Study of Ultra High Energy Cosmic Rays with the High Resolution Fly's Eye Prototype Detector

Chihwa Song

Submitted in Partial Fulfillment of the
Requirements for the Degree
of Doctor of Philosophy
in the Graduate School of Arts and Sciences

COLUMBIA UNIVERSITY

2001

ABSTRACT

Study of Ultra High Energy Cosmic Rays with
the High Resolution Fly's Eye Prototype Detector

Chihwa Song

The High Resolution Fly's Eye (HiRes) detector is an air fluorescent light detector for the study of ultra high energy ($> 10^{17}$ eV) cosmic rays. HiRes comprises two detectors operated in a stereo mode in the dry air of the desert near Dugway, Utah. Between 1993 and 1996 one site was operated as a prototype to study the flux and average mass composition of cosmic rays between 10^{17} and 10^{19} eV. In this thesis, I study the energy spectrum and the composition of cosmic rays in this energy region. For this analysis, detector properties like the aperture and the resolution are investigated with an extensive detector simulation. In addition, I study the question whether cosmic rays at the highest energies are gamma rays, as predicted by theories explaining cosmic rays as decay products of topological defects. Several methods are proposed to discriminate gamma showers from protons and heavier nuclei. An application on HiRes monocular data shows no significant result due to lack of statistics, but in the future, the full stereo HiRes detector will unambiguously discriminate between the particle types.

Contents

List of Tables

List of Figures

Acknowledgments

I would like to thank my advisor Stefan Westerhoff for helping me complete my doctoral degree and for his patient assistance.

My work could not have been carried out without efforts of all HiRes-MIA collaborators. I would like to express my appreciation to my collaborators at the University of Utah. I thank them for their full support while staying in Utah. I thank Zhen Cao, Bruce Knapp, John N. Matthews and Pierre Sokolsky for their guidance. I appreciate the help from Tareq Abu-Zayyad and Xingzhi Zhang. Their independent efforts enabled me to use the HiRes-I monocular data. I am indebted to Bruce Dawson for his valuable advice and help.

I also want to express special thanks to Dieter Heck, Johannes Knapp and Sciutto Sergio for their valuable help with the air shower simulation codes CORSIKA and AIRES. I want to acknowledge support from the Center for High Performance Computing, Utah.

Finally, I thank my wife for her invaluable support.

Introduction

In our universe, there are numerous mysterious and unusual phenomena. Among these, some astrophysical objects act as accelerators that boost particles to energies much higher than those generated by man-made accelerators. These high energy particles have been indirectly observed on earth. That is, instead of the primary particles, secondary particles of the air shower cascade induced by the primary in the earth's atmosphere have been detected. These secondary particles subsequently ionize air molecules. It was Hess who discovered in 1912 that the ionizing radiation came from outer space by measuring the ionization of the atmosphere at increasing altitudes. Since then, this ionizing radiation has been referred to as cosmic rays, but the sources of cosmic rays have not been identified yet, in spite of numerous attempts.

Observed energies of cosmic rays reach up to about 10^{20} eV. Such high energy cosmic rays are called ultra high energy cosmic rays, although there is no explicit definition of ultra high energy. For the purposes of this thesis, I will define ultra high energy as energies greater than 10^{17} eV. Such high energy cosmic rays are thought to be accelerated by astrophysical objects such as supernova remnants, active galactic nuclei and hot spots of radio galaxies. However, all of these hypotheses have some problems, mainly insufficient acceleration and significant energy losses by accelerated particles within the acceleration region. As a consequence, the theoretical models usually employ extreme values in parameters to explain the extension of the spectrum beyond 10^{20} eV.

There is another approach to explain ultra high energy cosmic rays. In so-called 'top-down' models, particles are created by the decay of supermassive meta-stable X

particles rather than accelerated from low energies. The X particles can be produced by radiation, interaction or collapse of topological defects in the very early universe. Possible topological defects are ordinary cosmic strings, superconducting strings, annihilation of magnetic monopole-antimonopole pairs and cosmic necklaces. In any case, chemical composition and incoming direction provide important clues to the origin of cosmic rays.

The cosmic ray flux observed on earth is predicted to be cut off at about 3×10^{19} eV due to photo-pion production. This was recognized by Greisen a few years after the cosmic microwave background radiation was discovered by Penzias and Wilson in 1965. The source of protons whose energies is greater than 3×10^{19} eV is limited to within 50 Mpc of earth. This end of the energy spectrum is known as the Greisen-Zatsepin-Kuzmin (GZK) cut-off. By now, several experiments have reported events above 10^{20} eV, but no significant evidence to align arrival directions with nearby astronomical objects has been found so far, although this cut-off provides a strong constraint in the search for possible sources.

At energies above 10^{16} eV, it is no longer possible to detect the primary cosmic ray particles directly. The arrival direction, mass and energy of primary particles have to be deduced from the air showers induced in the earth's atmosphere when the particles interact with air molecules. Ground array detectors like AGASA [1], Haverah Park [2] and Yakutsk [3] consist of a large number of particle detectors such as scintillators, muon counters and water Cherenkov tanks that measure the particles of the air shower that reach ground level, typically over a large area with a sampling ratio of a few percent.

Unlike the ground array detectors, the Fly's Eye and its successor, High Resolution Fly's Eye (HiRes), collect fluorescent light from exited nitrogen molecules caused by shower particles. The atmosphere acts like a rather complex calorimeter. Because the fluorescent light is emitted isotropically, the longitudinal shower development can be measured at a distance. To extract meaningful information from observables and to infer physical principles, we need to understand air showers and our detector correctly.

For this reason, reliable air shower simulations and simulation of the detector itself have to be carried out.

In this thesis, the characteristics of air showers are studied using the air shower simulation codes CORSIKA (COsmic Ray SImulations for KASCADE) and AIRES (AIR shower Extended Simulations). Energy determination of cosmic rays in atmospheric fluorescent light detection techniques is investigated with the aid of the air shower simulation CORSIKA. We also study the longitudinal development of air showers, and propose a Gaussian function in shower age to use for fitting the data. In addition, the longitudinal shower profile is parameterized as a function of energy for proton and iron primaries. This parameterization is employed in the detector simulation and enables us to simulate the detector response to realistic air showers without time-consuming full air shower simulations.

Based on these studies with the detector simulation, events of good quality are selected and reconstructed. Using HiRes prototype data, we study the chemical composition and flux of cosmic rays at energies between 10^{17} and 10^{19} eV. From direct measurements of cosmic rays with balloon- and satellite-borne instruments at low energies, we know that the composition of the cosmic ray flux changes from proton-dominated to iron-dominated between 10^{13} and 10^{15} eV, and it is believed to originate from supernova remnants in our galaxy. At higher energies, we have to deduce the composition indirectly from the observation of the air showers, and the conclusions depend on the hadronic interaction model, causing large uncertainties. Composition studies are, however, important as they provide clues to the origin of cosmic rays. If the composition becomes lighter as indicated in the composition study by the Fly's Eye, the cosmic rays are probably extragalactic.

At the highest energies, the source of cosmic rays is not known. But the break at 3×10^{18} eV of cosmic ray flux, which is referred to as the 'ankle', may be interpreted as the emergence of a new source of cosmic rays. It is generally believed that cosmic rays above the ankle are of extragalactic origin. Some top-down scenarios predict a flux of gamma rays and neutrinos, which also solves the propagation problem - at

these energies charged particles cannot travel over a long distance due to the significant energy loss via photo-pion production with microwave background radiation. Thus, a method to identify gamma rays above the ankle is proposed, based on the simulation study using the fact that such high energy gamma rays can interact with the earth's magnetic field and consequently produce secondary particles at the top of the atmosphere instead of the primary gamma rays. This effect causes air showers to have their shower maximum at higher elevations depending on the strength of the magnetic field, and this can be observed by the HiRes detector. For this study, HiRes-I monocular data is used because the HiRes prototype data does not cover these high energies. One of the advantages of this method is that it does not require good resolution of energy and arrival direction. The composition above the ankle may indeed help to discriminate between top-down and conventional scenarios.

Chapter 1

COSMIC RAYS

Cosmic rays are not really rays. In fact, they are energetic particles, primarily protons and alpha particles. The source of cosmic rays is not certain even though there are possible sources such as the sun, supernovae, radio galaxies, neutron stars and gamma ray bursts. The total energy density of cosmic rays is about 1 eV/cm^3. The most energetic particle detected so far had an energy of about 3×10^{20} eV (50 J), which equals the kinetic energy of the fastest baseball pitch. Cosmic rays are not only interesting, they are a natural source of high energy particles, and many particles have been found in cosmic rays before they were produced in the laboratory.

1.1 Discovery of Elementary Particles

Electrons and protons were discovered in laboratories, but several more elementary particles were discovered in cosmic ray observatories before they could be produced in accelerators. Cosmic ray physics has thus made a fundamental contribution to high energy particle physics.

The first particle to be discovered in cosmic rays was the positron, which was observed in a cloud chamber by Millikan and Anderson in 1930 [4]. This discovery was confirmed by Blackett and Occhialini in 1933. By 1936, Anderson and Neddermeyer discovered particles with a mass intermediate between those of the electron and

the proton, which were called 'mesotrons' [5]. In fact, these are muons, which were originally thought to be the pions predicted by Yukawa to explain the nature of the nuclear force. In 1947, Rochester and Butler reported the discovery of two cases of particle tracks in the form of 'V's with no incoming particles [6]. This class of particles were known as 'strange' particles. Both neutral and charged strange particles were discovered and they are now referred to as charged and neutral kaons (K^+, K^-, K^0). Meanwhile, another powerful tool, nuclear emulsions, had been developed by Cecil Powell. The photographic emulsions showed clearly the production of charged pions (π^+, π^-). In bubble chambers, the Ξ^- particle was discovered by Armenteros et al. in 1952 [7] and the Σ particle was discovered by Bonetti et al. in 1953 [8].

Since the first accelerator, the voltage multiplier, was invented in 1929, accelerator technology has developed continuously. In the 1950s, accelerated particles reached the point where their energies were comparable to those available in cosmic rays. For example, in 1953 the Cosmotron at Brookhaven National Laboratory could boost proton energies to 3 GeV. After about 1953, the future of high energy physics lay in the accelerator laboratory rather than in the cosmic ray observatory. The interest in cosmic ray physics shifted to the questions of the origin, propagation and chemical composition of cosmic ray particles [9].

1.2 History of Cosmic Ray Physics

A charged electroscope is discharged by ionized air molecules caused by natural radioactive material but it keeps discharging even without the source. The source of natural radiation forming ions in the atmosphere was examined by Wilson [10]. However, it remained unsolved in spite of his various attempts. In 1912, this problem was solved through a series of balloon flights by Hess and later Kolhörster [11, 12]. They found that the ionization of the atmosphere increased with altitudes and the radiation at 9 km was about 10 times more intense than at sea level. The measurement is in contrast to what is expected for radiation from the earth, which means

that the source of the ionizing radiation was extraterrestrial. Later, the radiation was named 'cosmic rays' by Millikan. At that time, cosmic rays were thought to be hard gamma rays which could be more penetrating than alpha and beta particles. Later they turned out to be primarily charged particles.

In 1929, the Geiger-Müller counter enabled individual cosmic rays to be detected. It was soon discovered that the earth's magnetic field strongly influences low energy cosmic rays. Because of the deflection of charged particles in the magnetic field, an east-west anisotropy was discovered. The Geiger-Müller detector also enabled Pierre Auger in 1938 to discover extensive air showers, which are cascades of subatomic particles initiated by primary cosmic particles in the atmosphere. Auger gradually increased the separation between two detectors spaced horizontally and found that the detectors continued to register coincidences up to 300 meters. Based on his measurements, Auger concluded that he had observed showers with energies of 10^{15} eV [13]. In 1946, groups led by Rossi and Zatsepin started experiments on the structure of Auger showers. These were the first arrays of correlated detectors to detect air showers.

In 1963, John Linsley and his collaborators discovered the first cosmic ray with an energy of about 10^{20} eV in the Volcano Ranch array in New Mexico [14]. In 1991, the Fly's Eye experiment in Utah observed a cosmic ray event with an energy of 3.2 $\times$ 10^{20} eV [15]. A few years later, the AGASA Group in Japan [1] and the Yakutsk group in Russia [3] reported events with energies of 2.1 $\times$ 10^{20} eV and 1.1 $\times$ 10^{20} eV, respectively.

1.3 Characteristics of Cosmic Rays

1.3.1 Energy Spectrum

At energies less than a few tens of GeV, the energy spectrum changes with variations in solar activity. During sunspot maximum, the sun's magnetic field becomes stronger and shields the earth from cosmic rays. Consequently the energy spectrum of cosmic rays changes inversely with solar activity. The energy spectrum of cosmic rays spans a

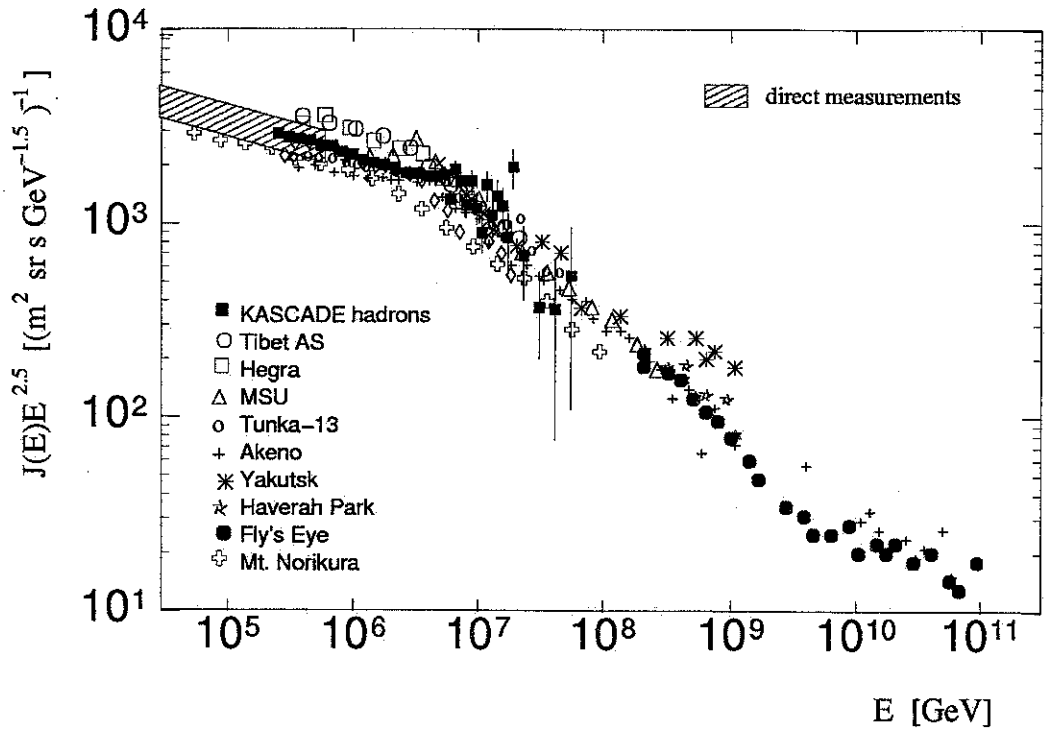

Figure 1.1: The energy spectrum of cosmic rays. The data around the 'knee' was taken from reference [16].

very wide range of energies and is well represented to first order by a power law ($E^{-\gamma}$) distribution at energies above the solar modulation region. The energy spectrum has been measured by a number of experiments, as shown in Figure 1.1. In this figure, the flux is multiplied by $E^{2.5}$ to enhance the structure. The breaks in the spectrum at $10^{15.5}$ and $10^{18.5}$ eV are referred to as the 'knee' and the 'ankle', respectively. The slopes (γ) of the energy spectrum below and above the knee are approximately 2.7 and 3.0.

One of the most striking features is the fact that the energy spectrum continues beyond 50 EeV. High energy protons at these energies interact with microwave background radiation via $p\gamma_{2.7K} \rightarrow p\pi^0$ or $p\gamma_{2.7K} \rightarrow n\pi^+$, an interaction that is expected to cause a cut-off in the cosmic ray energy spectrum. This is known as the Greisen-Zatsepin-Kuzmin (GZK) cut-off [17, 18]. It is also possible to lose energy via pair production ($p\gamma_{2.7K} \rightarrow pe^-e^+$). In fact, the cross section of pair production is

larger than that of photo-pion production. However, the energy loss due to the pair production is negligible since the mass of the electron is much smaller than the mass of the pion. The characteristic attenuation length is about 50 Mpc for a proton of energies of 10^{20} eV [19]. This limits the distance of possible astrophysical sources to around 50 Mpc. The active galaxy M87 in the Virgo cluster is a possible source for cosmic rays above 50 EeV, and it is 16 Mpc away from earth. At these energies, the deflection in extragalactic magnetic fields is small ($< 1°$), so these particles should point back to their sources. But no strong experimental evidence has yet been found although the current data sample suffers from small statistics.

1.3.2 Chemical Composition and Sources

The chemical composition of the cosmic rays provides important clues to their origin and to the processes of propagation from their sources to the earth. Moreover, the change in the composition and in the spectrum are correlated. Thus, we will discuss the composition at different energy regions.

Below the Knee ($E < 10^{10}$ eV)

Low energy cosmic rays consist mainly of protons and light nuclei. The data taken by satellite and balloon experiments shows that the chemical composition of the cosmic rays is similar to that of the solar system, as shown in Figure 1.2. However, when compared to the elements of the solar system, cosmic rays have higher levels of hydrogen and helium, and lower amounts of lithium, beryllium, boron and of several elements with atomic numbers between calcium and iron [20]. This can be explained by 'spallation' [21]. The particles produced in their sources interact with interstellar gases - mostly hydrogen and helium - and produce lighter nuclei. This relative abundance provides us with very important clues as to the nature of the propagation of cosmic rays in our galaxy.

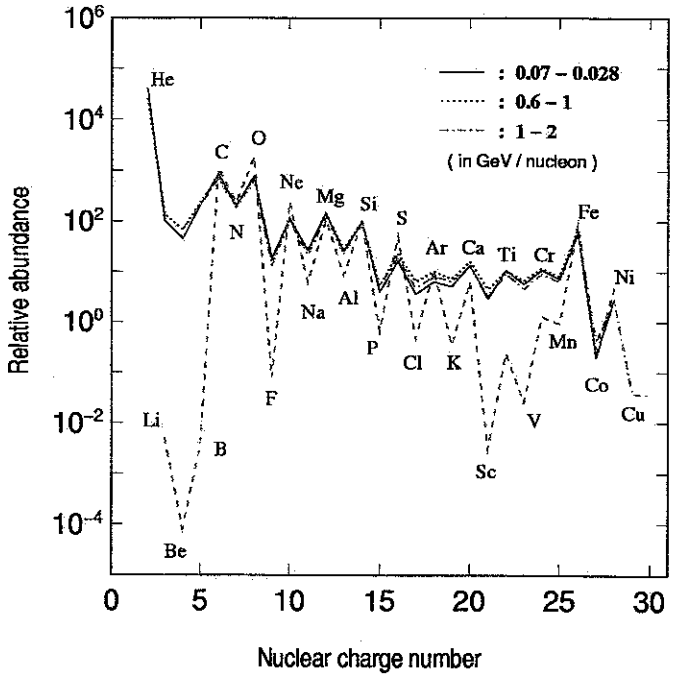

Figure 1.2: The relative abundance of element in the solar system (green dashed line) and in cosmic rays (all other lines) are compared in three different energy ranges. The data has been normalized to [Si]=100 [20].

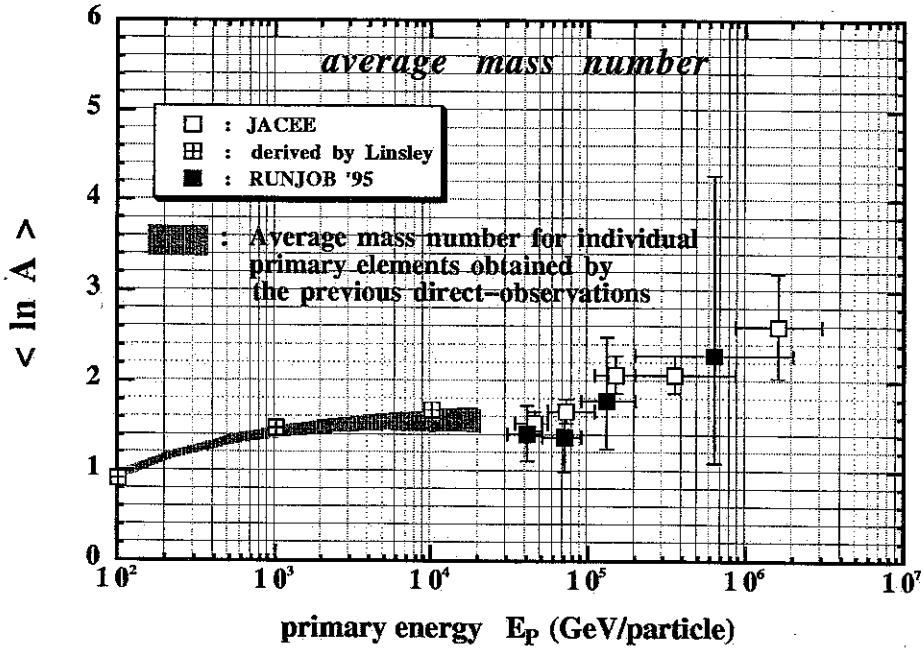

Figure 1.3: The average atomic number of cosmic rays [22].

Around the Knee ($10^{12} < E < 10^{16}$ eV)

The source of cosmic rays at these energies is believed to be supernova remnants which can easily account for the energy stored in galactic cosmic rays [23]. The maximum energy that can be reached by supernova remnants is about the particle's charge times 10^{14} eV. Measurements taken from high altitude balloons (JACEE [24], RUNJOB [25]) and satellites (PROTON [26], SOKOL [27]) show that as the cosmic ray energy increases, the composition of the cosmic rays is changed from proton-dominated to iron-dominated between 10^{13} and 10^{15} eV. Figure 1.3 shows the average atomic number of cosmic rays. This suggests that as the energy reaches the knee of the spectrum, heavy nuclei become the dominant component. This change in chemical composition is explained in the so-called 'Leaky Box' model. In this model, the particles are assumed to be reflected at the galactic boundaries, but there is some probability that particles will diffuse out. This probability increases with the energy of the particle, as the radius of a particle's orbit in a magnetic field, the so-called Larmor radius, is given by

$$R \propto \frac{E}{ZB} \tag{1.1}$$

where Z is the charge of cosmic ray particle, B is the galactic magnetic field and E is the total energy of the particle. As the Larmor radius also depends on the charge of the particle, light nuclei have larger probabilities to reach the edge of the galaxy. Consequently, the remaining flux becomes dominated by heavy nuclei.

There are alternative explanations for the origin of the knee. One model explains the steepening of the energy spectrum by assuming that the characteristics of high energy particle interaction change suddenly at the knee [28]. Alternatively, the break in the energy spectrum may result from the decreasing number of high energy particles beyond the knee due to the increasing energy loss [29] or to the breakdown of the acceleration mechanism [30]. Above the knee, cosmic rays could be produced by re-acceleration by interstellar turbulence [31] or by supernova explosions in denser media [32]. The origin of cosmic rays above the knee may be extragalactic [33], but

the resulting composition becomes lighter above the knee.

Around the Ankle ($E > 10^{17}$ eV)

In higher energy regions from 10^{17} to $10^{18.5}$ eV, the Fly's Eye and MIA-HiRes data show that the composition becomes proton-dominated, based on the average maximum depth of the shower [15, 34]. In contrast to the results from the Fly's Eye, based on muon content of an air shower on the ground level, the AGASA group concluded that the composition does not change [35]. In fact, the interpretation of primary composition strongly depends on the hadronic interaction model. The discrepancy of the results between Fly's Eye and AGASA was explained by the fact that the two groups used quite different hadronic models [36]. The composition change from heavy to light nuclei may be attributed to a change of sources.

The composition above the ankle is not known. But light nuclei may be dominant based on the composition study of the MIA-HiRes, and the ankle of the cosmic ray spectrum may be interpreted as the change of the composition. At energies above 10^{19} eV, the arrival directions of cosmic rays roughly point to their sources as shown in Figure 1.4. However, there is no significant evidence that cosmic ray arrival direction clusters along the galactic plane. Thus, the sources of cosmic rays above the ankle are probably extragalactic. However, the arrival direction of the highest energy cosmic ray detected by the Fly's Eye was found to be off by 88° from the direction of the closest active galaxy, M87. The difficulties to explain the production of high energy cosmic rays from known astrophysical objects have stimulated physicists to invent new types of model. We will describe these new models as well as the conventional ones in the next section.

1.4 Origin of Ultra High Energy Cosmic Rays

There are two types of models which explain the sources of Ultra High Energy Cosmic Rays (UHECRs). 'Top-down' models postulate the production of the high energy particles via exotic processes, whereas 'bottom-up' postulate the acceleration of charged

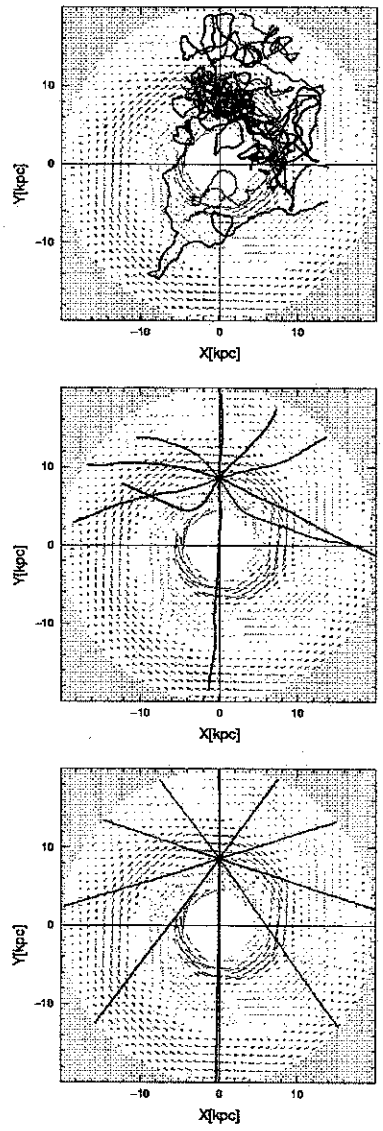

Figure 1.4: The path of antiprotons in our galaxy at energies of 10^{18}, 10^{19} and 10^{20} eV from top. The origin of the coordinate systems located at the center of the galaxy and the earth is located on the Y axis. The particles which originate from earth, move freely at higher energy [37]. The galactic magnetic field is about 3 μG and is parallel to the local spiral arms with large fluctuations.

particles in known astrophysical sources. However, if the UHECRs are gamma rays or neutrinos, they can travel over longer distances. In Chapter 7, we will discuss the possibility that the UHECRs are gamma rays and propose how to distinguish such high energy gamma rays from hadronic showers.

1.4.1 Bottom-Up Models (Astrophysical Sources)

UHECRs can be accelerated in or around astrophysical objects. There are two different acceleration mechanisms. First, particles can obtain high energies by diffusive, stochastic acceleration, which is also known as Fermi acceleration [38, 39, 40]. This occurs in all systems where shock waves are present, such as supernova remnants, hot spots of radio galaxies and colliding galaxies [41, 42]. Particles are accelerated by repeated encounters with moving magnetized plasmas. This type of mechanism naturally provides a power-law energy spectrum of cosmic rays. Secondly, in the 'one-shot' model, particles can be accelerated by very strong electric fields generated by rotating compact objects such as highly magnetized neutron stars and the accretion disks of black holes. However, the power-law spectrum can not be explained naturally by means of this model [43].

The origin of cosmic rays has long been believed to be supernovae which accelerate particles in expanding Supernova Remnants (SNRs) [44]. However, this has not yet been confirmed. Lepton acceleration by SNRs is implied by X-ray observations of SN 1006 [45], IC 443 [46] and Cas [47], but there is no evidence for accelerated hadrons from these sources [48]. Furthermore, it is difficult to explain the origin of cosmic rays above the knee with the SNR hypothesis. There is no strong correlation between the arrival directions of UHECRs and SNRs.

The most likely sources of UHECRs are the nearby strong radio galaxies which have Active Galactic Nuclei (AGN) and extended jets [49, 50]. At the ends of the extended jets, the so-called 'hot spots'[1], the relativistic shock wave is believed to be able to accelerate particles up to 10^{20} eV energies. However, this strongly depends

[1]Radio galaxies with and without hot spots are called Fanaroff-Riley Class I and II galaxies, respectively.

on the spot's local magnetic field, which is very uncertain. Moreover, the powerful radio galaxies are at large distances from our galaxy.

Material accreted by a black hole within an AGN will probably be magnetized. The magnetic flux will be frozen into the accreting material and so the field close to the horizon can become quite large [51]. Cosmic ray particles could be accelerated by the effective electromotive force generated by rotation of the externally supplied magnetic field lines threading the horizon.

In principle, AGNs can accelerate particles to a few tens of EeV [33, 52]. However, the particles lose their energy in the acceleration region due to curvature radiation and photo-pion production on intense radiation fields. In addition, there are energy losses due to synchrotron radiation and inverse Compton scattering. Eventually, the maximal energy becomes about 10^{16} eV, which is well below the initial energy [53]. To avoid this problem, the acceleration site should be outside the active center. Thus, this limitation has led to the proposal that the quasar remnants in nearby inactive galaxies are the sources of UHECRs [54]. The number of supermassive black holes associated with dead (no jet) quasars are sufficient to explain the observed UHECR flux.

Newly formed, rapidly rotating neutron stars such as the Crab and Vela pulsars may accelerate particles to high energies [55, 56, 57]. However, the ambient magnetic and radiation fields cause significant energy loss as in the AGN case. Recently discovered 'magnetars' - neutron stars with a very strong magnetic field (10^{15} G) - can accelerate particles to energies 2 to 3 orders of magnitude larger than ordinary pulsars.

Gamma Ray Bursts may be the source of the UHECRs [58, 59, 60, 61]. GRBs, like UHECRs, have unknown origins and are isotropically distributed in space. However, the flux of UHECRs associated with nearby GRB would be too small to fit the UHECR observations, and the distribution of UHECR arrival directions and times would not support their common origins [62].

All of these models have some problems, mainly insufficient acceleration and sig-

nificant energy loss by accelerated particles within the acceleration region via synchrotron radiation and inverse Compton scattering. These models usually employ extreme values in parameters to explain the extension of the spectrum beyond 10^{20} eV.

1.4.2 Top-Down Models (Exotic Sources)

There is another approach to explain the UHECRs, the so-called 'top-down' models. In these models, the UHECRs are created by the decay of unstable or metastable superheavy elementary 'X' particles rather than accelerated from lower energies. The decay mechanism of the X particles into quarks and leptons depends on their origin and nature, and the spectra of the particles resulting from the decay are determined by quantum chromodynamics. Hadronization of quarks generates mainly pions and a small fraction of neutrons and protons.

The X particles may be produced through two different mechanisms. First, they can be produced by radiation, interaction or collapse of topological defects in the very early universe. The possible sources of UHECRs are ordinary cosmic strings [63, 64, 65], superconducting strings [66, 67], annihilation of magnetic monopole-antimonopole pairs (monopolonia) [68, 69], cosmic necklaces [70] and possible direct emission of X particles from cosmic strings [71, 72]. Secondly, long-lived superheavy relic particles can be produced from a primordial quantum field after the inflationary stage of the universe [73, 74]. Their mass should be larger than 10^{12} GeV and their lifetime should be larger than or comparable to the age of the universe so they can decay in the present era. The relic particles can exist with sufficient abundance so as to act as cold dark matter particles. The relic particles are expected to be clustered in our galactic halo and can produce UHECRs which experience no cutoff. In addition, a slight anisotropy is predicted due to the asymmetric position of the sun in the galaxy [75, 76], and recent studies show that the present data is consistent with the anisotropy expected in the model of X particles in the halo [77, 78]. Whereas top-down models have no problem explaining the high energies of cosmic rays, the exotic sources may be insufficient to

explain the flux of cosmic rays [53, 65].

Chapter 2

EXTENSIVE AIR SHOWERS

As mentioned in the previous chapter, the flux of cosmic rays above 10^{15} eV is low, and detectors with large apertures are therefore crucial. Consequently, the detectors have to be earth-based, and we observe the extensive air showers caused by the primary cosmic ray particles instead of the primary particles themselves. The earth's atmosphere acts as a complicated calorimeter, and a detailed knowledge of the physics of air shower development is crucial. In this chapter, we review the particle interactions in the air showers and how the air showers develop longitudinally and laterally. In addition, we will describe how to determine the primary energy from observables depending on the detection technique. To demonstrate relevant physical phenomena, the air shower simulation code CORSIKA [79] is used. At the end of this chapter, we describe the various experimental techniques for air shower detection and their advantages and shortcomings.

2.1 Cascade Physics

Cosmic ray particles make inelastic collisions with nuclei in the atmosphere and produce nucleons, mesons and other particles. Most of the mesons produced in this collision are pions. Neutral pions decay into photons which initiate an electromagnetic cascade. Electromagnetic interactions are governed by the laws of quantum electrodynamics and can be described with a high degree of accuracy. However, hadronic interactions are much more complicated than electromagnetic ones. Various

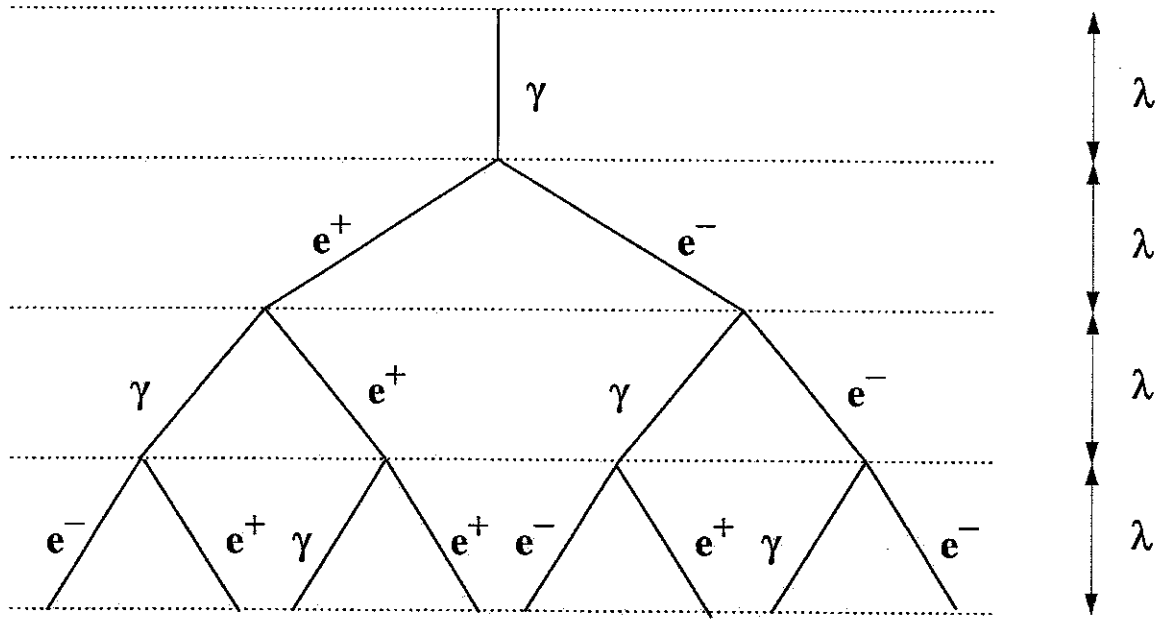

Figure 2.1: The simple electromagnetic cascade.

processes in hadronic interactions may occur.

2.1.1 Electromagnetic Cascades

Let us consider a simple electromagnetic cascade as shown in Figure 2.1. The mean free path λ of the photon is about the same as the radiation length of electrons in the ultra-relativistic limit. The number of particles at depth X after $n = X/\lambda$ interactions is

$$N(X) = 2^{X/\lambda}, \tag{2.1}$$

where X and λ are in g/cm^2. Thus, the average energy of the particles is

$$E(X) = \frac{E_0}{N(X)}, \tag{2.2}$$

where E_0 is the energy of the primary particle. The maximum number of particles is given by

$$N_{max} = N(X_{max}) = \frac{E_0}{E_c}, \tag{2.3}$$

where E_c is the critical energy and X_{max} is the depth at which the shower reaches maximum size. After this, the number of particles falls off because ionization dominates the energy loss. Combining Eq. (2.1) and Eq. (2.3) gives the depth of shower maximum:

$$X_{max} = \lambda \frac{\ln(E_0/E_c)}{\ln 2}. \tag{2.4}$$

By using the definition of the radiation length, combining Eq. (2.2) at a radiation length(X_r)

$$N(X_r) = \frac{E_0}{E(X_r)} \equiv e, \tag{2.5}$$

and Eq. (2.1) gives us

$$X_r = \frac{\lambda}{\ln 2}. \tag{2.6}$$

Eq. (2.4) can be expressed in terms of the radiation length:

$$X_{max} = X_r \cdot \ln(E_0/E_c). \tag{2.7}$$

This simple model works well over a wide energy range. However, even though the cross-sections for $\mu^+\mu^-$ pair production and photo-nuclear reaction are small, they should be considered in order to account for the muon component in high energy gamma induced showers. In the high energy limit, the cross-section for the $\mu^+\mu^-$ pair production approaches

$$\frac{\sigma_{\mu^+\mu^-}}{\sigma_{e^+e^-}} = \frac{m_e^2}{m_\mu^2} \cong 2.3 \times 10^{-5}, \tag{2.8}$$

and reaches 11.4 μb above $E_\gamma = 1$ TeV. The photo-nuclear cross-section of the proton is compared with other cross sections in Figure 2.2. According to this figure, one out of about 300 gamma induced showers behaves like a hadronic shower.

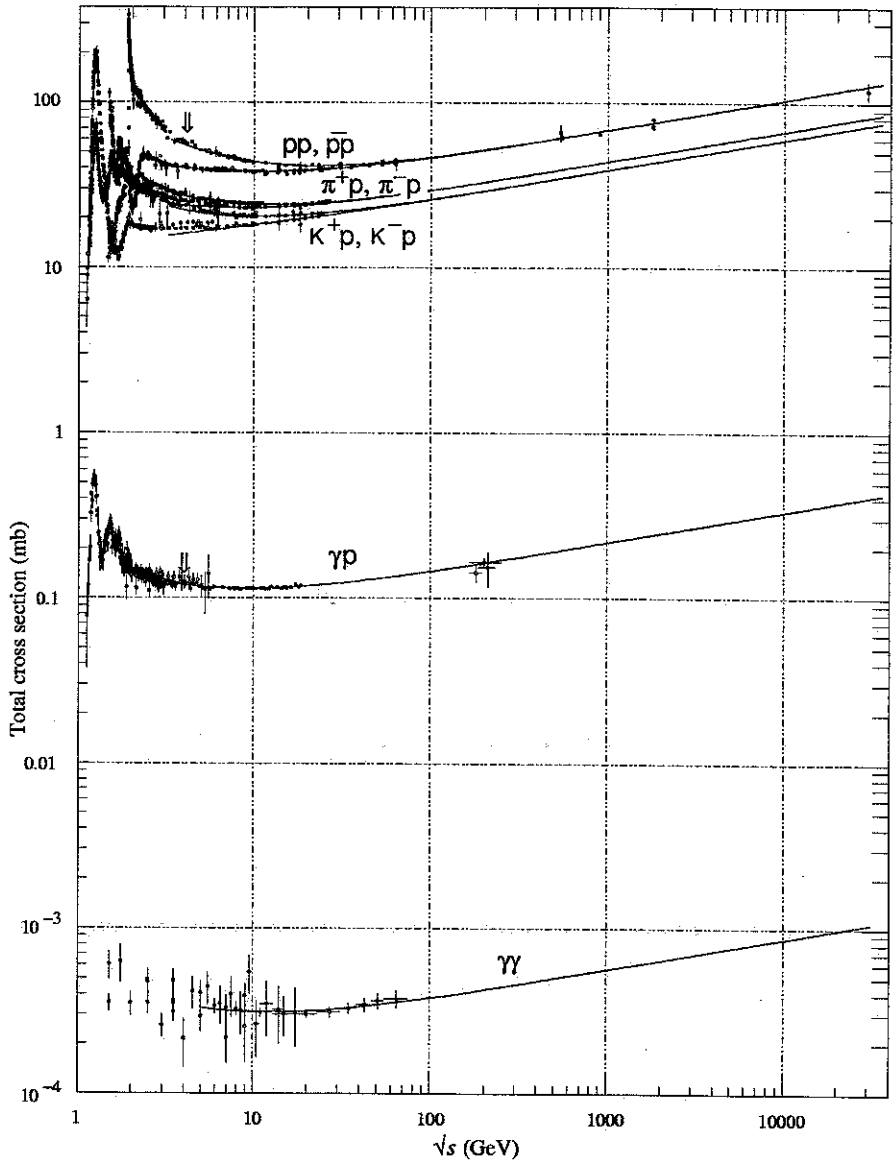

Figure 2.2: The hadronic, pγ and $\gamma\gamma$ cross sections [80].

other atomic nuclei can disturb the electron while it travels in the formation zone. The multiple scattering of the electron during this interaction can cause suppression of bremsstrahlung. A similar effect occurs in pair production at higher energies, because the LPM effect depends only on the electron's energy.

The dielectric suppression for the soft photon emission is called Ter-Mikaelian effect [84]. Radiated photons can interact with the electrons in the medium by forward Compton scattering. This interaction can be coherent, causing a phase shift over the formation zone. If the phase shift is large enough, it can lose coherence, and consequently the photon emission is suppressed. As the photon energy approaches zero, bremsstrahlung is completely suppressed, causing a cut-off at low energies in the energy spectrum of radiated photons. There is no infrared divergence of the emitted photon energy spectrum in this case. A detailed theoretical description and experimental results on the dielectric suppression from E-146 at SLAC can be found in [83, 85].

In bremsstrahlung, an electron of energy E emits a photon of energy k near a nucleus of charge Z. The cross section for this process is given by Migdal, taking into account the LPM effect [82]:

$$\frac{\mathrm{d}\sigma_{brem}}{\mathrm{d}k} = \frac{4\alpha r_e^2 \xi(s)}{3k}\Big\{y^2 G(s) + 2[1+(1-y)^2\phi(s)]\Big\}Z^2 \ln\left(\frac{184}{Z_{1/3}}\right), \qquad (2.9)$$

where $y = k/E$ and $s = (E_{LPM}k/4E(E-k)\xi(s))^{1/2}$. $G(s)$, $\phi(s)$ and $\xi(s)$ are described in detail in Appendix A. E_{LPM} is the characteristic energy in TeV of the LPM effect and is given by

$$E_{LPM} = \frac{m^2c^4 X_r \alpha}{8\pi\hbar c} \cong 3.84 \times X_r, \qquad (2.10)$$

where $m \cong 0.511$ MeV/c^2, X_r is the radiation length in cm and α is the fine structure constant. For example, E_{LPM} is 2.2 TeV for lead, 139 TeV for water and 116 PeV for air at STP. The suppression factor due to the LPM effect can be defined as

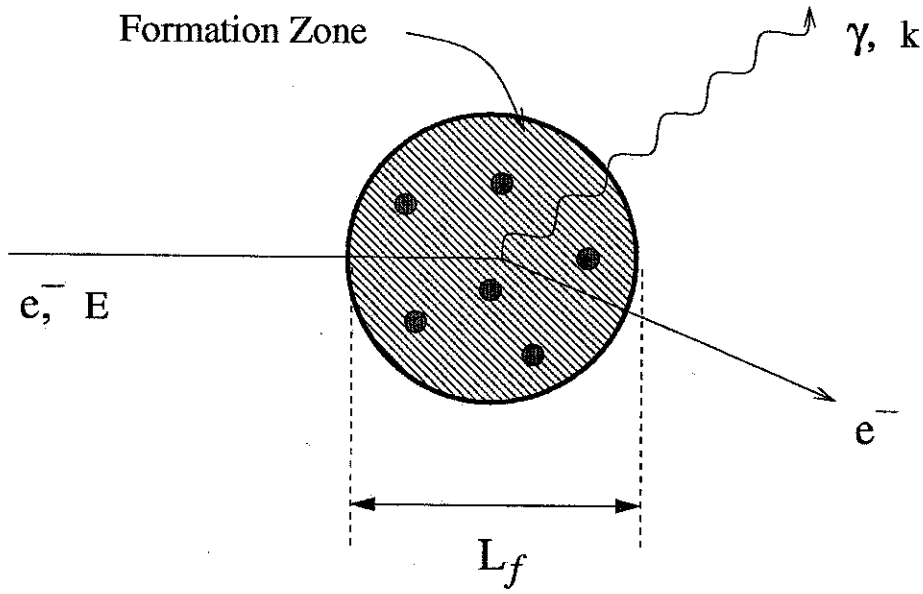

Figure 2.3: An electron of energy E emits a soft photon of energy k near a nucleus of charge Z via bremsstrahlung. If the formation length (L_f) becomes comparable to the distance over which multiple scattering becomes important, bremsstrahlung is suppressed.

At high energies ($> 10^{19}$ eV), however, another process becomes important. Due to multiple scattering and dielectric suppression, the cross sections of electron bremsstrahlung and pair production are drastically reduced. The suppression mechanism due to multiple scattering is called the Landau-Pomeranchuk-Migdal (LPM) effect. The LPM effect was first predicted by Landau and Pomeranchuk in 1953 [81] and Migdal provided the corresponding quantum mechanical theory in 1956 [82]. This suppression was observed and investigated recently at the Stanford Linear Accelerator Center (SLAC) [83]. Figure 2.3 illustrates the LPM effect. An electron of energy E emits a soft photon of energy k near a nucleus of charge Z via bremsstrahlung. In the ultra-relativistic limit, the electron transfers a small amount of the longitudinal momentum to the nucleus involved in the bremsstrahlung process. According to the Heisenberg uncertainty principle, the uncertainty about where the momentum transfer occurs is very large - larger than the atomic scale. The distance interval in which the interaction must take place is called the formation length (L_f). In dense materials,

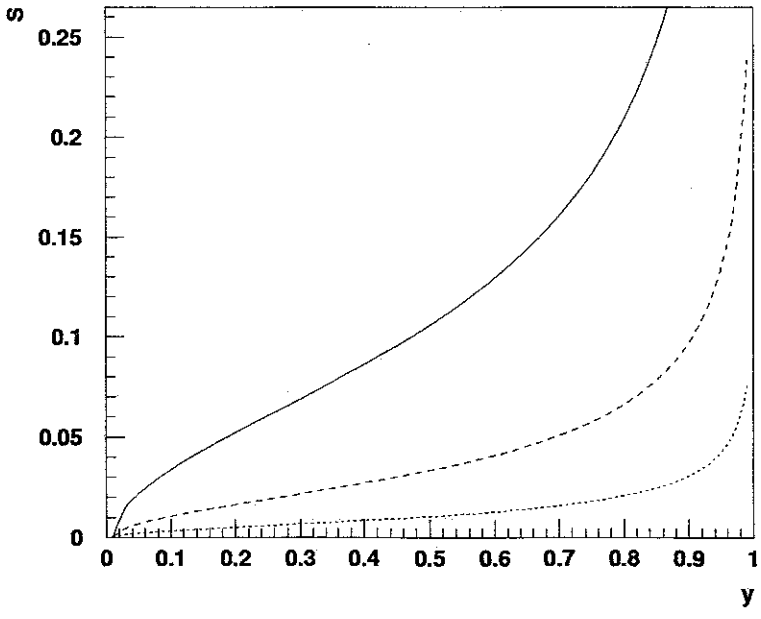

Figure 2.4: The suppression due to LPM effect is calculated in air ($E_{LPM} = 116$ PeV). The suppression factor is shown as a function of y for energies $E = 10^{19}$ eV (solid line), 10^{20} eV (dashed line) and 10^{21} eV (dotted line).

$$S = \frac{\mathrm{d}\sigma_{brem}/\mathrm{d}k}{\mathrm{d}\sigma_{BH}/\mathrm{d}k}, \tag{2.11}$$

where σ_{BH} is the cross section given by Bethe and Heitler [86]:

$$\frac{\mathrm{d}\sigma_{BH}}{\mathrm{d}k} = \frac{4\alpha r_e^2}{3k}\Big\{y^2 + 2[1 + (1-y)^2]\Big\}Z^2 \ln\left(\frac{184}{Z_{1/3}}\right). \tag{2.12}$$

Figure 2.4 shows S as a function of y for different values of the electron energy in air. The bremsstrahlung cross section becomes smaller as the energy increases. Consequently, this effect causes an electromagnetic shower to develop slowly.

For pair production, we have

$$\frac{\mathrm{d}\sigma_{pair}}{\mathrm{d}E} = \frac{4\alpha r_e^2 \xi(\tilde{s})}{3k}\Big\{G(\tilde{s}) + 2[u + (1-u)^2]\phi(\tilde{s})\Big\}Z^2 \ln\left(\frac{184}{Z^{1/3}}\right), \tag{2.13}$$

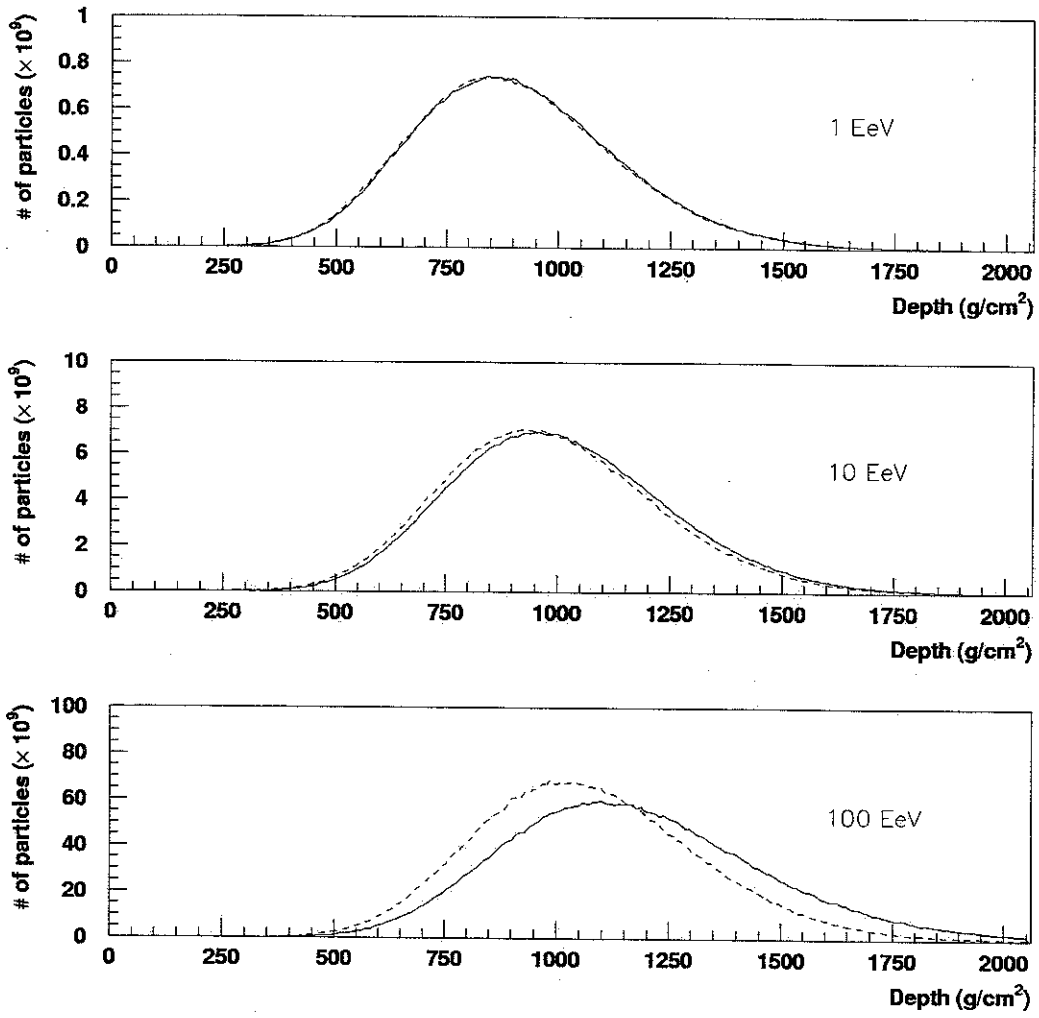

Figure 2.5: The average profiles of gamma induced showers generated by CORSIKA are shown at three different energies with (solid line) and without (dashed line) LPM effect. 400 events were generated at each energy.

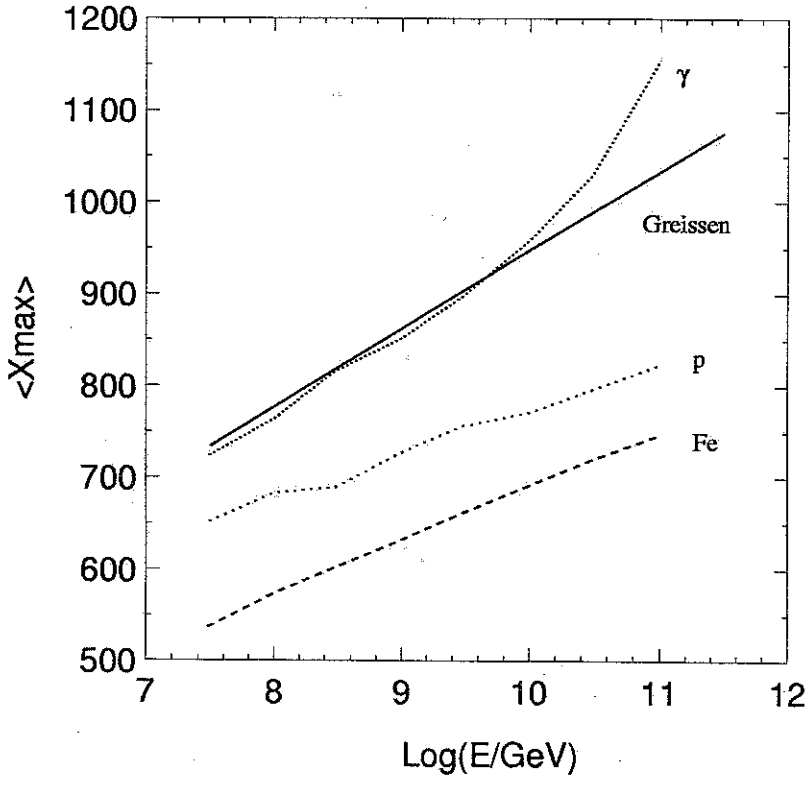

Figure 2.6: The average X_{max} for air showers induced by gamma, proton and iron at fixed energies as determined by CORSIKA simulations. The average X_{max} of the gamma induced showers is compared with Eq. (2.7) for pure electromagnetic showers. The LPM effect makes gamma induced air showers develop slowly.

where $u = E/k$ and $\tilde{s} = (E_{LPM}k/4E(k-E)\xi(\tilde{s}))^{1/2}$.

One of the electrons produced in pair production carries most of the initial photon's energy. Thus, the average energy of electromagnetic shower particles will decrease only slowly. Therefore, the LPM effect is important at the developing stage as well as at the beginning stage of the shower. The average shower developments with and without LPM effect are shown in Figure 2.5. Although most particles in hadronic showers are electromagnetic, the LPM effect does not influence the shower development because the average energies of shower particles decrease very quickly. Figure 2.6 shows the influence of the LPM effect on the electromagnetic cascades. The LPM effect becomes important and is crucial to the study of cosmic ray composition at high energies (> about 10^{19} eV).

2.1.2 Hadronic Cascades

After the initial nucleon-nucleus collision, secondary nucleons and charged pions continue to interact with nuclei in the atmosphere until the energies drop below 1 GeV, which is required for multiple pion production. Protons lose energy by ionization and charged pion decay via:

$$\pi^+ \rightarrow \mu^+ + \nu_\mu, \tag{2.14}$$

$$\pi^- \rightarrow \mu^- + \bar{\nu_\mu}, \tag{2.15}$$

where the mean lifetime of the charged pion is 2.551×10^{-8} s.

The muons slow down by ionization and the energy loss is small. The low energy muons decay via:

$$\mu^+ \rightarrow e^+ + \nu_e + \bar{\nu_\mu}, \tag{2.16}$$

$$\mu^- \rightarrow e^- + \bar{\nu_e} + \nu_\mu, \tag{2.17}$$

where the mean lifetime of the muon is 2.2001×10^{-6} s.

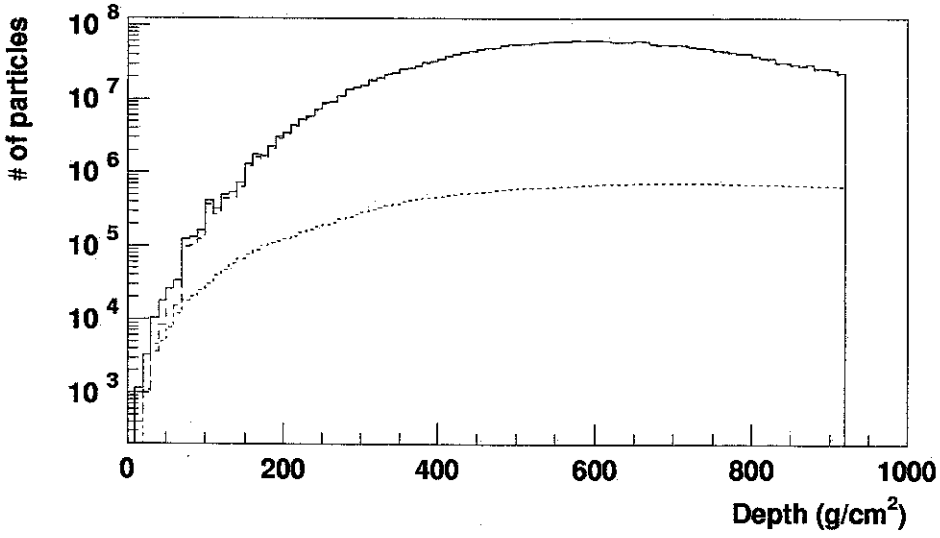

Figure 2.7: The shower profiles of charged particles (solid line), electrons (dashed line) and muons (dotted line) for a proton induced shower at 10^{17} eV generated by CORSIKA.

decay mode	branching ratio	decay mode	branching ratio
$K^{\pm} \longrightarrow \mu^{\pm} + \nu_{\mu}$	63.51 %	$K_S^0 \longrightarrow \pi^+ + \pi^-$	68.61 %
$K^{\pm} \longrightarrow \pi^{\pm} + \pi^0$	21.16 %	$K_S^0 \longrightarrow \pi^0 + \pi^0$	31.39 %
$K^{\pm} \longrightarrow \pi^{\pm} + \pi^{\pm} + \pi^{\mp}$	5.59 %	$K_L^0 \longrightarrow \pi^{\pm} + e^{\mp} + \nu_e$	38.78 %
$K^{\pm} \longrightarrow \pi^0 + e^{\pm} + \nu_e$	4.82 %	$K_L^0 \longrightarrow \pi^{\pm} + \mu^{\mp} + \nu_{\mu}$	27.17 %
$K^{\pm} \longrightarrow \pi^0 + \mu^{\pm} + \nu_{\mu}$	3.18 %	$K_L^0 \longrightarrow \pi^0 + \pi^0 + \pi^0$	21.12 %
$K^{\pm} \longrightarrow \pi^0 + \pi^0 + \pi^{\pm}$	1.73 %	$K_L^0 \longrightarrow \pi^+ + \pi^- + \pi^0$	12.56 %

Table 2.1: The major decay modes of kaons and their branching ratios [80].

Meanwhile, the neutral pions decay into two photons immediately after the first interaction since their lifetimes are very short (1.78×10^{-16} s):

$$\pi^0 \rightarrow \gamma + \gamma.$$

These photons initiate electromagnetic cascades. Figure 2.7 shows the number of particles as a function of depth. Most charged particles are electrons and only about 1 % of the charged particles are muons. Kaon decay also initiates electromagnetic cascades or produces muons. Table 2.1 shows the major decay modes and branching ratios for kaons.

2.1.3 Nuclear Interactions

When a primary particle interacts with an atmospheric molecule, not all nucleons of a projectile nucleus participate in the interaction. The non-interacting nucleons are called 'spectators'. In the simulation, the spectators can be treated in two ways [79]. First, they can be regarded as free nucleons with their initial velocities. This assumes the 'total fragmentation' of the projectile nucleus in the first interaction. Secondly, 'no fragmentation' keeps all spectators together as one nucleus. For more realistic treatment, the excitation energy of this remaining nucleus can be calculated from the number of wounded nucleons in a way described by Gaimard [87]. Each wounded nucleon is assumed to be removed out of the Woods-Saxon potential of the original projectile nucleus, which leads to a hole state in the nucleonic energy level system. From the total excitation energy, the number of evaporating nucleons or α particles is calculated assuming a mean energy loss per evaporated nucleon of 20 MeV [88]. The emitted nucleons carry transverse momenta determined by experiments [89] or by Goldhaber's theory [90] using 0.090GeV/nucleon as the average transverse momentum.

2.2 Shower Development

The main goal of cosmic ray experiments is to measure the primary energy, the arrival direction and the type of the primary particle. However, only the arrival direction can be measured directly. The energy and composition have to be deduced from the air shower development by using Monte Carlo simulation. Based on the average behavior of shower maximum depth or muon content in an air shower on the ground level, the mass of the primary particle can be inferred. The primary energy can be obtained from the longitudinal shower profile and the total number or density of shower particles at a certain distance from the shower axis. To interpret experimental data, we thus have to know how showers induced by cosmic rays develop longitudinally and laterally in the atmosphere.

2.2.1 Longitudinal Shower Development

In fluorescent light detection experiments, the longitudinal shower profile is used to determine the shower energy. The electromagnetic energy is given by

$$E_{em} = \frac{E_c}{X_r} \int_s^\infty N(X) dX, \tag{2.18}$$

where E_c is the critical energy, X_r is the radiation length and $N(X)$ is the number of charged particles. Then E_{em} should be converted into the total energy by compensating for unseen energy - the energy channeled into neutrinos, high energy muons and nuclear excitation by hadrons, etc. However, in reality, often only a part of the shower profile is observed, because the detector can not cover the whole sky, or the air shower stops developing further when it reaches the ground level. Thus, we need to extend the shower profile at both ends.

Since extensive air showers were discovered, the development of electromagnetic cascades has been studied by many authors [91, 92, 93, 94], and it has been described in detail by Greisen and Rossi [95, 96]. The propagation of particles in the cascade is described by a cascade equation, and the equation can be solved under various

approximations. First of all, all processes except pair production and bremsstrahlung can be neglected. This is called 'Approximation A' and is not valid for low energy particles. In 'Approximation B', the ionization loss of electrons is taken into account, but it is a constant of E_c/X_r. One of the results of the cascade theory is given by Greisen [97]:

$$N(X) = \frac{\beta}{\sqrt{y}} \exp[\frac{X}{X_r}(1 - \frac{3}{2}\ln s)], \tag{2.19}$$

where $\beta = 0.31$, $y = \ln(E_0/E_c)$ and s is the shower age defined as

$$s = \frac{3 \cdot X}{X + 2 \cdot X_{max}}. \tag{2.20}$$

The number of particles increases until the shower reaches the maximum depth ($s = 1$ or $X = X_{max}$) and then decreases. After $s = 2$, the number of particles becomes very small and the shower profile in age looks symmetric. For a pure electromagnetic shower, $y = X_{max}/X_r$ as derived in the first section.

However, the analytical calculation is complicated even for an electromagnetic shower. And the solution shows only the average behavior of the showers, although the cascade equation can be calculated numerically. Thus, Monte Carlo simulations were developed to study the fluctuations in air showers. Based on Monte Carlo simulations using the scaling model for nuclear interactions, the longitudinal development of hadronic showers is found to be well represented by the so-called Gaisser-Hillas function:

$$N(X) = N_{max}\left(\frac{X - X_1}{X_{max} - X_1}\right)^{\frac{X_{max}-X_1}{\lambda}} e^{-(X-X_{max})/\lambda}, \tag{2.21}$$

where $N(X)$ is the number of charged particles, X_1 is the first interaction depth and $\lambda = 70$ g/cm^2 which has been regarded as the proton interaction length. However, this function is somewhat different from the original function given by [98]:

$$N(X) = S_0\frac{E_0}{\epsilon}e^{\frac{X_{max}}{\lambda}-1}\left(\frac{X - X_1}{X_{max} - \lambda}\right)^{\frac{X_{max}}{\lambda}-1} e^{-(X-X_1)/\lambda}, \tag{2.22}$$

with

$$N_{max} = S_0 \frac{E_0}{\epsilon} \tag{2.23}$$

$$X_{max} = X_r' \ln(\frac{E_0}{\epsilon}) \tag{2.24}$$

where S_0 is 0.045, X_r' is 36 g/cm^2, ϵ is 74 MeV and λ is 70 g/cm^2. Both Eq. (2.21) and Eq. (2.22) are identical only if X_1 is equal to λ, which is why λ is traditionally called the proton interaction length even though it is longer than the acceptable values at energies above 10^{17} eV.

In order to understand the Gaisser-Hillas function, let me introduce a statistical distribution rather than tracing the history of the function. A gamma distribution is used to describe random variables bounded at one end in the Poisson process. The general formula for the probability density function of the gamma distribution is given by

$$f(X) = \frac{1}{\lambda\Gamma(n)}\Big(\frac{X-\mu}{\lambda}\Big)^{n-1} e^{-(X-\mu)/\lambda}, \qquad \text{for } X \geq \mu, \tag{2.25}$$

where n is the shape parameter, μ is the location parameter and λ is the scale factor. For $\mu = 0$ and $\lambda = 70$, the distribution for integer n is given in Figure 2.8. If $\mu = 0$ and $n = 1$, the function becomes an exponential function:

$$f(X) = \frac{1}{\lambda} e^{-X/\lambda}. \tag{2.26}$$

This is the first interaction distribution when λ is the mean free path of the incident particles.

If $\mu = X_0$ and $n = m + 1$, the gamma distribution function becomes

$$f(X) = \frac{1}{\lambda\Gamma(m+1)}\left(\frac{X-X_0}{\lambda}\right)^m e^{-(X-X_0)/\lambda}. \tag{2.27}$$

This distribution is assumed to be proportional to the longitudinal shower development and to the distribution of the maximum depths. Later, it will be shown that this function also fits the distribution of X_{max} with the location parameter X_c, which is the lower limit of X_{max}. The longitudinal shower profile can be written as

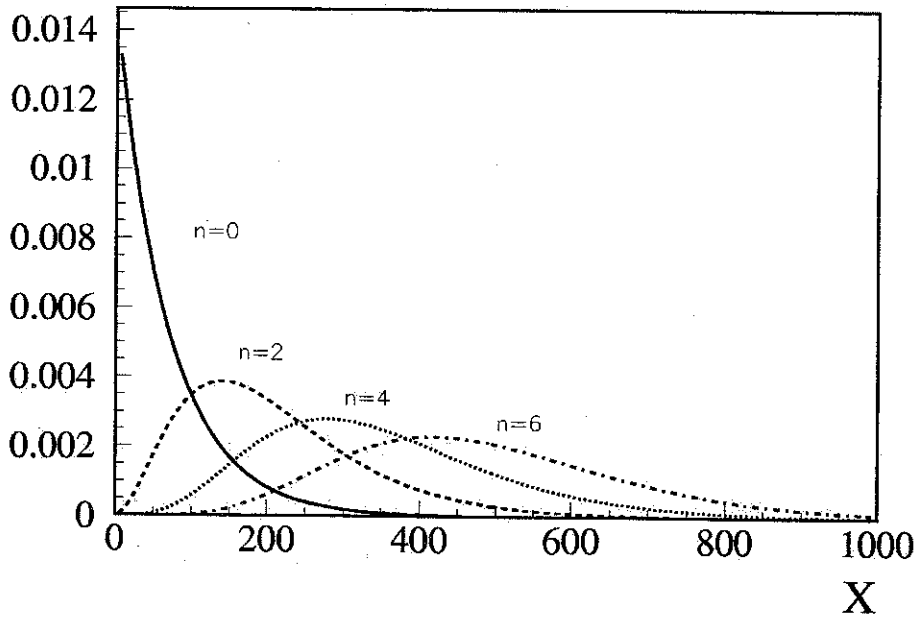

Figure 2.8: The gamma distribution for different n with $\lambda = 70$.

$$N(X) = N_0 \left(\frac{X - X_0}{\lambda} \right)^m e^{-(X-X_0)/\lambda}, \tag{2.28}$$

and

$$X_{max} = m\lambda + X_0, \tag{2.29}$$

$$N_{max} = N_0 m^m e^{-m}. \tag{2.30}$$

We can express this function by using other parameters as in the following:

$$N(X) = \left(\frac{X - X_0}{X_1 - X_0} \right)^{\frac{X_{max}-X_0}{\lambda}} e^{-(X-X_1)/\lambda}, \tag{2.31}$$

or

$$N(X) = N_{max} \left(\frac{X - X_0}{X_{max} - X_0} \right)^{\frac{X_{max}-X_0}{\lambda}} e^{-(X-X_{max})/\lambda}. \tag{2.32}$$

We have three different forms. The last one is exactly the same as the Gaisser-Hillas function if X_0 is X_1 where $N(X_0) = 0$ and $N(X_1) = 1$. X_0 has mostly negative values and λ is not a proton interaction length but a parameter depending on the mass and energy of the primary particle. The longitudinal profile of the particle number is similar to that of the energy deposition in an electromagnetic cascade, which is reasonably well described by [99]:

$$\frac{\mathrm{d}E}{\mathrm{d}t} = E_0 b \frac{(bt)^{a-1} e^{-bt}}{\Gamma(a)}, \tag{2.33}$$

where $t = X/X_r$. The longitudinal profile of the number of charged particles is proportional to that of the energy deposition, which is also proportional to the fluorescent light production.

The Greisen and Gaisser-Hillas functions describe electromagnetic and hadronic showers well, but the values of some parameters like λ or β are somewhat dependent on the mass of the primary particles. We will discuss the profile functions in detail in Chapter 4.

2.2.2 Lateral Distribution of Shower Particles

The lateral distribution of particles in air showers is thought to be crucial only for detector array experiments, but it plays a very important role in fluorescent light detection experiments, too. This is simply because the shower track is not just a straight line. It is a line with a lateral width depending on the stage of the longitudinal development of the shower. The ground detector arrays usually measure the number of muons or all charged particles and their arrival times by using plastic scintillators, water Cherenkov detectors, or muon counters. The total number of muons on the ground is a good estimator of the primary energy, because the number of muons attenuates more slowly than the number of electrons. However, muons are much less abundant and spread more widely than electrons, so a larger detector is required to measure the total number of muons.

The number density of electrons at a distance r from the shower axis is given by

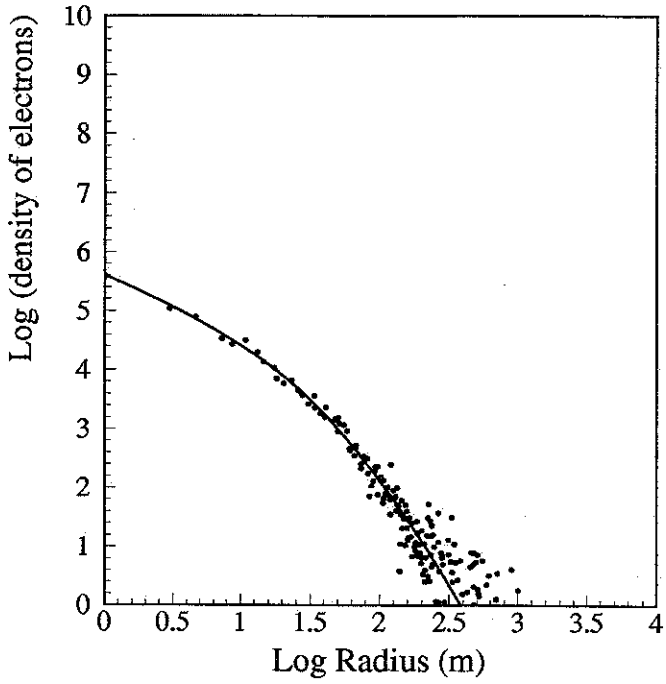

Figure 2.9: The lateral distribution of electrons for 10^{17} eV gamma showers generated by CORSIKA is compared with the NKG function.

$$\rho_e = N_e \frac{C_e(s)}{r_1^2 s_m^2} \left(\frac{r}{r_1 s_m}\right)^{s-2} \left(1 + \frac{r}{r_1 s_m}\right)^{s-4.5}, \tag{2.34}$$

with

$$C_e(s) = \frac{\Gamma(4.5-s)}{2\pi\Gamma(s)\Gamma(4.5-2s)}, \tag{2.35}$$

where $s_m = 0.78 - 0.21s$ is the modulation function [100, 101]. Eq. (2.34) is known as the Nishimula-Kamata-Greisen (NKG) function after dropping a term of N_e/r_1^2 with $s_m = 1$ [102]. r_1 is the Molière radius, which is defined as

$$r_1 = \frac{m_e c^2 (4\pi/\alpha)^{1/2}}{E_c} X_r, \tag{2.36}$$

where E_c is the critical energy and X_r is the radiation length. About 90 % of the energy of a shower is deposited inside a cylinder around the shower axis with a radius of r_1. Figure 2.9 shows the lateral distribution of electrons generated by the

CORSIKA air shower simulation package.

The lateral distribution of muons is independent of the shower age. The number density of muons as a function of the lateral distance r from the center of the shower is given by Greisen [103]:

$$\rho_\mu = N_\mu \frac{C_\mu}{r_0^2}\left(\frac{r}{r_0}\right)^{-0.75}\left(1+\frac{r}{r_0}\right)^{-2.5}, \tag{2.37}$$

where $C_\mu = \Gamma(2.5)/2\pi\Gamma(1.25)\Gamma(1.25)$ and r_0 is 320 m. However, the Akeno group found that Eq. (2.37) overestimates the muon ($\geq$ 1 GeV) density beyond 800 m and proposed a modified function [35]:

$$\rho_\mu = N_\mu \frac{C'_\mu}{r_0^2}\left(\frac{r}{r_0}\right)^{-0.75}\left(1+\frac{r}{r_0}\right)^{-2.52}\left\{1+\left(\frac{r}{r'_0}\right)^3\right\}^{-0.6}, \tag{2.38}$$

where $C'_\mu = 0.325$, r_0 is (266 $\pm$ 32) m and $r'_0 = 800$ m. Instead of $(1+(r/800)^3)^{-0.6}$, the Yakutsk group used $(1+r/2000)^{-1}$ and considered the zenith angle in their function [104].

The relation between N_e and E_0(eV) is given by [105]:

$$E_0 = 3.9\times 10^{15}\left(\frac{N_e}{10^6}\right)^{0.9}. \tag{2.39}$$

Or, instead of N_e, N_μ can be used [35]:

$$E_0 = 2.16\times 10^{18}\left(\frac{N_\mu}{10^6}\right)^{1.19}. \tag{2.40}$$

However, the particle density at 600 m from the shower axis is adopted by detector array experiments because this quantity is not sensitive to the lateral distribution function, and because it only weakly depends on the hadronic interaction model and on assumptions about primary mass composition [106, 107]. Thus, the primary energy in eV is expressed in terms of the density of the charged particles [105],

$$E_0 = 2.0\times 10^{17}\rho_e(600)^{1.0}, \tag{2.41}$$

or in terms of that of the muons at $\sec\theta = 1$ [35]:

$$E_0 = 2.22 \times 10^{18} \rho_\mu (600)^{1.22}. \tag{2.42}$$

For inclined showers, the density has to be corrected.

2.2.3 Energy Spectrum of Shower Particles

Based on simulation studies with 100 GeV photon induced showers, the integral energy spectrum is given by Hillas [108]:

$$T(E) = \left(\frac{0.89E_0 - 1.2}{E_0 + E}\right)^s (1 + 10^{-4} sE)^{-2}, \tag{2.43}$$

where $E_0 = 44 - 17(s - 1.46)^2$ if $s \geq 0.4$ or 26 if $s < 0.4$ and E is the kinetic energy in MeV. Particles of energies below 15 MeV are not included in this study.

The energy spectrum of shower particles is used to calculate how much Cherenkov light is produced. The threshold energy for Cherenkov radiation is given by

$$E_{th} = \frac{0.511\text{MeV}}{\sqrt{2(1-n)}}, \tag{2.44}$$

where n is the index of refraction. E_{th} is about 21 MeV at sea level. Therefore, the Hillas's energy spectrum works fine for generating Cherenkov light. However, the function is no longer valid for the calculation of fluorescent light production, which has a much lower threshold energy. The average energy spectra of shower particles induced by protons are shown in Figure 2.10 at the various stages of the shower development and are fitted to a Gaussian function:

$$\widetilde{n}_e(E, S) = \frac{1}{\sigma(S)\sqrt{2\pi}} \cdot e^{-\frac{(E-\mu(S))^2}{2\sigma(S)}}, \tag{2.45}$$

where E is the energy of electrons in $\log_{10}(\text{keV})$ and S is the shower age. Figure 2.11 shows the mean and sigma of the Gaussian function at various shower ages.

Fortunately, the fluorescent light efficiency does not depend strongly on the particle's energy. Thus, the average energy of shower particles at different stages of the shower development can be used approximately for fluorescent light calculation.

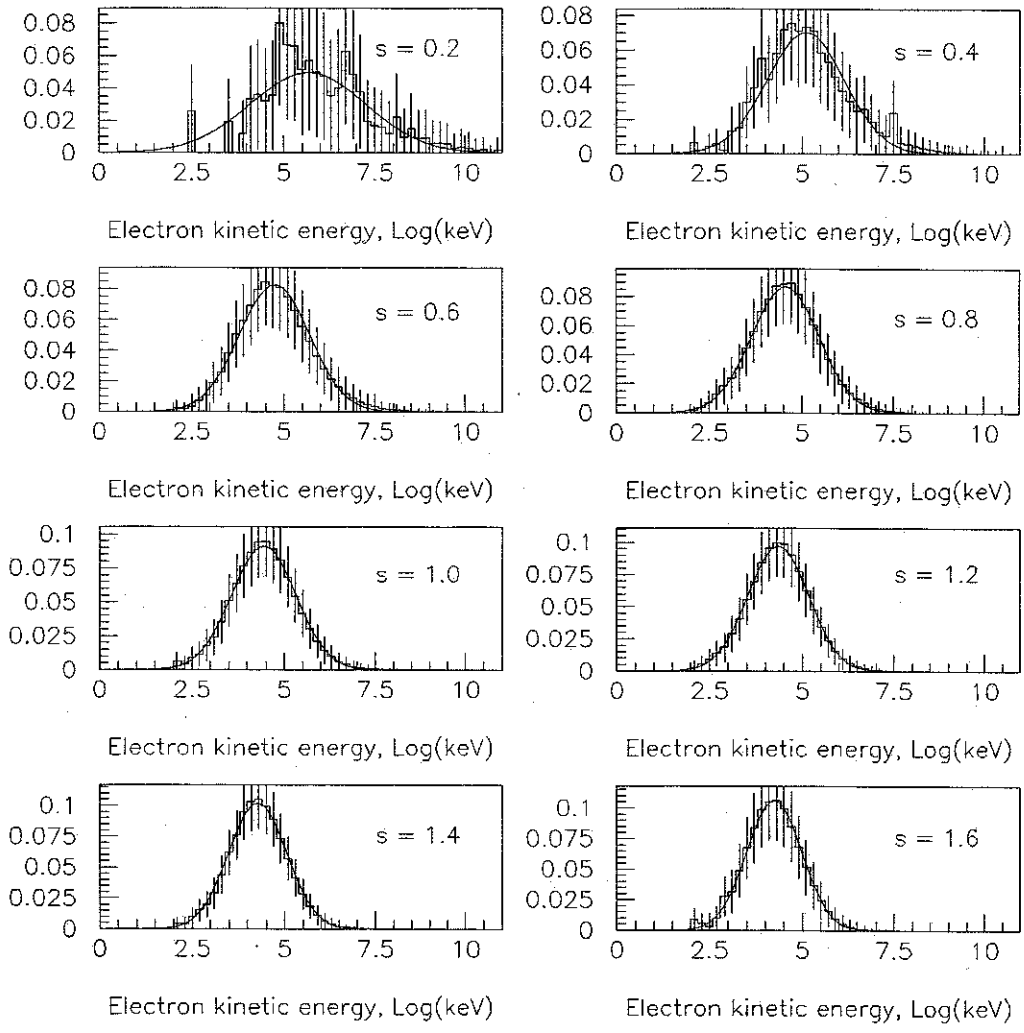

Figure 2.10: Energy spectra of electrons at various ages for 10^{17} eV proton showers.

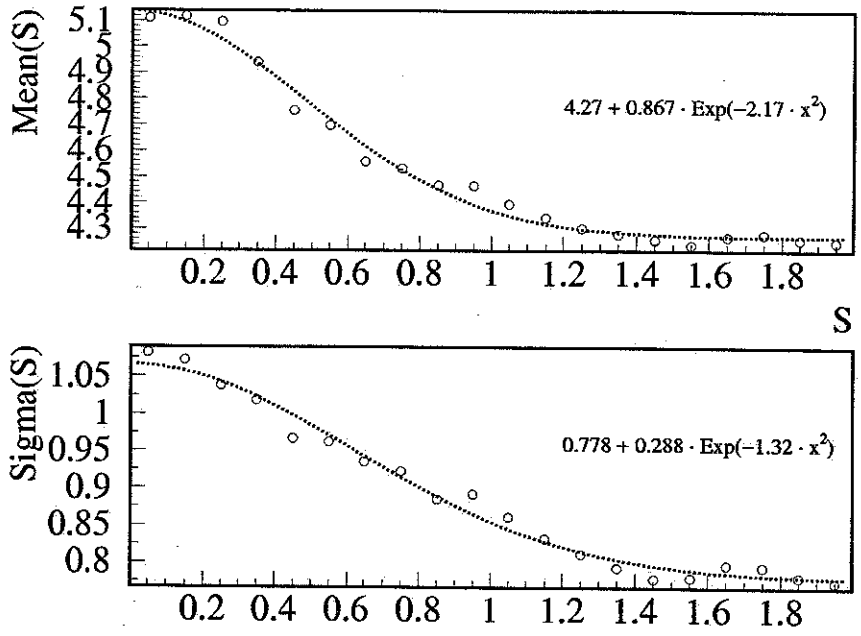

Figure 2.11: The mean and sigma of a Gaussian fit to the energy spectrum of electrons as a function of shower age for 10^{17} eV proton showers.

2.3 Observation Techniques of Air Showers

Below about 10^{15} eV, the flux of cosmic rays is high enough for detectors mountable on satellites or balloons at the top of the atmosphere. Detection techniques are similar to the ones used in high energy particle physics experiments. Calorimeters, emulsion stacks, solid state detectors, synchrotron radiation detectors and transition radiation detectors are flown on balloons, satellites or space shuttles. They collect data on X rays, gamma rays, the chemical composition of cosmic rays around the knee, and the abundance of antimatter in cosmic rays.

Above 10^{15} eV, however, the flux is too low, and a direct measurement of cosmic rays is not practical. Experiments have to be earth-based, which means that it is not possible to observe the primary particle directly, but only the extensive air showers induced by primary particles in the atmosphere. There are several different detection methods. One way is to detect secondary particles on the ground level

using scintillation detectors or muon counters. Another way is to collect the light generated by the secondary particles as Cherenkov light or fluorescent light from excited nitrogen molecules. As the measurement of the primary particle is indirect, the determination of the energy and mass of the primary particle is considerably more complicated than in direct measurements, and the measurement depends somewhat on the hadronic interaction model used in the analysis. Moreover, with the lack of a 'test beam,' it is difficult to calibrate detectors. Thus, the indirect measurement has larger systematic errors than the direct measurement.

Particle Detector Arrays

Extensive air showers with many particles arriving on the ground can be detected with different kinds of particle detectors. The most common are scintillation counters, which can measure the arrival times of particles. Other common devices include water Cherenkov counters, resistive plate chambers and a variety of position-sensitive devices, which allow us to measure particle directions. These tracking detectors include different types of drift chambers, streamer tube detectors, and Geiger tube detectors. Magnets can be used to determine the momentum of secondary particles, but nuclear emulsion has the highest resolution of any technique yet developed. The disadvantage of this technique is a low sampling area because of the large distances between detectors. Also, the lateral distribution of shower particles varies at different stages of the shower development, depending on the hadronic interaction model. Thus, the primary energy and mass deduced from the observed lateral distribution on the ground level are model-dependent.

To detect an extensive air shower, the detector has to cover a broad area, depending on the energy of the primary particle. Communication between detectors, which can be spaced meters or even kilometers apart, is necessary to detect the extensive air showers.

Cherenkov Light Detectors

Cherenkov light generated by charged particles in air showers can be detected at ground level. Charged particles moving through the atmosphere with a velocity larger than the local speed of light (the vacuum speed of light divided by the refractive index (n) of the air) emit Cherenkov light. The light is emitted in a narrow cone around the direction of the particle. The opening angle θ_{max} is a function of the index of refraction, and is given by $\cos^{-1}(1/n)$. It increases downwards, but is always less than about 1.3° at Standard Temperature and Pressure (STP: 20°C at 1 atmosphere). From each part of the particle track the Cherenkov light arrives on the ground in a ring. In the air shower, most secondary particles will stop or decay before they reach the ground. The Cherenkov light from those shower particles moving faster than the local speed of light overlaps on the ground.

Blackett was the first to realize, in 1948, that air showers would produce sufficient amounts of Cherenkov light to be detected. In 1952, Galbraith and Jelley succeeded in detecting the Cherenkov light from air showers. Since then, Cherenkov light has been used to study the properties of cosmic rays. In 1977, the imaging technique was proposed to distinguish hadronic and electromagnetic showers [109]. This technique also enables us to map the shower development. In searching for sources of TeV energy gamma rays, this technique is essential to suppress the cosmic ray background.

Fluorescent Light Detectors

Showers can be detected at even larger distances by the fluorescent light which is emitted isotropically by nitrogen molecules when charged particles pass nearby. Most of the light is emitted in several bands from 300 to 400 nm, as shown in Figure 2.12. The fluorescent light yield is about 4 to 5 photons per meter per ionizing particle. Telescopes with photomultiplier tubes can see the track of air showers through the atmosphere. This technique provides the largest detector aperture for a given instrument size.

Originally, this technique was developed to detect the yield of nuclear explosion

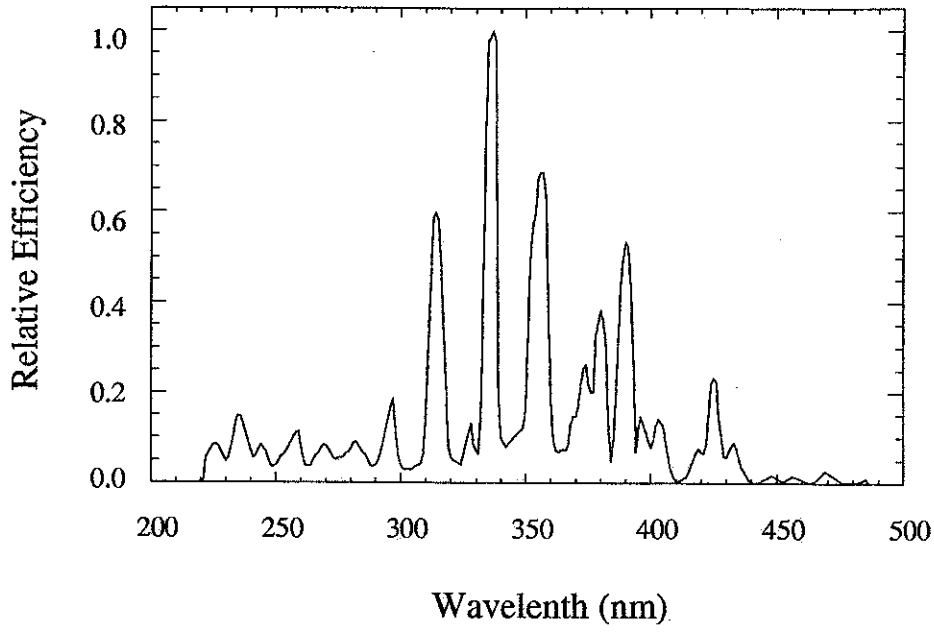

Figure 2.12: Spectrum of nitrogen fluorescent light.

tests in the early 1960s. The first attempt to detect the fluorescent light caused by air showers was made by a group led by Kenneth Greisen at Cornell University in the 1960s [110, 111]. Unfortunately, the attempt failed because the fluorescent light was too weak to be detected by the group's 0.1 m^2 Fresnel lenses and because the weather conditions in Ithaca, New York, were not conducive to the detection of fluorescent light.

The method was first successfully used in the Fly's Eye experiment. The three prototype fluorescence detectors were tested with the Volcano Ranch ground array in New Mexico and were able to observe air showers in coincidence with the ground array in 1976.

Chapter 3

THE HiRes DETECTOR

The HiRes detector is a fluorescent light detector that consists of three parts: the atmosphere as a calorimeter, a telescope and a system of electronic components. To collect weak fluorescent light, large mirrors and photo-multiplier tubes are used and the night sky noise is suppressed using UV filters. Finally, the tube signal is amplified and used to calculate the number of photoelectrons and trigger time for triggered events. In this chapter, we describe the configuration of the detector and the means for calibrating the detector.

3.1 High Resolution Fly's Eye Detector

The first successful fluorescent light detector, Fly's Eye, operated from 1981 to 1992. The High Resolution Fly's Eye (HiRes) experiment is an upgraded version with larger mirrors, smaller photo-multiplier tubes (PMTs) and more sophisticated electronics. A prototype detector was tested and operated from 1993 to 1996. HiRes-I and HiRes-II were completed in 1997 and in 1999, respectively. Figure 3.1 shows the relative location of the two sites.

The HiRes prototype detector was situated on the top of Little Granite Mountain at the Dugway Proving Ground, Utah. The geographical location was 40° 11′ 43″ latitude, 112° 50′ 9″ longitude and 1,957 m above sea level (an atmospheric depth of 860 g/cm^2). The detector overlooked the Chicago Air Shower Array (CASA) and the Michigan Muon Array (MIA) about 3.3 km away from HiRes. MIA consisted of 16

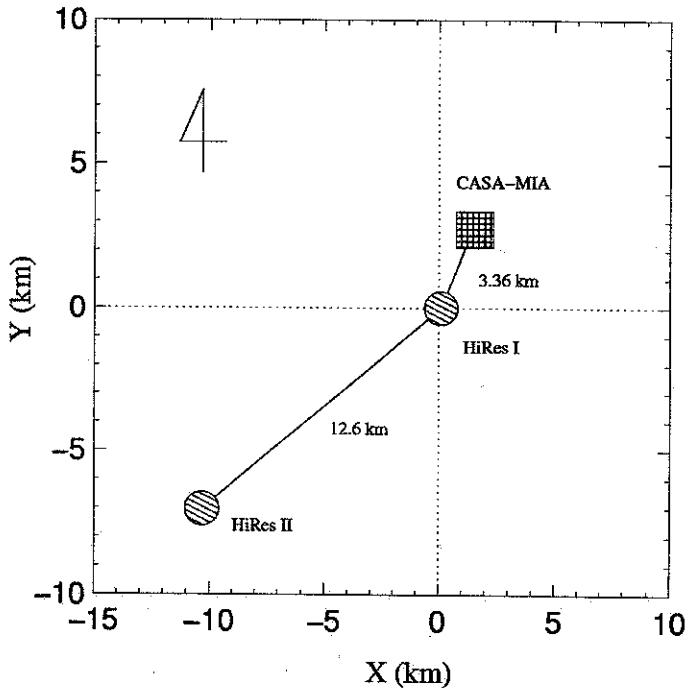

Figure 3.1: CASA, MIA and HiRes detectors at Dugway, Utah

patches of 64 scintillation counters buried 3 m under ground, which measure muon arrival times and recorded all hits occurring within 4 μs of the system trigger. CASA, on the surface, consisted of 1,087 scintillation detector stations. The HiRes prototype detector collected data with fourteen mirrors from August 1993 to October 1996. The detector pointed to the north-east with elevation angles of 3° to 70°. The field of view of the detector is shown in Figure 3.2. HiRes-MIA hybrid data was taken until four months before the HiRes prototype was dismantled. Meanwhile, four mirrors had been installed at Camel's Back Ridge in September 1994. Stereo data was taken for about two years.

In 1997, the HiRes prototype detector was relocated and seven more mirrors were added. HiRes-I now consists of twenty-one mirrors and covers 3° to 17° in elevation with full azimuthal angle. It is designed to detect distant air showers induced by the highest energy cosmic rays and to maximize the aperture by working in stereo with HiRes-II. Thus, the integration time of tube signals for HiRes-I (5.6 μs) is set to be longer than that for the prototype detector (1.2 μs).

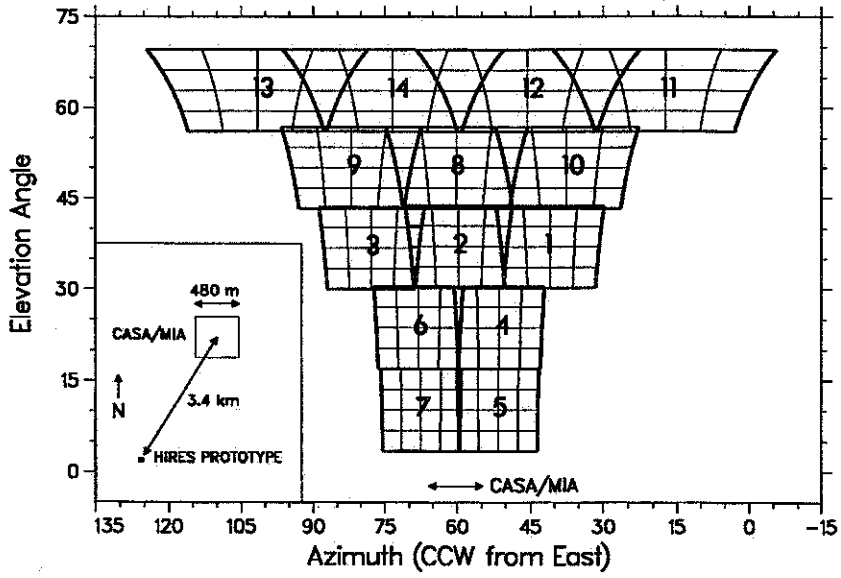

Figure 3.2: The field of view of the HiRes prototype detector.

HiRes-II was designed in 1995 and completed at Camel's Back Ridge in 1999. It consists of forty-two mirrors covering 3° to 31° in elevation with full azimuthal angle. Flash Analog to Digital Converter (FADC) electronics were adopted as opposed to the Sample and Hold (S/H) electronics of HiRes-I. Each PMT cluster has sixteen FADC cards which receive signals from each vertical column of sixteen PMTs. PMT signals are digitized every 100 ns. This enables us to choose the integration time for each tube based on shower geometry to optimize the ratio of signal to noise. By this process, shower geometry reconstruction is improved.

3.2 Detector Components

3.2.1 Mirrors

The mirror production process is described in [112]. Each mirror has a 2 m diameter and consists of four segments in a clover leaf pattern. The mirrors were formed by heating glass blanks on a concave ceramic mold. The area of each mirror is 4.18 m^2

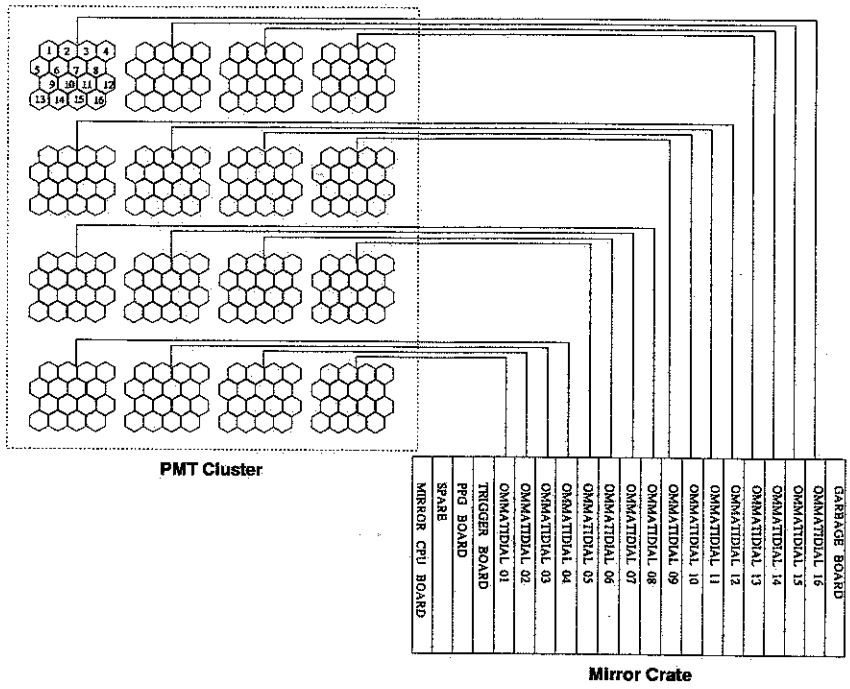

Figure 3.3: PMT cluster box

and the area obscured by a PMT cluster is 3.75 m^2. The radius of curvature (R) is 474 cm. The distance between PMT cluster and mirror is set to 0.97 × (R/2) to minimize the spot size. Because the mirror shape is spherical rather than parabolic, light can not be focused on the focal plane. The average reflectivity at 337 nm is 85 %, which was measured with the aid of a pulsed nitrogen laser.

3.2.2 PMT Clusters

The PMT clusters (Figure 3.3) are held in the focal plane of the spherical mirrors and have 256 hexagonal PMTs of 40 mm diameter behind an UV filter. A temperature sensor is located at the center of each cluster and a cooling fan is held at the top.

The photons reflected by the spherical mirrors go through a UV bandpass (300 - 400 nm) filter which reduces the night sky background noise by a factor of 7 to 8 [113]. Figure 3.4 shows the transmission curve of the UV filters. The average transmission is about 85.5 % at 355 nm.

The PMTs convert the fluorescent light into an electrical signal. Half of the mirrors

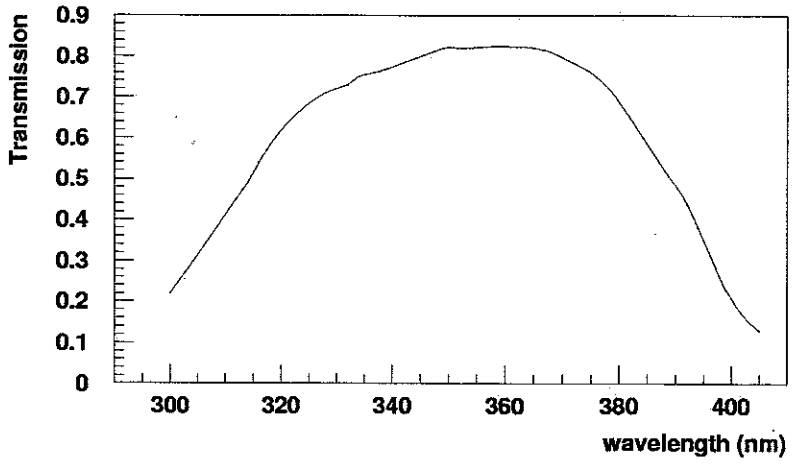

Figure 3.4: UV filter transmission.

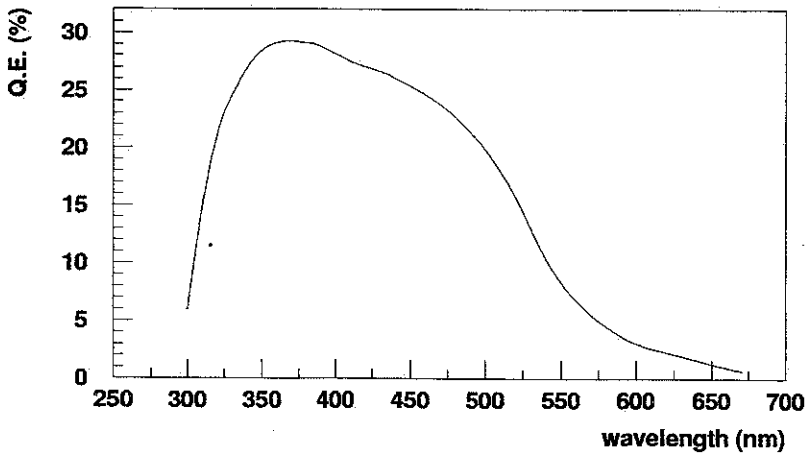

Figure 3.5: The quantum efficiency of a PMT (Philips XP 3062/FL).

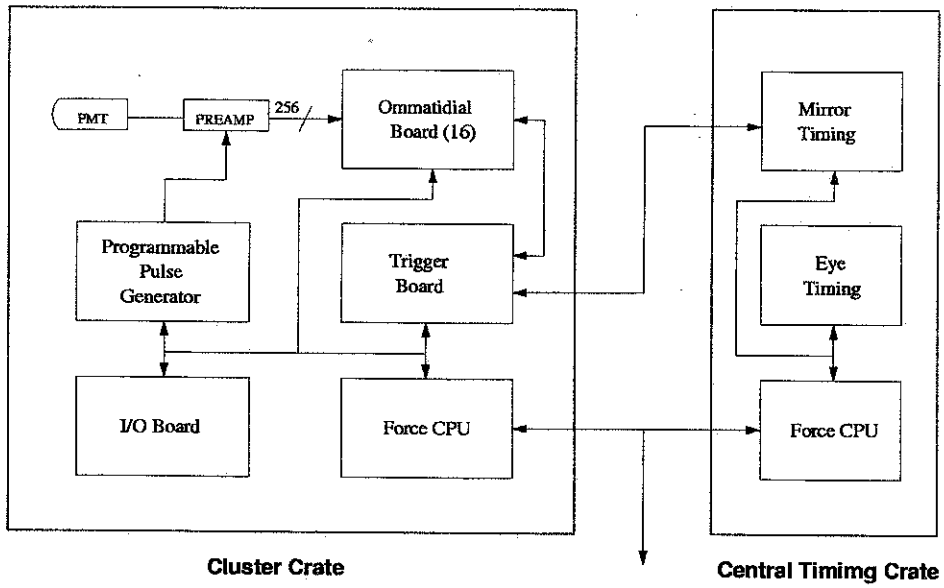

Figure 3.6: The board diagram [114]. To diagnose and calibrate the electronics, a Programmable Pulse Generator (PPG) which produces variable square pulses is used.

use Philips XP 3062/FL PMTs, and the remaining mirrors use EMI 9974 KAFL PMTs. The PMTs are arranged in sixteen sub-clusters of sixteen PMTs each and wrapped in magnetic shielding metal. The PMT quantum efficiency was measured for all PMTs used in the HiRes detector. Figure 3.5 shows the wavelength dependence of the quantum efficiency. The pre-amplifier connected to the PMTs adds a gain of 10 % onto the PMT pulse and generates a differential signal which can suppress DC sky noise. A 2 kV 100 mA supplier provides about 1,100 V to the PMTs.

3.2.3 Electronics

The electronics must filter out night sky background noise while responding to a wide range of signal characteristics that identify the fluorescent light tracks of extensive air showers [114]. The noise is caused by stars, diffused galactic radiation, Cherenkov light from small showers, and particles striking the PMTs. The minimum dynamic range, accuracy of the pulse integration and timing electronics are set by the required detector aperture and energy sensitivity. Figure 3.6 shows the system block diagram.

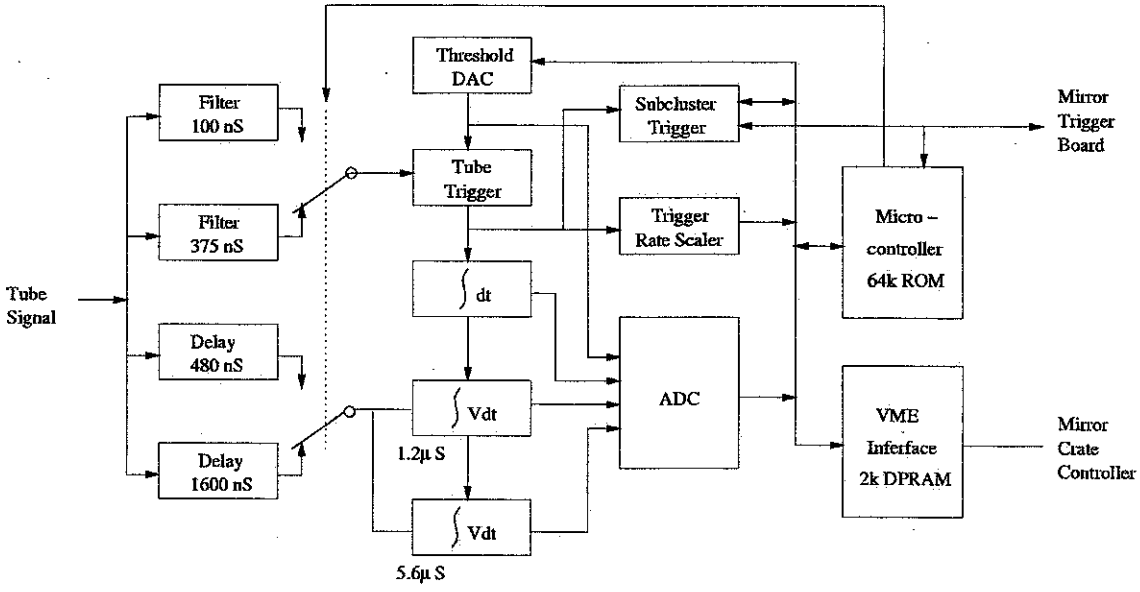

Figure 3.7: The Ommatidial Board (Rev.3).

Ommatidial Board

The ommatidial board handles PMT triggers and digitizes their integrated charges and the times when the signals of PMTs rise above threshold. There are two channels. Channel A has 1.2 μs integration time with an RC filter and channel B has 5.6 μs integration time with an LC filter. For at least 25 μs after the signal rises above threshold, the PMT may not re-triggered. Figure 3.7 shows the block diagram of the ommatidial board.

The trigger rate of each PMT is monitored periodically and the trigger threshold is adjusted to maintain the trigger rate near a compromise between sensitivity and PMT trigger dead time.

Trigger Board

The event trigger pattern is handled by the trigger board. A subcluster trigger is formed when a pattern of PMT triggers within the subcluster matches that of a trigger look-up table requiring at least three triggered PMTs, two of which must be adjacent. The mirror trigger requires at least two subclusters to trigger. When this

happens, the hold-off time for all triggered tubes is extended an additional 10 μs. The mirror trigger signal is sent to adjacent mirrors which do not require their own mirror trigger conditions. This signal is also sent to the central timing crate that records the absolute mirror trigger time.

Central Timing Crate

The central timing crate records the mirror trigger time and generates timing pulses to the mirrors. The prototype detector had WWVB[1] clocks which only had a resolution of 1 ms. These were replaced with Global Positioning System (GPS) clocks in November of 1994. The GPS clocks produce a synchronization pulse. The relative accuracy is reduced to about 10 ns. The central timing crate is also used to fire a Xenon flasher which is situated between HiRes and CASA-MIA. The HiRes timing system is described by Wilkinson [115].

3.2.4 The Atmosphere as a Calorimeter

The atmosphere consists mainly of N_2 (78.1%), O_2 (21.0%) and Ar (0.9%), and can be roughly divided into five layers [116]. In the lowest one, the 'troposphere', the temperature decreases with altitude. Air in this layer is heated from the ground up. This is the layer in which most clouds occur. The troposphere extends up to about 18 km. On the surface of the earth, aerosols of microscopic liquid or solid particles, such as smoke, dust, fog and smog, tend to remain dispersed rather than to settle. The size of aerosol particles ranges from 10^{-7} to 10^{-4} cm in diameter. Above the troposphere is the 'stratosphere'. The upper stratosphere contains the ozone layer. The layer from 50 to 80 km, called the 'mesosphere', is where most meteors burn up. The layer above 80 km reflects radio waves of certain frequencies back to earth because of the relatively high concentration of ions in this layer, extending to an altitude of 640 km. It is called the 'ionosphere'. Because the temperature in this layer reaches about 1,200°C, it is also called the 'thermosphere'. The region beyond

[1]NIST radio station WWVB is located in Colorado and continuously broadcasts time and frequency signals at 60 kHz.

the thermosphere is called the 'exosphere', which extends to about 9,600 km; here atoms and molecules escape from the earth. Most of the first interactions of cosmic rays occur in the troposphere and stratosphere. The ozone layer has been taken into account in our detector simulation and shower reconstruction codes.

HiRes detects fluorescent light produced by particles in air showers. The amount of light detected depends on how light is scattered and absorbed by air molecules or aerosols. If the wavelength of light is about equal to the size of the particle, Mie scattering occurs. If the particle is smaller than the wavelength of light, there will be Rayleigh scattering. Rayleigh scattering is well understood, but Mie scattering problems are very difficult to solve except in the case of a few simple geometries. In Rayleigh scattering, light scatters in all directions without changing the frequency of the scattered light. The scattering probability strongly depends on the wavelength ($\propto \lambda^{-4}$) and the scattering angle is proportional to $1 + \cos^2(\theta)$. In Mie scattering, the wavelength dependence and angular distribution of the scattered light depend on the size, shape and dielectric constant of the aerosols. The scattering probability is proportional to λ^{-1} and the angular distribution is strongly peaked in the forward direction.

3.3 Detector Calibration

Calibration of experimental equipment is very important to obtain meaningful quantities from raw data. However, unlike high energy physics experiments, the calibration of our detector has some difficulties. The huge atmosphere as our calorimeter is not controllable and is constantly changing, while the calorimeters used in accelerators are well understood and can be tested using well known energy sources. In particular, the aerosol scattering which plays a very important role in light propagation is dependent on the size of the aerosols and the wind speed. Thus, the atmospheric conditions need to be monitored at all times.

3.3.1 PMT Calibration

For a given PMT signal (anode current), we should know the corresponding number of fluorescent photons striking the surface of the PMT. In order to calibrate the absolute gain and quantum efficiency of PMTs, we use an Argon laser (351 or 364 nm) or a He/Cd laser (325 nm). The wavelengths are chosen to match the window of the UV filter for nitrogen fluorescent light. The quantum efficiency of the PMT is measured as a function of wavelength, as shown in Figure 3.5. This varies slightly from tube to tube, depending on the cathode coating.

The absolute anode sensitivity (A/W) is measured. The anode sensitivity S is a function of the wavelength λ of an incident photon and the applied voltage V:

$$S(\lambda, V) = \frac{I_{anode}}{P_{ph}} = \frac{e}{hc}\lambda\eta(\lambda)G(V) \tag{3.1}$$

where $G(V)$ is the tube gain and $\eta(\lambda)$ is the quantum efficiency. The intensity of the laser beam diffused by a Teflon cylinder is measured by a diode calibrated by the National Institute of Science and Technology (NIST). This provides an absolute calibration. The typical intensity is 8×10^6 photons/cm^2 (4.5 pW/cm^2) at 350 nm. Unfortunately, we do not know the wavelength of incoming photons in the real experiment. Thus, we take the average value for nitrogen fluorescent photons. Then the gain (or sensitivity) is a function of voltage only:

$$G(V) = e^{\alpha} \cdot V^{\beta}, \tag{3.2}$$

where $\alpha = -31.70 \pm 0.770$ and $\beta = 5.89 \pm 0.14$ at $\lambda = 351$ nm. The voltage is varied through four steps at seven points across the PMT surface.

To measure the active area of the PMT, the laser light (1 mm diameter) is focused to a sharp point on the PMT surface. The active area is measured by summing the areas of all points which pass a minimum response cut. Thus, the tubes are characterized by active area and gain (or sensitivity).

PMTs are required to have a uniform response within 10 % over the face of the

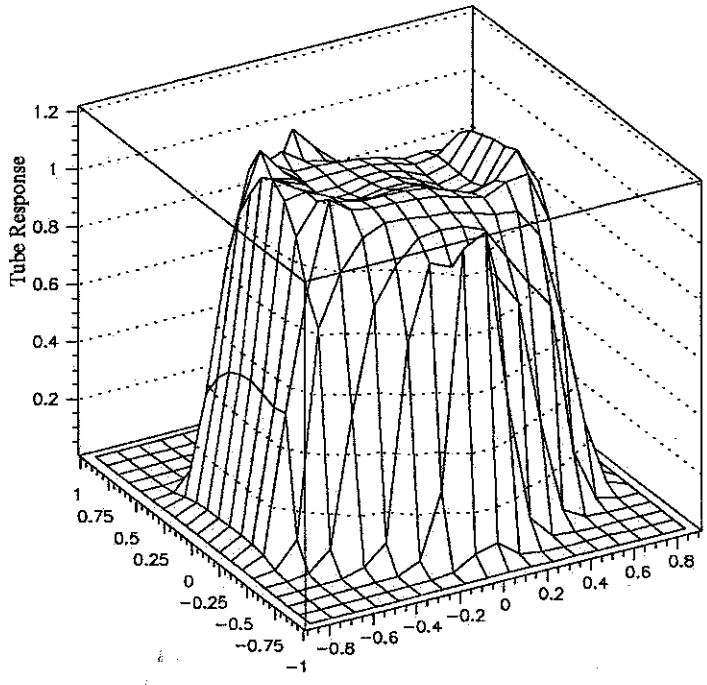

Figure 3.8: The tube response profile in arbitrary units.

tube, except for the area within 3 mm of the edge. Figure 3.8 shows the tube response profile.

3.3.2 Optics Calibration

The absolute mirror reflectivity starts at about 90 % when the mirrors are washed. After several months, the average reflectivity over the wavelength band of 300 to 400 nm falls to about 82 %. The mirror reflectivity can be measured every night by comparing tube response with two different diffusers of YAG laser light as shown in Figure 3.9.

The average transmission of UV filters is about 85.5 % at 355 nm. The transmission factors for each mirror are shown in Table 3.1. Figure 3.10 shows the fluorescent light spectrum resulting from a UV transmission filter and photocathode of a PMT. Eventually, photons of any wavelength within the resultant spectrum are converted into photoelectrons with corresponding efficiencies.

Mirror Number	UV filter transmission		Sensitivity(A/W)	
	Average	RMS	Average	σ
1	0.8574	0.0262	11,880	162.1
2	0.8057	0.0187	15,000	208.9
3	0.7481	0.0170	12,070	172.2
4	0.8979	0.0278	11,700	117.9
5	0.9028	0.0300	9,848	175.6
6	0.8615	0.0063	14,240	136.3
7	0.8937	0.0282	11,920	178.9
8	0.8555	0.0181	12,990	157.5
9	0.8682	0.0171	12,630	183.8
10	0.9006	0.0125	11,200	178.3
11	0.8417	0.0238	10,630	196.6
12	0.8485	0.0224	13,450	199.6
13	0.8365	0.0195	10,090	143.1
14	0.8542	0.0199	11,650	232.3
Mean	0.8554	0.0205	12,093	147.8

Table 3.1: The UV filter transmission and sensitivity after correction for the UV filter transmission for each mirror.

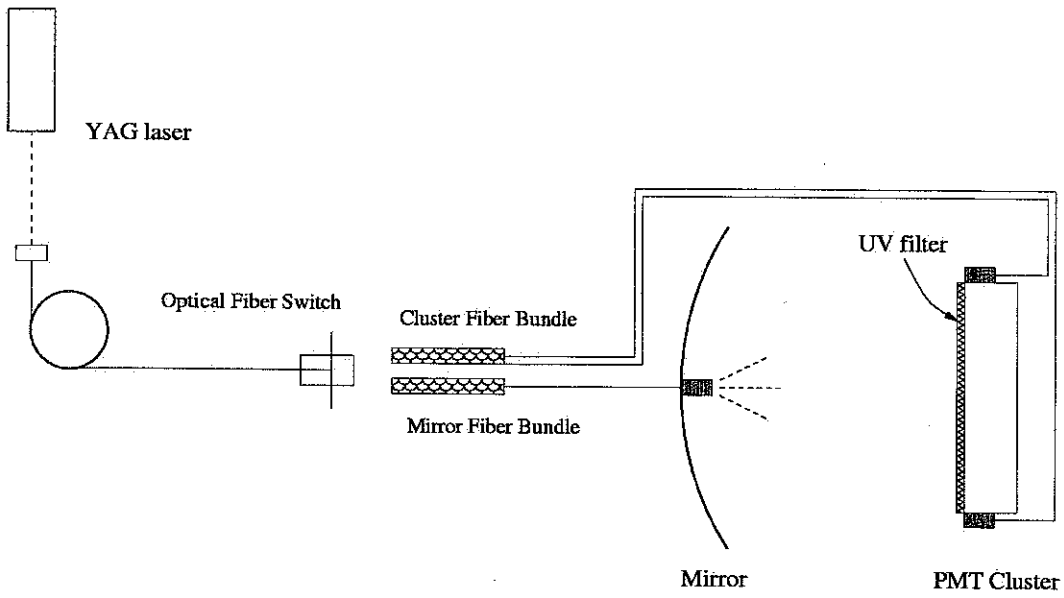

Figure 3.9: The YAG laser delivers light to each mirror through optical fibers. Then, a diffuser distributes uniform light onto the mirror or directly to the surface of the PMT cluster.

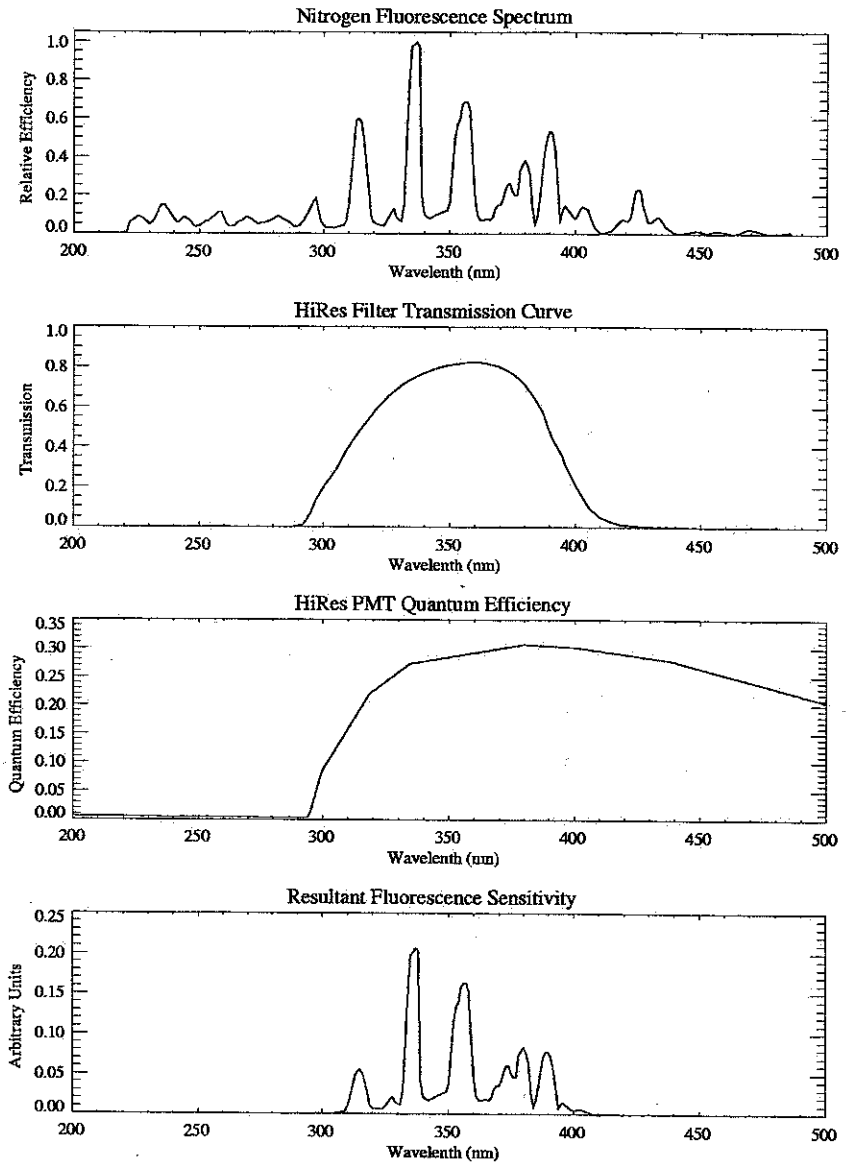

Figure 3.10: The fluorescent light spectrum before and after considering the UV filter transmission and the quantum efficiency.

3.3.3 Electronics Calibration

Pre-amplifier

The signal is amplified by a pre-amplifier which has nonlinear gain. Thus, a programmable pulse generator (PPG) is used to check the gain. The PPG generates pulses of various width and amplitude before and after the operation of the detector. The gain of the pre-amplifier is given by

$$G_{pre} = G_{asym} \times (1 - e^{\alpha + A}/\beta), \tag{3.3}$$

where α, β and G_{asym} are constants. A is the amplitude of the signal in volts.

Pedestal and Noise

Three hundred snapshots are taken each minute in a free trigger mode. The tube signals are integrated with charge to digital converters (QDCs) for two different time periods. The integration time is 1.2 μs for channel A and 5.6 μs for channel B. Then, pedestal values are obtained from the mean of the QDC values.

The photoelectrons resulting from the sky noise follow a Poisson distribution. Thus, the standard deviation of the number of photoelectrons (N_{pe}) is given by $\sqrt{N_{pe}}$. When we assume that the fluctuation of charge in each channel is caused by sky noise and that the number of QDCs (N_{QDC}) is proportional to N_{pe}, the mean μ and standard deviation σ of QDCs are given by

$$\mu_{QDC} = \kappa N_{pe}, \tag{3.4}$$

$$\sigma_{QDC} = \kappa' \sqrt{N_{pe}}, \tag{3.5}$$

where κ, κ' and α are constants. Thus, the number of photoelectrons can be obtained by

$$N_{pe} = \alpha \mu_{QDC}^2 / \sigma_{QDC}^2, \tag{3.6}$$

where $\alpha = 1.2$ comes from the fluctuation of the gain [117]. $\Delta gain/gain$ was found to be about 0.46 [118]. The electronics noise was obtained from the QDC distribution for PMTs shielded from night sky. When the PMTs were exposed to the night sky, the combined electronics and sky noise was measured and found to be 40 photoelectrons in channel A and 200 photoelectrons in channel B.

3.3.4 Atmospheric Calibration

As a calorimeter, the atmosphere is large enough to observe extensive air showers induced by cosmic rays. However, it is not simple to calculate how much light is produced by shower particles and how they propagate to the detector through the atmosphere. It is very important to know the characteristics of the atmosphere in determining the primary energy and detector aperture. The absorption of light in the region of 300 to 400 nm is negligible compared with scattering. Since the concentration of aerosols in the atmosphere changes over time, it is necessary to monitor the changes in the aerosol component of the atmosphere at frequent intervals.

Weather Code

Table 3.2 shows the weather code for the HiRes prototype data. The weather codes are recorded manually every hour, and filed in 'parts', each of which contains about two hours of data. The data is filtered to eliminate noise events, since most events are triggered by noise. Thus, all events after filtering are likely to be cosmic rays. Figure 3.11 shows the trigger rate distribution for all parts and for good weather parts, which have the weather code of zero for all digits. There is no significant difference between them. We may interpret this in two ways. First, the weather code may not be useful in understanding the atmospheric conditions because the code merely reflects cloud coverage at hourly intervals. It does not tell us about aerosol size, sky temperature or wind speed. Secondly, the weather conditions may not be crucial for the HiRes prototype detector, because the detector has a short time window so that only close events can be observed.

Digit	Weather condition
1st Frost	0 : no frost on tubes 1 : frost on tubes
2nd Atmospheric clarity	0 : negligible scattering 1 : moderate scattering 2 : heavy scattering 3 : socked in
3rd Overhead clouds in FOV	0 : no clouds visible 1 : $< 1/2$ sky cloudy 2 : $> 1/2$ sky cloudy
4th Horizon cloudiness	0 : no clouds visible 1 : clouds visible
5th Overhead cloudiness (all sky)	0 : no clouds visible 1 : $< 1/4$ sky cloudy 2 : $1/4 - 1/2$ sky cloudy 3 : $1/2 - 3/4$ sky cloudy 4 : $> 3/4$ sky cloudy

Table 3.2: The weather code for HiRes prototype data

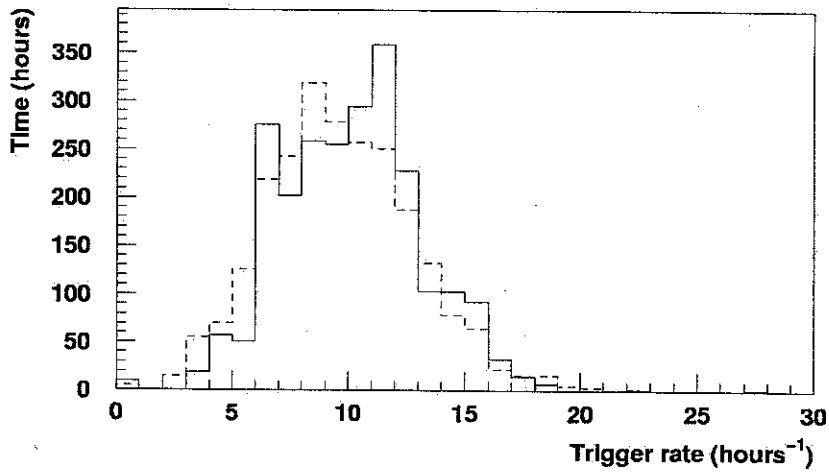

Figure 3.11: The trigger rate distribution for all parts (dashed line) and good weather parts (solid line) of HiRes prototype data. The distributions are weighted by the time period for each part. The total number of parts is 1505. 190 parts are selected as the good weather parts which have a weather code of zero for all digits.

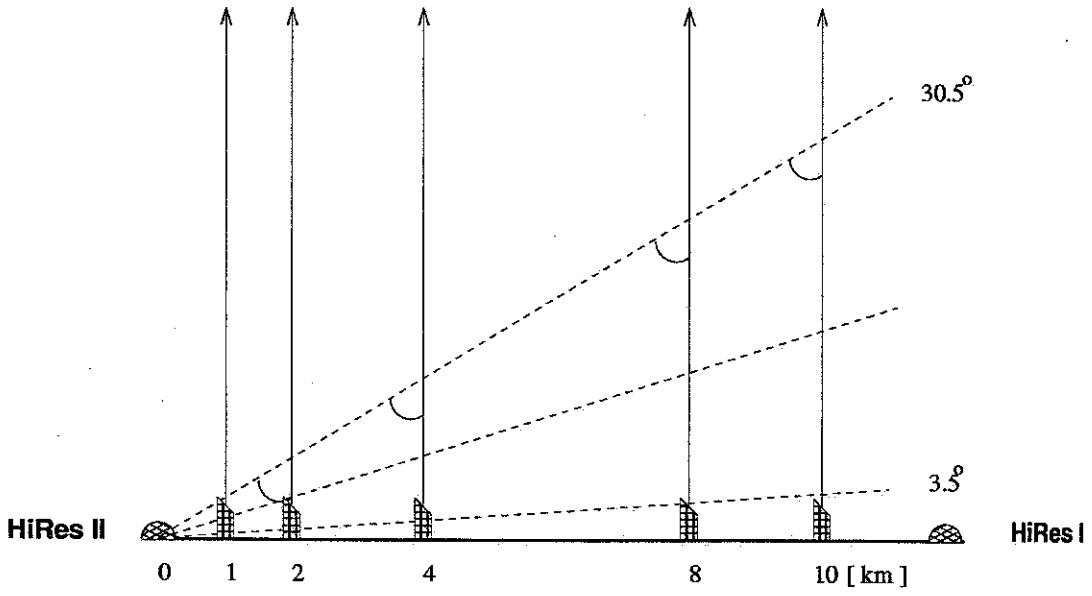

Figure 3.12: The alignment of the flashers

Monitoring Tools

Several methods to monitor the atmosphere have been developed with known light sources such as Xenon flashers and YAG lasers. The atmospheric response to the known light source can be predicted with the aid of the MODTRAN (MODerate resolution TRANsmittance) code [119]. In the simulation, the U.S. standard atmosphere [120] is usually employed along with the 'wind dependent desert aerosol model [121]'. In addition, the flashers and lasers can be used to calibrate our detector by using their known energy and geometry. Unfortunately, some equipment was installed after the HiRes prototype detector was disassembled.

The intersite flasher was located at the center of MIA. It was inclined at an elevation angle of 21°. The flasher fired five times every eight minutes. Since December 1996, twelve vertical Xenon flashers have been located between HiRes-I and HiRes-II [122]. They are located in two rows, 1, 2, 4, 8 and 10 km from the HiRes-II detector. Figure 3.12 shows the sideview of the flashers. For a given angle from the detector, we can measure how much light is attenuated as a function of height from the flashers without knowing the phase function.

The steerable laser system was located at the center of the CASA-MIA site beginning in 1995 [123]. The laser fired 10 ns pulses with energies up to 50 mJ every hour. Unlike the flashers, the laser could point in any direction and could reach further distances. The laser monitored much larger volumes of the atmosphere than the flashers. Two lasers currently operate at the HiRes I and II sites.

Cloud detectors were installed by collaborators from Australia [124]. Using infrared thermopile devices, they provide useful information about clouds. The thermopile devices measure temperature differences between themselves and the sky. The devices monitor the temperature of the night sky, taking advantage of the fact that a clear sky is colder than a cloudy one. The detectors read voltages every minute. This enables us to measure cloud coverage more quantitatively than with the naked eye.

Chapter 4

SIMULATION

To analyze experimental data or to design a detector, it is necessary to know how cascades caused by high energy cosmic rays develop in the atmosphere. The air showers are simulated with the aid of the known physics and models at high energy regions unattainable with accelerators. Consequently, our interpretation of experimental data depends on the models. In the air shower simulation, a large number of particles are produced, and computing time becomes extremely long for higher energy primary particles. To reduce the time, a so-called thinning algorithm is employed.

In addition, one has to simulate the detector response to the air showers. The air shower can be generated by a full shower simulation, but this is time-consuming despite the high level of thinning achieved by the algorithm. Thus, for the detector simulation, showers are generated using parameterizations of the longitudinal and lateral shower development. The detector simulation is used to understand energy and angular resolution, and to determine the aperture of the detector.

4.1 Air Shower Simulation Codes

Versatile packages for simulating air showers over a wide range of primary energies for various primary particles are available. AIRES (AIR shower Extended Simulations) [125] and CORSIKA (COsmic Ray SImulations for KAscade) [79] are the most popular simulation codes for extensive air showers. Several choices are available for the hadronic interaction model at the highest energies. Both codes are written in

FORTRAN.

4.1.1 AIRES and CORSIKA

AIRES is a successor of MOCCA developed by Hillas [126]. In addition to the SIBYLL model [127], the QGSJET model [128] was installed in AIRES for high energy hadronic interactions. However, the current version of AIRES does not include scintillator simulation or generation of Cherenkov light, which are contained in MOCCA. The geomagnetic field is taken into account using the International Geomagnetic Reference Field (IGRF) model [129]. Hillas's splitting algorithm is adopted to simulate electromagnetic and low energy hadronic interactions in AIRES [44]. In this process, computing time is drastically reduced and energy is automatically conserved. Hillas's original splitting algorithm for a nucleon projectile on a target nucleon [44, 130] is as follows:

1. *Split the total energy into two parts at random.*
2. *Assign one part as the energy of the leading nucleon.*
3. *Divide the remaining energy into 2^2 parts.*
4. *Split each of the four pieces of energy into two parts again.*
5. *Assign one part as the energy of a pion.*
6. *Split the other part and assign one piece as the energy of another pion.*
7. *Divide the remaining energy into 2^3 parts.*
8. *Continue this process until the remaining energy is less than the threshold energy.*

In order to reduce computing time, a thinning algorithm [131] was selected within AIRES and CORSIKA: if the total energy of secondary particles from a given interaction falls below a certain fraction of the primary energy, only one of the secondaries is followed, selected at random according to its energy E_i with a probability of $p_i = E_i / \sum_j E_j$. The sum does not include neutrinos or particles with energies below the preset thresholds.

Interactions	AIRES	CORSIKA
EM	Hillas's splitting algorithm	EGS4
Hadronic ($E_{lab} < 80$ GeV)	Hillas's splitting algorithm	GHEISHA ISOBAR
Hadronic ($E_{lab} > 80$ GeV)	QGSJET SIBYLL	QGSJET SIBYLL DPMJET VENUS ($E_{lab} < 2 \cdot 10^{16}$ eV) HDPM ($E_{lab} < 10^{17}$ eV)

Table 4.1: The simulators for electromagnetic and hadronic interactions in AIRES and CORSIKA.

CORSIKA was developed by Dieter Heck and Johannes Knapp et al. for the KASCADE experiment at Karlsruhe in 1990. Within CORSIKA, electromagnetic cascades are simulated with the EGS4 code [132, 133]. Low energy hadronic interactions are simulated with GHEISHA [134] which is also used in the detector simulation code GEANT [135]. At the high energy region, SIBYLL [127], QGSJET [128], DPMJET [136], VENUS [137] and HDPM [138] are available, as shown in Table 4.1. However, CORSIKA does not take into account the curvature of the earth, and the magnetic field of the earth is approximated to be a constant equal to that at the observation site.

Both AIRES and CORSIKA use the same atmospheric model which is parameterized by Linsley for the U.S. standard atmosphere [120]. In his parameterization [139], the atmosphere is divided into five layers. The vertical depth is given as a function of height:

$$X_v(h) = \begin{cases} A_i + B_i e^{-h/C_i} & : \quad h_i < h < h_{i+1}, \quad i = 1,2,3,4 \\ A_i - B_i \frac{h}{C_i} & : \quad h > h_i, \qquad\quad i = 5 \end{cases} \tag{4.1}$$

where h is the height, A_i, B_i, C_i and h_i are given in Table 4.2.

Layer i	h_i (km)	A_i (g/cm^2)	B_i (g/cm^2)	C_i (m)
1	0	-186.5562	1222.6562	9941.8638
2	4	-94.9199	1144.9069	8781.5355
3	10	0.61289	1305.5948	6361.4304
4	40	0.0	540.1778	7721.7016
5	100	0.01128292	1	10^7

Table 4.2: The coefficients of Linsley's parameterization for the U.S. standard atmosphere.

4.1.2 Parameters in the Simulation

In this analysis, CORSIKA is used to simulate extensive air showers. The QGSJET model [128], which is in good agreement with Fly's Eye measurements, is chosen. Within CORSIKA, electromagnetic sub-showers are simulated with the EGS4 code [132, 133]. In order to reduce computing time, a thinning algorithm is selected within CORSIKA and is active below 10^{-5} times primary energy. In our simulations, the threshold energies are 300, 700, 0.1 and 0.1 MeV for hadrons, muons, electrons and photons respectively. Particles below the threshold energies are not followed by the simulation. We chose an observation level 300 m above sea level and simulated showers with a zenith angle of 45° in order to see longer shower tracks.

4.2 Determination of the Primary Energy

One of the goals in a cosmic ray detection experiment is to determine the energy of the incident particles. Unfortunately, the primary energy cannot be measured directly at high energies where the flux is very low. In HiRes, the primary energy has to be reconstructed from the nitrogen fluorescent light caused by the air shower particles. This technique has the advantage that one can measure the number of charged particles in the showers as a function of atmospheric depth.

4.2.1 Calorimetric Energy of an Air Shower

The atmosphere is a calorimeter. The calorimetric energy of an air shower is determined by integrating the longitudinal profile and then correcting for 'unseen' energy. The energy of pure electromagnetic showers was determined by Rossi [95]:

$$E_{em} = \frac{E_c}{X_r}\int_0^\infty N_e(X)dX, \tag{4.2}$$

where X_r is the electron radiation length in air, E_c is the critical energy of an electron in air, and N_e is the number of electrons in the shower. This equation implies that the electromagnetic energy is the total track length of all charged particles multiplied by an energy loss rate $\mathrm{d}E/\mathrm{d}X$ given by E_c/X_r. An important issue is the numerical value of the critical energy E_c, which has been defined separately by Rossi [80] and by Berger and Selter [140]. These authors define critical energy as the energy at which the ionization loss per radiation length is equal to the electron energy or the energy at which energy loss rates for bremsstrahlung and ionization are equal.

We turn to simulations to check the results and avoid this definitional confusion. We simulate ultra high energy showers with realistic fluctuations and realistic distributions of the energies of shower particles. An example is shown in Figure 4.1, where we plot the energy spectra of shower particles at ground level. Particle energies cover a wide range and particles lose energy to ionization at different rates (see inset to figure).

For these simulations we replace Eq. (4.2) with a more general expression for the calorimetric energy,

$$E_{cal} = \alpha\int_0^\infty N_{ch}(X)dX, \tag{4.3}$$

where we integrate over the charged particle longitudinal profile. We replace the constant in Eq. (4.2) with a parameter α representing the mean ionization loss rate over the entire shower. This factor will be approximately equal to E_c/X_r and is

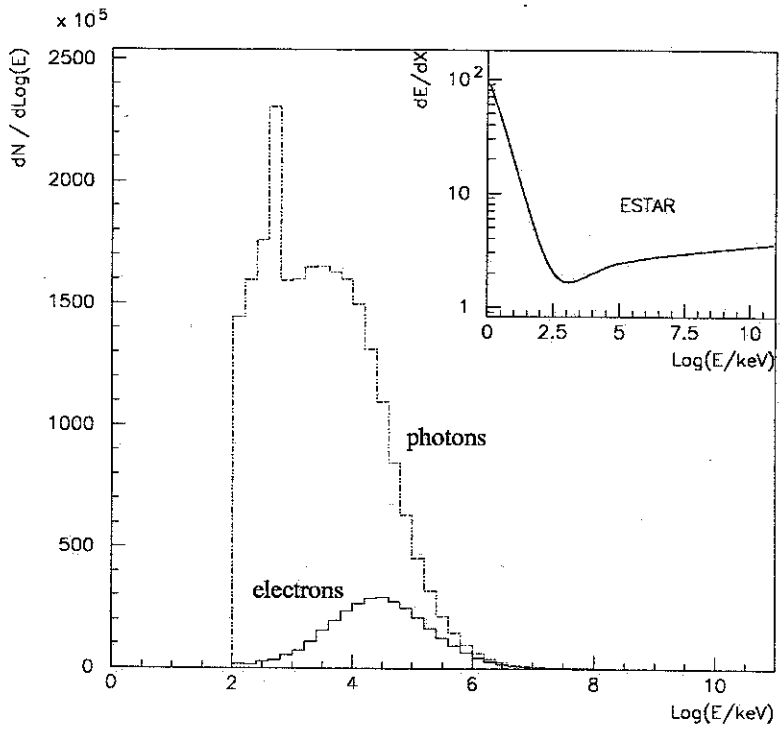

Figure 4.1: The mean energy spectra of photons, electrons and muons at $S = 1$ for 200 proton showers at 10^{17} eV. The spike in the photon spectrum corresponds to electron-positron annihilation. The inset shows the energy loss rate (in MeV/g/cm^2) by ionization of electrons in dry air over the same energy range as the main figure. The ESTAR code produced by the U.S. National Institute of Science and Technology (NIST) was used below 10 GeV [141] and this curve is extrapolated into the region above 10 GeV.

calculated below. Given E_{cal}, we must then make a correction that takes into account the energy carried by high energy muons and neutrinos which ultimately deposit most of their energy in the ground, and the small amount of energy that is lost to nuclear excitation. This 'missing' energy has previously been parameterized by Linsley [142] and by the Fly's Eye group [143].

We also simulate gamma ray induced air showers (which have a very small 'missing energy' component) to check the calorimetric energy method. Finally, we simulate proton and iron induced showers to calculate the 'missing energy' corrections for primary energies up to 10^{20} eV.

4.2.2 Electromagnetic Energy of Showers

Consider a purely electromagnetic shower as shown in Figure 2.1. The primary particle energy E_{em} can be approximated by

$$E_{em} \cong \int_{\epsilon}^{\infty} \triangle E(k) \mathcal{N}_e(k) dk, \tag{4.4}$$

where $\mathcal{N}_e(k)$ is the number of electrons with kinetic energy k and $\triangle E(k)$ is the energy loss by each of these electrons in the calorimeter via ionization. This is an approximation because we have only included particles with kinetic energies above a threshold ϵ. This is consistent with our simulations where we impose a threshold of 0.1 MeV for photons, electrons and positrons. This integral can be carried out by summing over all the electrons produced in the simulation.

We rearrange Eq. (4.4) and include the energy spectrum of particles as a function of atmospheric depth,

$$\mathcal{N}_e(k) = \int_0^{\infty} N_e(X) n_e(k, X) \frac{dX}{\triangle X(k),} \tag{4.5}$$

where $\triangle X(k)$ is the mean free path of electrons as a function of k, $N_e(X)$ is the total number of electrons at depth X, and $n_e(k, X)$ is the normalized electron energy spectrum. Then, the electromagnetic energy is approximated by

$$E_{em} \cong \int_0^\infty N_e(X) \left(\int_\epsilon^\infty \frac{\triangle E}{\triangle X}(k) n_e(k, X) dk \right) dX. \tag{4.6}$$

Typically, the age parameter s is used rather than the depth to describe the stage of development of a shower. The energy spectrum of electrons can then be parameterized in terms of age s. Since the age parameter is really only valid for a pure electromagnetic cascade and since we will use the parameter in reference to hadronic showers, we will refer to our parameter as 'pseudo age' S. We define it as:

$$S(X) = \frac{3 \cdot (X - X_1)}{(X - X_1) + 2 \cdot (X_{max} - X_1)}, \tag{4.7}$$

where X_1 is the depth of the first interaction and X_{max} is the depth at which the shower reaches maximum size. Under this definition, $S(X_1) = 0$, $S(X_{max}) = 1$ and $S(\infty) = 3$.

One can then calculate the mean ionization loss rate ($\mathrm{d}E/\mathrm{d}X$) for the electrons in the shower (with energies $> \epsilon$) at pseudo age S,

$$\alpha(S) = \int_\epsilon^\infty \frac{\triangle E}{\triangle X}(k) \tilde{n}_e(k, S) dk, \tag{4.8}$$

where $\tilde{n}_e$ is the normalized energy spectrum as a function of S. For comparison with Eq. (4.2) we rewrite Eq. (4.6) as:

$$E_{em} \cong < \alpha >_S \int_0^\infty N_e(X) dX, \tag{4.9}$$

where

$$< \alpha >_S = \frac{\sum_i < N_e >_{\triangle S_i} \cdot \alpha(S)_{\triangle S_i}}{\sum_i < N_e >_{\triangle S_i}}, \tag{4.10}$$

and $< N_e >_{\triangle S_i}$ is the average number of electrons within a pseudo age bin $\triangle S_i$.

We have simulated 10^{17} eV showers initiated by photons, protons and iron nuclei in order to calculate the mean energy loss rate over the entire shower, $< \alpha >_S$. We

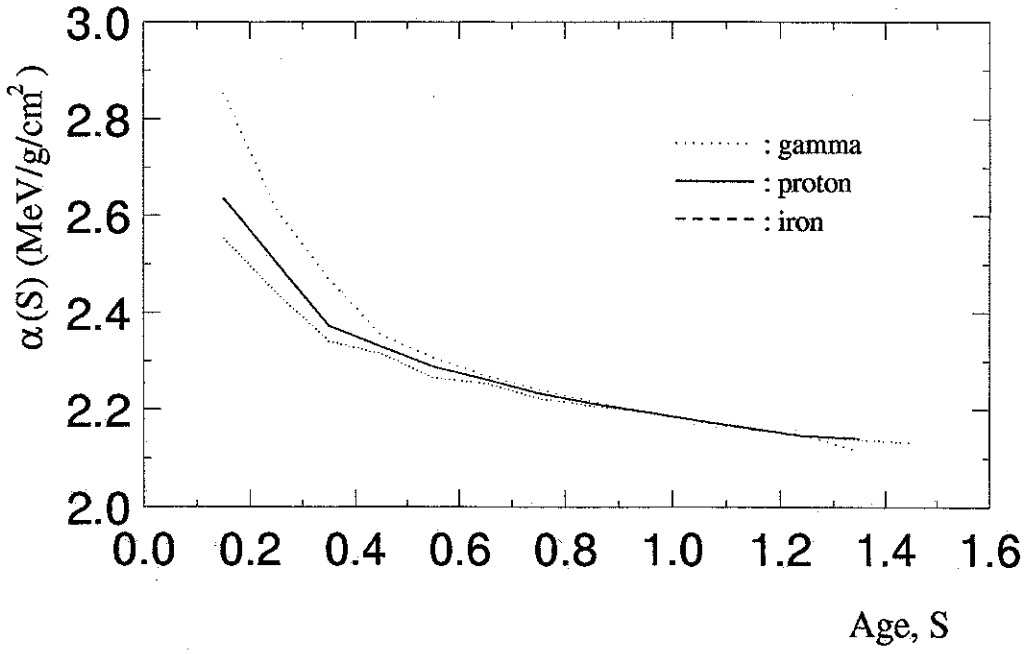

Figure 4.2: The mean ionization loss rate $\mathrm{d}E/\mathrm{d}X$ as a function of S for gamma, proton and iron induced showers at 10^{17} eV.

use bins of $\triangle S_i = 0.1$. Figure 4.2 shows $\alpha(S)$ as a function of age and we find $< \alpha >_S$ is 2.186 ± 0.011, 2.193 ± 0.011 and $2.189 \pm 0.010\,\mathrm{MeV/(g/cm^2)}$ for gamma, proton and iron induced showers respectively.

This compares with the value of the ratio $E_c/X_r = 2.18$ MeV/(g/cm^2) used in the Fly's Eye analysis, where the values were taken to be $E_c = 81$ MeV and $X_r = 37.1$ g/cm^2. This agreement may be a coincidence, since more recent values of the parameters from [80] are $E_c = 86$ MeV (using Rossi's definition) and $X_r = 36.7$ g/cm^2, giving a ratio which is 7 % higher than the typical simulation value of $< \alpha >_S$. However, we note that the simulation results only include the energy loss rates for particles above the 0.1 MeV threshold.

Figure 4.3 shows average shower profiles as a function of age for different primary masses and energies, with the shower size normalized to 1 at $S = 1$. The difference in the average proton-induced shower profile at three different primary energies is smaller than the difference between the proton and iron average profiles at one energy. In other words, the shape of the shower development curve as a function of S is quite

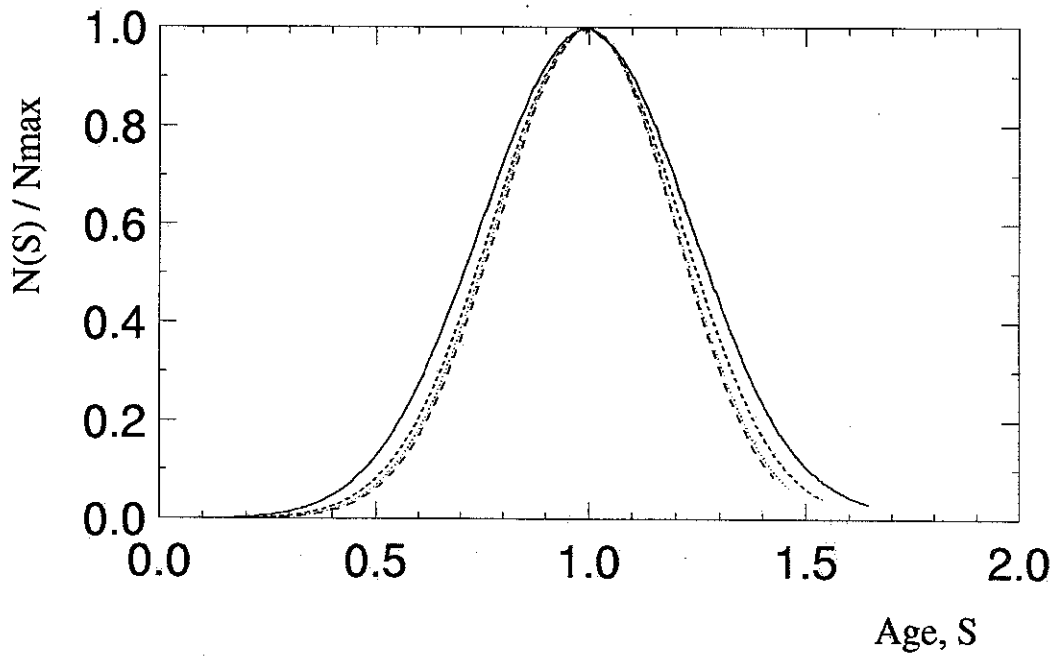

Figure 4.3: The solid line is an average shower profile for 200 iron induced showers at 10^{17} eV. The other three lines are average shower profiles for 200 proton showers at 10^{17} eV (short dashed line), 10^{18} eV (dotted line) and 10^{19} eV (long dashed line).

independent of primary energy or primary mass. It is also well known that the shower particle energy spectrum is a function of S only. Hence, we can assume that our result for $< \alpha >_S$ can be applied over a range of primary masses and energies.

We now apply Eq. (4.3) to some gamma ray induced showers, with $\alpha = 2.19\,\mathrm{MeV}/(\mathrm{g/cm^2})$. The CORSIKA energy thresholds are set as described above with a threshold energy of 0.1 MeV for photons, electrons and positrons. We integrate the shower development curves in two ways for comparison. First, we numerically integrate the CORSIKA output which plots the development curve in 5 g/cm^2 increments. Alternatively, we fit a Gaisser-Hillas function (with variables X_0, X_{max}, N_{max} and λ) to the CORSIKA output and then integrate the function. Both methods give almost identical results.

Table 4.3 shows the results for 500 showers. The calorimetric energy is about 10 % lower than the true value. This is true even when we switch off processes which are not purely electromagnetic, namely $\mu^+\mu^-$ pair production and photo-nuclear reactions,

	Without $\mu^+\mu^-$ & γN		With $\mu^+\mu^-$ & γN		
E_0, eV	E_{cal}/E_0	N_{max}	E_{cal}/E_0	N_{max}	N_μ
10^{16}	0.897 ± 0.003	$(8.45 \pm 0.41)10^6$	0.888 ± 0.004	$(8.32 \pm 0.39)10^6$	$(2.15 \pm 0.80)10^3$
10^{17}	0.898 ± 0.004	$(7.97 \pm 0.39)10^7$	0.888 ± 0.005	$(7.88 \pm 0.34)10^7$	$(2.82 \pm 1.37)10^4$
10^{18}	0.898 ± 0.003	$(7.56 \pm 0.28)10^8$	0.889 ± 0.004	$(7.44 \pm 0.27)10^8$	$(3.19 \pm 0.92)10^5$

Table 4.3: Results of CORSIKA simulations of gamma ray induced air showers at three primary energies. The left-hand half of the table shows results from simulations where photo-nuclear and muon pair production processes have been switched off. The uncertainties shown are root mean squared errors.

E_0, eV	E_{loss}/E_0	$E_e(<0.1$ MeV$)/E_0$	$E_\gamma(<0.1$ MeV$)/E_0$	E_{cal}/E_0
10^{16}	0.888 ± 0.003	0.090 ± 0.001	0.010 ± 0.001	0.888 ± 0.004
10^{17}	0.884 ± 0.005	0.090 ± 0.001	0.012 ± 0.003	0.888 ± 0.005
10^{18}	0.876 ± 0.007	0.092 ± 0.002	0.018 ± 0.005	0.889 ± 0.004

Table 4.4: Results from a study of energy conservation within CORSIKA. Gamma ray induced showers were simulated at three primary energies E_0. E_{loss} refers to the energy lost to the atmosphere through ionization by charged particles with energies above 0.1 MeV. The fraction of the primary energy carried by sub-0.1 MeV electrons and photons is shown in the next two columns. The fraction of primary energy determined by the calorimetric equation (final column) is consistent with E_{loss}/E_0. Again, all uncertainties are RMS.

which have small but important cross-sections in gamma ray initiated showers.

The missing energy is in fact mostly a threshold effect and stems from the energy of particles that drop below the 0.1 MeV threshold. Table 4.4 shows that at 10^{17} eV, 88.4 % of the primary energy is lost to the atmosphere through ionization by particles above 0.1 MeV. Electrons in the shower with energies below 0.1 MeV carry 9.0 % of the primary energy, while sub-0.1 MeV photons carry 1.2 % of the primary energy. The calorimetric energy derived by Eq. (4.3) is 88.8 % of the primary energy, a good match to the ionization energy loss by particles above 0.1 MeV.

We assume that the sub-0.1 MeV particles will eventually lose energy to ionization. The nitrogen fluorescence efficiency is proportional to the ionization loss rate, so experiments like HiRes will detect light in proportion to the energy loss, even for very low energy particles. So for further CORSIKA studies described below we have added 10 % of the primary energy to the integrated energy loss result (from Eq. (4.3))

to account for the sub-0.1 MeV particles that do not appear in the CORSIKA output.

4.2.3 Missing Energy

We have described the calorimetric energy estimation for gamma ray induced showers. Next, we consider hadronic showers, where we expect the calorimetric energy to fall short of the primary energy because of the so-called 'missing energy' - the energy channeled into neutrinos, high energy muons and nuclear excitation. Much of this energy is deposited into the ground and is not visible in the atmospheric calorimeter. The first estimate of missing energy was obtained by Linsley [142], who made measurements of the number of electrons and muons at ground level and assessed the energy content of these components. The Fly's Eye group parameterized Linsley's estimates [143] as:

$$E_{cal}/E_0 = 0.990 - 0.0782 \cdot E_0^{-0.175}, \tag{4.11}$$

where E_0 is the primary energy and E_{cal} is the calorimetric energy derived from Eq. (4.3), both in units of 10^{18} eV. This parameterization was said to be valid for $10^{15}\,\text{eV} < E_0 < 10^{20}\,\text{eV}$.

We have simulated proton and iron initiated showers at eight primary energies from 3×10^{16} eV to 10^{20} eV using CORSIKA. We apply Eq. (4.3) with a mean energy loss rate of 2.19 MeV/(g/cm^2) by fitting a Gaisser-Hillas profile to the CORSIKA development curve and then integrating the function. We then add 10% of the primary energy to this result to take into account the CORSIKA threshold effect. Finally, we compare this calorimetric energy with the primary energy, as shown in Figure 4.4. For comparison purposes, we also show Linsley's results. The solid line in Figure 4.4 shows the average behavior for proton and iron showers, which we express here as a function of E_{cal} (for practical convenience) in units of 10^{18} eV,

$$E_{cal}/E_0 = (0.959 \pm 0.003) - (0.082 \pm 0.003) \cdot E_{cal}^{-(0.150 \pm 0.006)}, \tag{4.12}$$

which is valid for $3 \times 10^{16}\,\text{eV} < E_0 < 10^{20}\,\text{eV}$.

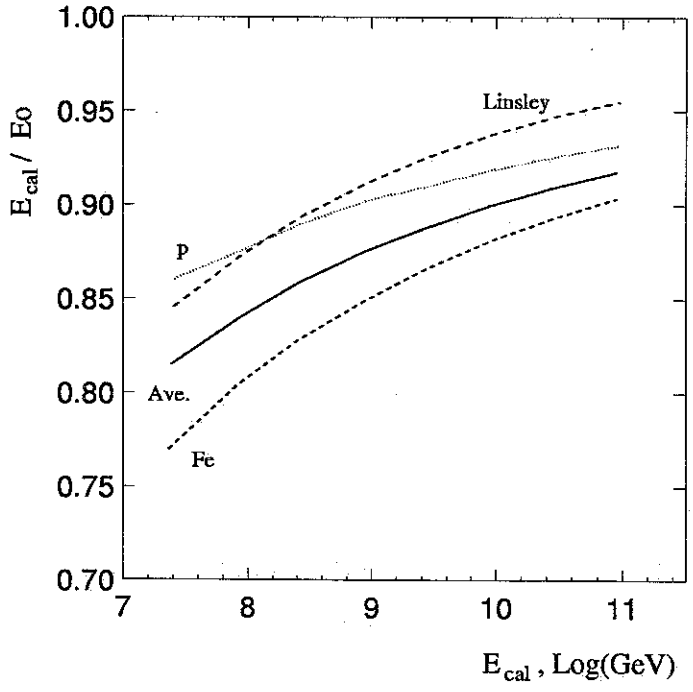

Figure 4.4: The functions for correcting the calorimetric energy to the primary energy, as a function of calorimetric energy. Shown are the corrections for proton showers (dotted line) and iron showers (short dashed line) and an average of the two (solid line). For comparison, Linsley's function is also shown.

The analysis shows that different corrections have to be applied to proton, gamma and iron showers. Unfortunately, in the analysis of air showers, it is not possible to determine shower type on an event-by-event basis: if we apply this average energy correction to a shower, we make an error of about 5 % in the energy estimation. If the primary particle is a gamma ray, this assumption will overestimate the energy by up to 20 %. Of course, if the shower development profile is obviously anomalous (as expected for gamma ray showers above 10^{19} eV due to the LPM effect), gamma-ray primaries can be recognized and this systematic error can be avoided. The parameterizations for proton and iron showers are

$$E_{cal}/E_0 = (0.964 \pm 0.003) - (0.062 \pm 0.004) \cdot E_{cal}^{-(0.143 \pm 0.009)}, \qquad (4.13)$$

and

$$E_{cal}/E_0 = (0.954 \pm 0.002) - (0.102 \pm 0.002) \cdot E_{cal}^{-(0.156 \pm 0.003)}, \qquad (4.14)$$

respectively.

In an experiment like HiRes, atmospheric nitrogen fluorescence provides a measurement of ionization energy deposition, since the yield of fluorescent photons is proportional to this energy deposition [144]. In the reconstruction process, we convert the amount of light emitted by the shower at a particular depth to a number of charged particles, assuming that these charged particles are ionizing at the mean ionization rate. We then perform the path length integral (Eq. (4.3)), multiply the result by the mean ionization loss rate of 2.19 MeV/(g/cm^2), and then make a correction for missing energy (Eq. (4.12)).

4.3 Longitudinal Shower Development

Fluorescent light detectors like HiRes observe the longitudinal shower profile caused by cosmic ray particles, that is, they measure the number of charged particles as a function of depth. It is important to note, however, that often only a part of the

shower profile is observed, because the detector may not cover the entire night sky or because the air shower stops developing when it reaches the ground. In general, it is very difficult to reconstruct showers for which X_{max} is outside the field of view of the detector. Thus, we need to extend the shower profile at both ends. Therefore, we need a general shower profile function to reconstruct the air shower and subsequently determine the shower energy by integrating this shower profile function [145].

For this purpose, the so-called Gaisser-Hillas function [98] has been widely used. In this section, we study the characteristics of the parameters in the Gaisser-Hillas function with simulated air showers. Two of the parameters turn out to be correlated, so finding an alternative to the Gaisser-Hillas function with fewer parameters is desirable. Given that the shower profile is very symmetric in terms of age (Figure 4.3), we try a Gaussian function in shower age s as an alternative shower profile function. The advantage of using a Gaussian function rather than the Gaisser-Hillas function is not only that the number of fitting parameters is reduced. In addition, the function is independent of the starting point of the shower profile, X_0, a parameter of the Gaisser-Hillas function which can not be obtained by experiment. Figure 4.5 shows the average shower profile from data along with the Gaisser-Hillas and Gaussian function. According to this figure, light produced at the early stage of shower development rarely reaches the detector. In the end, we compare the fitting qualities of both functions.

4.3.1 Gaisser-Hillas Function

The Gaisser-Hillas function is given by

$$N(X) = N_{max}\left(\frac{X - X_0}{X_{max} - X_0}\right)^{\frac{X_{max}-X_0}{\lambda}} e^{-(X-X_{max})/\lambda}, \tag{4.15}$$

where X_0 is interpreted as the first interaction depth; but in fact, X_0 is a physically meaningless parameter and has mostly negative values. To show this, we define X_1 as the first interaction depth to distinguish it from X_0. Under this definition, we have $N(X_0) = 0$ and $N(X_1) = 1$. The correlation between X_1 and X_0 was already shown

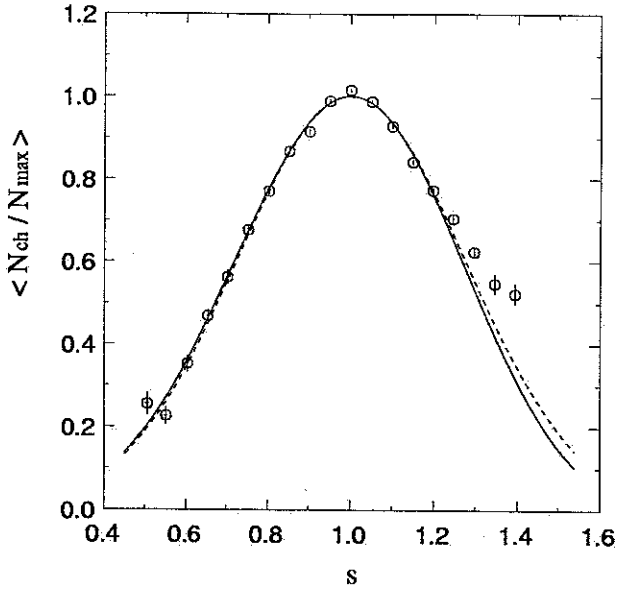

Figure 4.5: The average shower profile is shown in terms of the age parameter along with the Gaisser-Hillas function (solid line) and the Gaussian function (dashed line). The open circles refer to the MIA-HiRes prototype data taken from [146].

in Figure 4.6. The average X_0 for different primaries is shown in Table 4.5.

The maximum number of shower particles, N_{max}, is found to be correlated with λ as shown in Figure 4.7 (a). As mentioned previously, the area under the longitudinal shower profile is proportional to primary energy. Thus, we can infer that N_{max} is inversely proportional to the width of the profile. Figure 4.7 (b) shows the correlation between N_{max} and the width of the shower profile. λ has been known as the proton interaction length which was set to 70 g/cm^2. According to our study, λ is not the proton interaction length and depends on primary energy and mass. In summary, Table 4.5 shows the first interaction depth, the width of the profile and four parameters of the Gaisser-Hillas function with various primary energies and masses. According to the table, the width of the profile fluctuates much less than X_{max}, because the first interaction depth also contributes to the fluctuation of X_{max}. The fluctuation of width decreases with primary energy except for gamma induced showers.

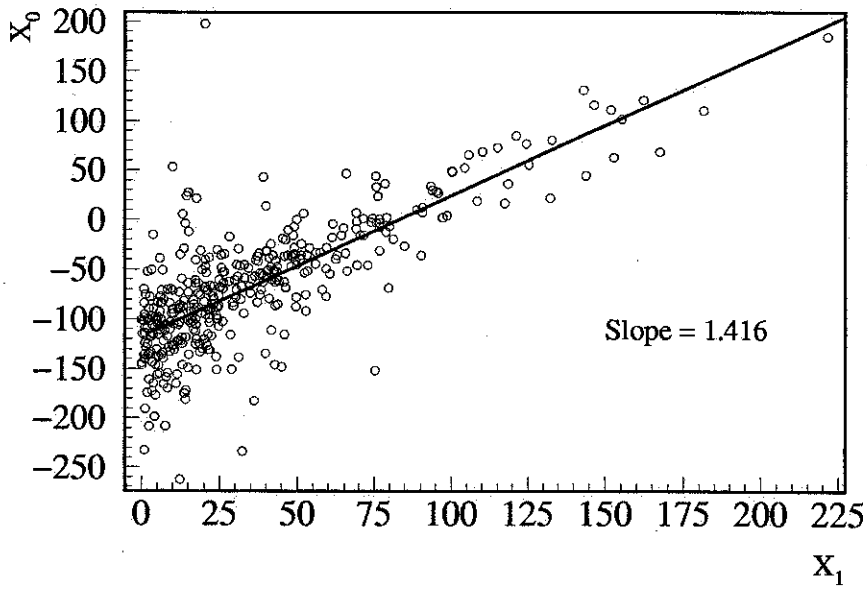

Figure 4.6: The correlation between X_0 and X_1 for 400 proton induced showers at 10^{18} eV. The QGSJET model [128] in CORSIKA was used to generate events.

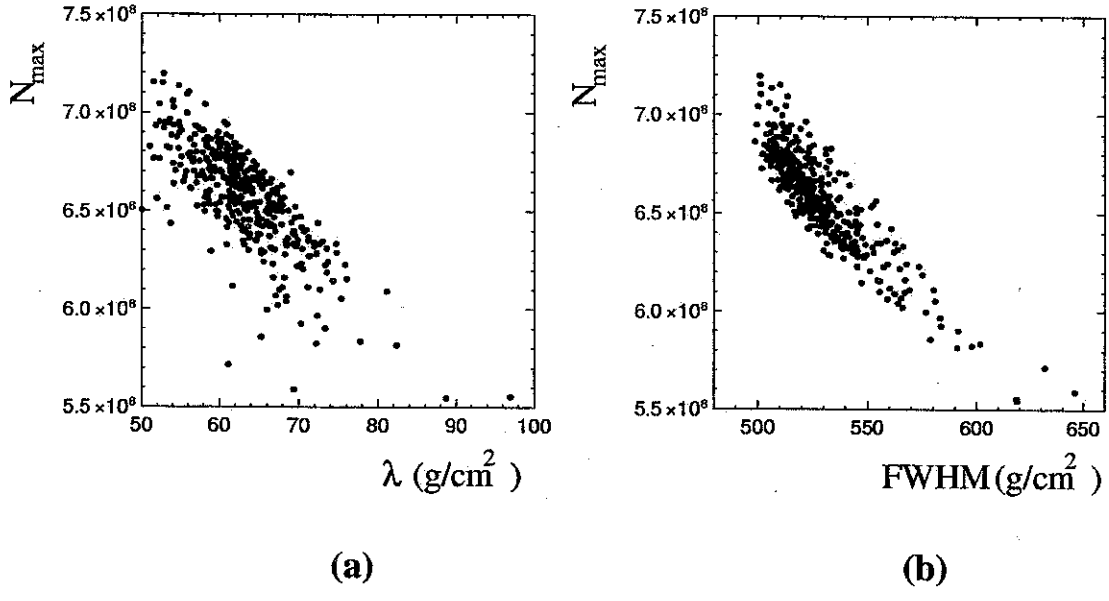

Figure 4.7: (a) shows the correlation between N_{max} and λ and (b) shows the correlation between N_{max} and the width of the profile (FWHM).

	$Log(E)$	X_1	X_0	N_{max}	X_{max}	λ	FWHM
p	17.0	52.8 ± 54.9	-33.3 ± 69.5	$(6.60 \pm 0.35)10^7$	672 ± 77.2	67.1 ± 9.2	512 ± 26
	18.0	49.3 ± 49.5	-68.0 ± 64.1	$(6.58 \pm 0.26)10^8$	731 ± 66	63.1 ± 5.7	529 ± 21
	19.0	46.5 ± 44.8	-86.1 ± 55.2	$(6.46 \pm 0.22)10^9$	782 ± 68	62.4 ± 4.8	548 ± 21
Fe	17.0	12.8 ± 12.5	-30.1 ± 20.0	$(5.97 \pm 0.15)10^7$	574 ± 19	79.1 ± 4.5	517 ± 12
	18.0	10.3 ± 10.4	-59.7 ± 17.7	$(6.18 \pm 0.13)10^8$	632 ± 17	72.2 ± 3.4	528 ± 10
	19.0	10.5 ± 9.83	-89.1 ± 12.4	$(6.29 \pm 0.11)10^9$	692 ± 15	66.6 ± 2.0	539 ± 7
γ	17.0	46.9 ± 43.3	-74.2 ± 64.3	$(7.87 \pm 0.32)10^7$	764 ± 49	50.1 ± 4.6	483 ± 19
	18.0	49.8 ± 47.9	-50.3 ± 66.7	$(7.46 \pm 0.31)10^8$	852 ± 54	52.0 ± 5.4	510 ± 24
	19.0	50.8 ± 50.2	-32.4 ± 69.0	$(6.97 \pm 0.33)10^9$	958 ± 67	54.7 ± 6.1	548 ± 32

Table 4.5: First interaction depth, the width of shower profile and four parameters of the Gaisser-Hillas function for p, Fe and γ induced showers.

4.3.2 Gaussian Function in Age Parameter

The age parameter has been used to describe the energy spectra and lateral distribution of shower particles. Figure 4.8 shows the shower profiles in age. A Gaussian function in age s is given by

$$f(s) = \exp\left\{\frac{1}{2\sigma^2}(s-1)^2\right\}. \tag{4.16}$$

Substituting the definition of age (Eq. (2.20)) into Eq. (4.16) gives

$$F(X) = \exp\left\{\frac{2}{\sigma^2}\left(\frac{X - X_{max}}{X + 2X_{max}}\right)^2\right\}. \tag{4.17}$$

Several examples of profile fits are shown in Figure 4.9. To determine χ^2 of the profile fit, it is necessary to know the error of the weighted shower profile due to the thinning algorithm. For a weighted air shower, the total number of charged particles at a given depth is determined by summing up all weights:

$$N_{ch} = \sum_{i=1}^{N_o} w_i = \bar{w} \cdot N_o, \tag{4.18}$$

where N_o is the unweighted number of particles and w_i is the weight of each particle. From the above equation, we have

$$\frac{\delta N_{ch}}{N_{ch}} = \sqrt{\left(\frac{\delta \bar{w}}{\bar{w}}\right)^2 + \left(\frac{\delta N_o}{N_o}\right)^2}. \tag{4.19}$$

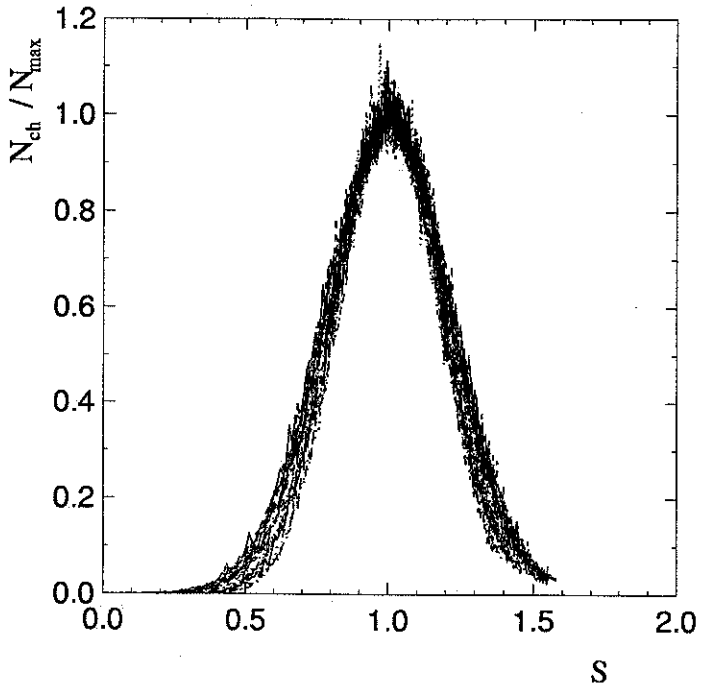

Figure 4.8: The shower profiles in age for proton induced showers at 10^{18} eV.

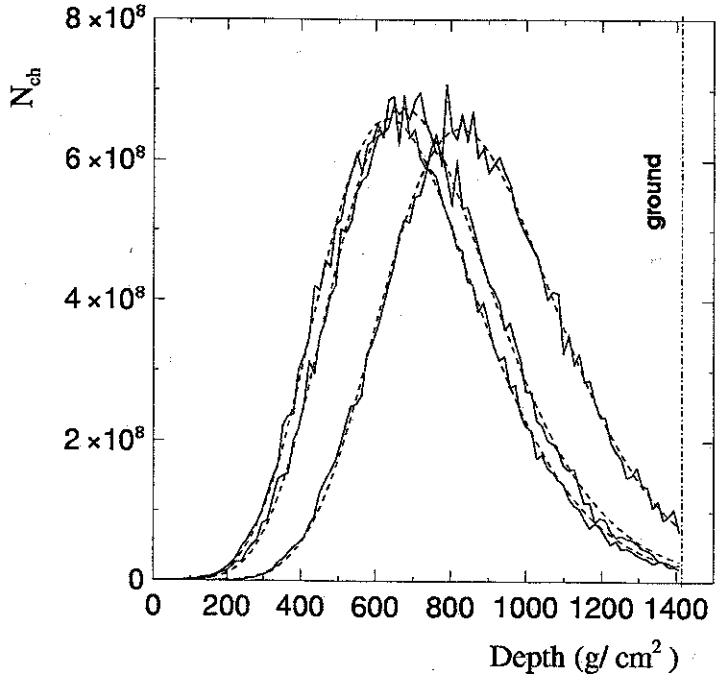

Figure 4.9: A few examples of shower profile fits with a Gaussian function (Eq. (4.17)) for proton induced showers at 10^{18} eV.

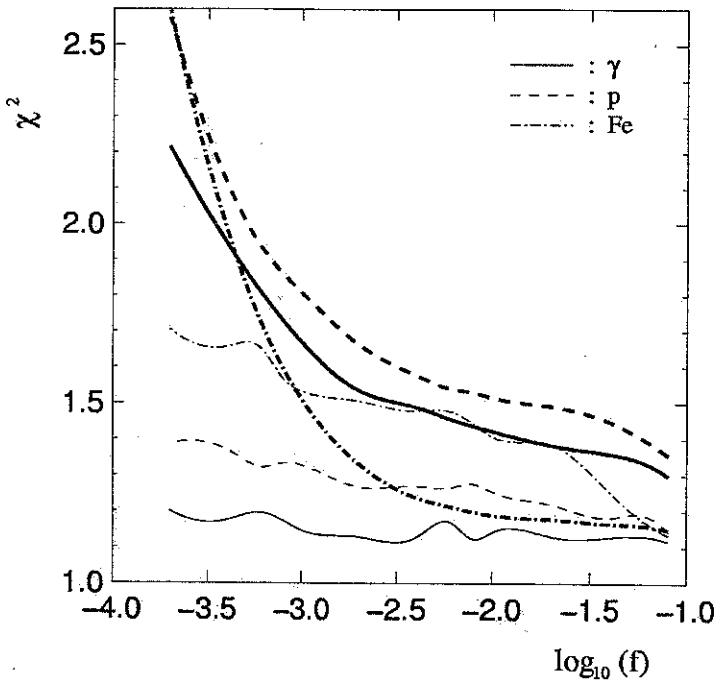

Figure 4.10: χ^2 as a function of f. Thick lines are for a Gaussian function in age, while thin lines are for the Gaisser-Hillas function.

Using $\delta\bar{w} = \sigma(w)/\sqrt{N_o}$ and $\delta N_o = \sqrt{N_o}$, we obtain

$$\delta N_{ch} = N_{ch}\sqrt{\frac{1}{N_o}\left\{\left(\frac{\sigma(w)}{\bar{w}}\right)^2 + 1\right\}}. \tag{4.20}$$

Finally, we define χ^2 as follows:

$$\chi^2 = \sum_{i=1}^{N} \frac{(F(x_i) - N_{ch}^i)^2}{(\delta N_{ch}^i)^2}, \tag{4.21}$$

where

$$\delta N_{ch}^i = \sqrt{N_o^i \cdot \bar{w}_i^2}. \tag{4.22}$$

However, when we do a fit with a Gaussian function in age, χ^2 is large. It turns out that the Gaussian function cannot fit the profile at the early stage of shower development. Thus, we should set a limit for the Gaussian function. To do so, we introduce a parameter f, where the fitting is limited to $N_{ch} \geq f \cdot N_{max}$. Figure 4.10 shows χ^2 as a function of f. The χ^2 of the Gaussian function increases quickly below

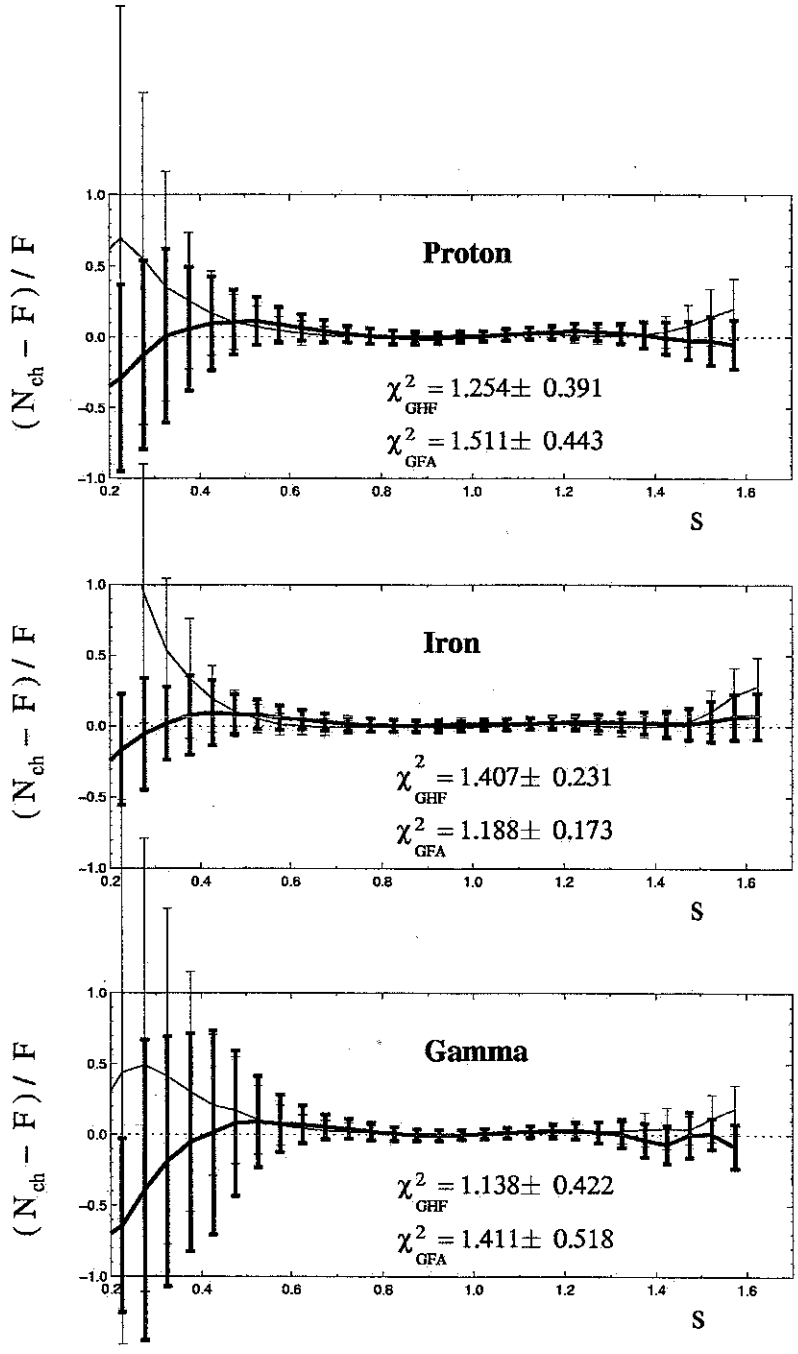

Figure 4.11: The residuals for gamma, proton and iron initiated showers are shown. The thick line is for a Gaussian function in age (GFA) and the thin line is for the Gaisser-Hillas function (GHF).

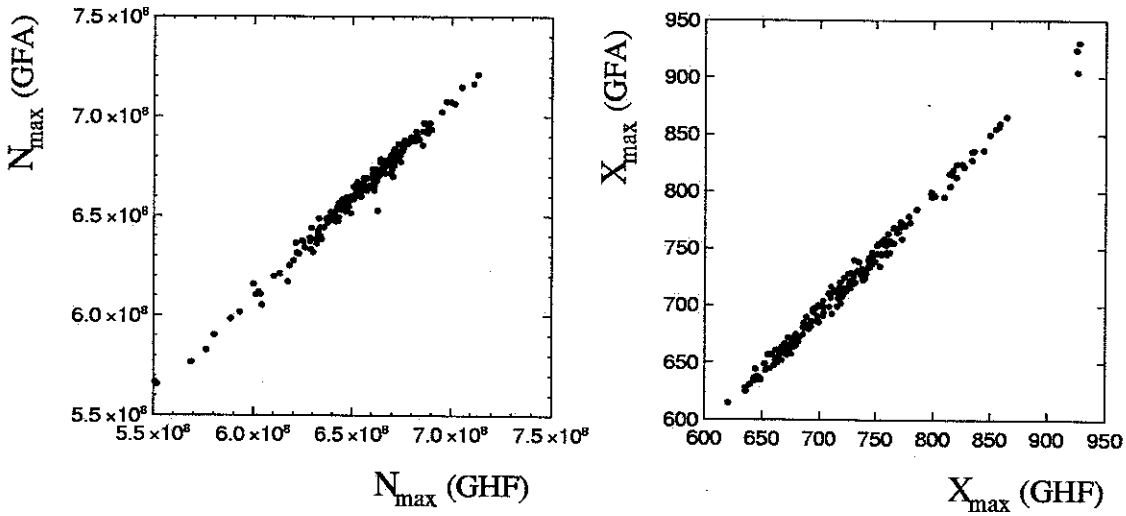

Figure 4.12: Comparison of X_{max} and N_{max} from fitting with the Gaisser-Hillas function (GHF) and a Gaussian function in age (GFA).

$Log(E)$	p	Fe	γ
17.0	0.210 ± 0.019	0.241 ± 0.008	0.176 ± 0.011
18.0	0.200 ± 0.015	0.227 ± 0.005	0.167 ± 0.011
19.0	0.196 ± 0.013	0.214 ± 0.004	0.159 ± 0.011

Table 4.6: σ of Gaussian in age for p, Fe and γ induced showers at three different energies.

$f = 0.01$, while that of the Gaisser-Hillas function increases very slowly. The residual is shown in Figure 4.11, and χ^2 with $f = 0.01$ is indicated on each graph. $f = 0.01$ corresponds to $s \approx 0.4$. According to Figure 4.5, the detector observes the shower profile within $0.5 < s < 1.4$. Therefore, a Gaussian function is expected to work well with the real shower profiles. We can also use an even larger f to determine N_{max} and X_{max}. Then, primary energy can be determined by integrating either functional form. For example, integrating the profiles initiated by protons at 10^{18} eV gives $(3.660 \pm 0.063) \cdot 10^{11}$ g/cm^2 for the Gaisser-Hillas function and $(3.673 \pm 0.065) \cdot 10^{11}$ g/cm^2 for a Gaussian function for 200 events. The difference is less than 1 %. Figure 4.12 shows the comparison of N_{max} and X_{max} determined by fitting with two different functions. Note that according to Table 4.6, σ changes slowly with energy, and is different for electromagnetic showers then for hadronic showers.

4.4 Detector Simulation

The simulation of the extensive air showers is only a part of the full simulation. Once air showers are simulated, we need to simulate the detector response to the air showers. HiRes is a detector that collects light produced by shower particles. The detector simulation consists of three parts - generation of air showers, production and propagation of light emitted at the shower track in the atmosphere, and the detector response to the light. To save computing time for full air shower simulations, the air showers are generated by a parameterization of the shower development in the simulation. Once we know how the detector responds to the light emitted by shower particles caused by the cosmic ray particle with a given energy, mass and arrival direction in the simulation, we can determine the detector aperture and the resolution of energy, X_{max} and arrival direction for the given primary particle.

4.4.1 Shower Generation

The generation of air showers with reasonably high thinning threshold energy is time-consuming. Alternatively, shower profile libraries can be built for different primaries

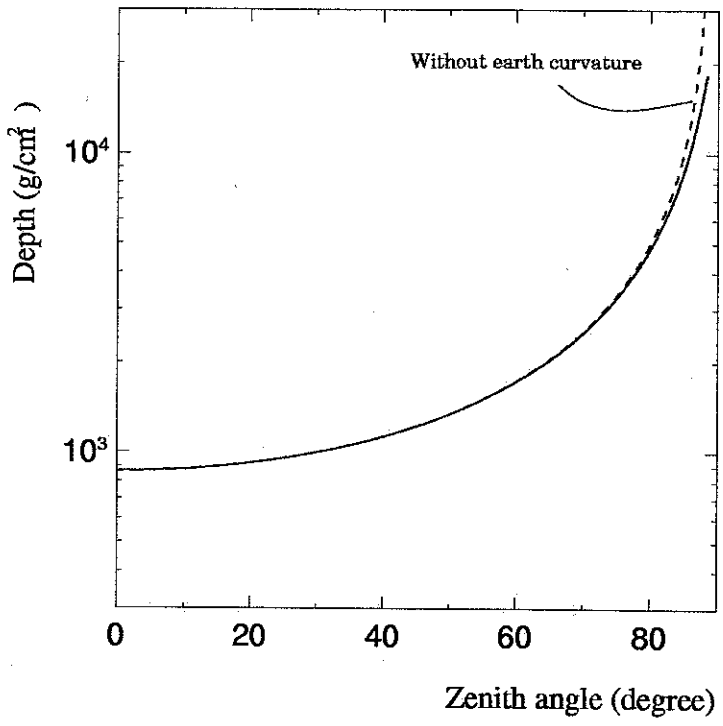

Figure 4.13: The atmospheric depth of Dugway, Utah, as a function of zenith angle for flat and curved earth.

at several fixed energies. The detector response to the showers from the libraries can be simulated. However, the number of such simulated events is limited. To overcome this limitation and to save computing time for air shower simulation, air showers are generated from a parameterization of the shower development. The parameterization has been done for proton and iron showers from $10^{16.5}$ to 10^{20} eV.

To generate a more realistic shower profile, we turn to air shower simulations. We used the shower profiles generated with the CORSIKA code. To see longer tracks, we generate air showers with a large zenith angle. Unfortunately, CORSIKA does not take into account the curvature of the earth. Figure 4.13 shows depth as a function of zenith angle for flat and curved earth. The difference is very small at zenith angles of less than about 60°. Thus, a zenith angle of 45° was chosen for the the simulation. The observation height is 300 m above sea level. The Gaisser-Hillas function is used to fit the shower profiles.

From the simulation study, we know that the first interaction depth (X_1) of the primary particle is correlated with X_0, as mentioned in the previous section. X_0 is generated from the first interaction depth. First, X_1 is generated randomly from an exponential function $\exp(-x/\lambda_0)$, where λ_0 is the mean free path of the primary particles. By using the correlation between X_0 and X_1, X_0 is generated by

$$X_0 = p \cdot X_1 + q, \tag{4.23}$$

where p and q are given in Table 4.7 and 4.8 for proton and iron induced showers, respectively. As mentioned in Chapter 2, the gamma probability density function is used to fit the X_{max} distribution:

$$X_m(x) = \frac{1}{l\Gamma(n-1)}\left(\frac{x - X_c}{l}\right)^n \cdot \exp[(X_c - x)/l], \tag{4.24}$$

where n, l and X_c are given in Table 4.7 and 4.8. The distributions of X_{max} generated from the parameterization and a full CORSIKA simulation are compared for proton and iron induced showers as shown in Figure 4.14.

When parameterizing the maximum shower size, we should be very careful. In the air shower simulation, low energy particles below the threshold energies were not taken into account in the shower size. Thus, we have to account for the low energy particles in the shower profile. However, we do not know how many particles were dropped below the threshold energies. Considering the fact that the calorimetric energy is determined by integrating the shower profile, the missing 10 % of the energy due to the threshold effect should increase the shower size by 10 % of the actual size. If N_{max}^{th} is the maximum shower size counting particles above the threshold, the actual shower size is

$$N_{max} = N_{max}^{th} + 0.1\ N_{max}. \tag{4.25}$$

Therefore, the shower maximum size is raised by 11.11 (10/9) %. We fitted N_{max} and λ distributions with a Gaussian. The mean and sigma are given in Table 4.7

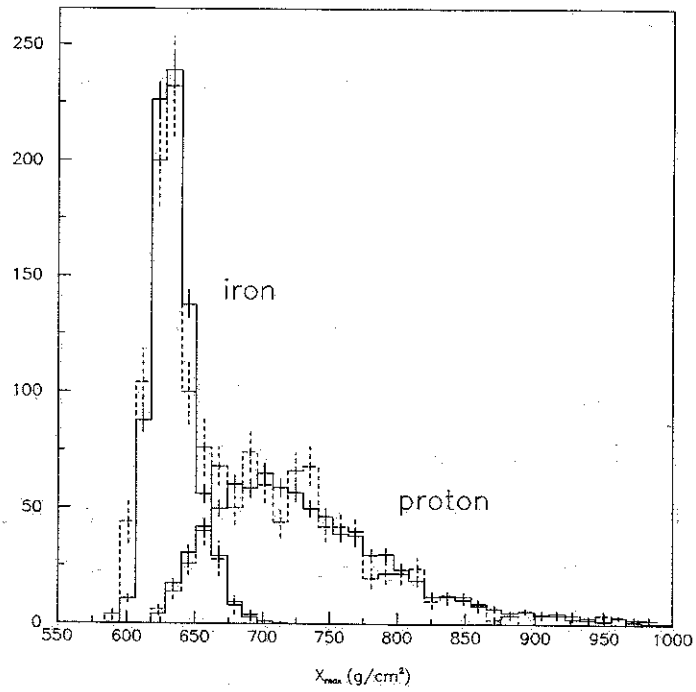

Figure 4.14: The X_{max} distributions from the parameterization (solid line) as compared to a full CORSIKA simulation (dashed line) for proton and iron induced showers at 10^{18} eV.

and Table 4.8. Considering the correlation between N_{max} and λ, both parameters are generated with random numbers (R_1, R_2):

$$N_{max} = \mu_1 + \sigma_1 \cdot R_1, \tag{4.26}$$

and

$$\lambda = r + \mu_2\ \sigma_2\ R_1 + \sqrt{1-\sigma_2^2} \cdot \mu_2\ R_2, \tag{4.27}$$

where μ_1 and μ_2 are mean, σ_1 and σ_2 are sigma for N_{max} and λ respectively, and r is the correlation coefficient. Figure 4.15 shows the comparison between the CORSIKA output and the parameterization of λ and N_{max}. All coefficients in the parameterization are shown in Table 4.7 and 4.8 for proton and iron, respectively. Figure 4.16 and 4.17 show the four parameters of the Gaisser-Hillas function as a function of the primary energy. The parameterization has been done at every half decade and is interpolated between the fixed energies. Figure 4.18 shows the ratio of reconstructed energy to input energy for proton and iron induced showers. 3,000 events were generated at fixed energies and the energy was analytically calculated. Combining Eq. (4.3) and the Gaisser-Hillas function gives

$$E_{cal} = \alpha N_{max} \lambda \Gamma\left(\frac{X_{max} - X_0}{\lambda + 1}\right)\left(\frac{e\lambda}{X_{max}}\right)^{(X_{max}-X_0)/\lambda}. \tag{4.28}$$

To convert to the primary energy, Eq. (4.13) and Eq. (4.14) are used for proton and iron showers, respectively. Figure 4.18 shows that the reconstructed energies without going through the detector are consistent with the input values.

Once a shower profile is generated, the core location is chosen at random within a pre-defined area. The incident direction is determined from a uniform distribution in $\cos(\theta)$ and ϕ.

4.4.2 Light Production and Propagation

Once an air shower is generated, we calculate the number of charged particles at the center of each segment subtending 0.04° seen from the detector as shown in Figure

$\log(E_0)$, eV		16.5	17.0	17.5	18.0	18.5	19.0	19.5	20.0
N_{max} ($\times 10^7$)	μ_1	1.980	6.693	19.90	65.99	196.3	650.4	1933.	6294.
	σ_1	0.113	0.299	0.759	2.18	4.80	13.0	38.0	143.4
λ (g/cm^2)	μ_2	67.69	65.81	63.62	62.87	62.46	62.10	62.99	64.10
	σ_2	7.225	5.966	5.652	5.169	4.063	3.887	2.726	3.305
r		-0.767	-0.759	-0.747	-0.756	-0.659	-0.597	-0.715	-0.693
X_0 (g/cm^2)	λ_0	52.85	47.61	46.31	48.46	42.77	45.27	41.97	34.35
	p	0.937	0.954	0.946	1.002	1.076	1.018	1.011	1.046
	q	-72.48	-83.83	-97.75	-117.3	-127.1	-133.4	-132.1	-131.1
X_{max} (g/cm^2)	n	1.111	1.429	1.434	1.210	0.338	1.102	0.517	0.844
	l	31.32	28.26	25.88	33.09	47.18	33.57	41.21	38.39
	X_c	525.6	548.8	583.3	613.8	650.8	667.0	694.0	716.3

Table 4.7: Coefficients of the parameterization with the Gaisser-Hillas function for proton showers without correcting for the threshold effect.

$\log(E_0)$, eV		16.5	17.0	17.5	18.0	18.5	19.0	19.5	20.0
N_{max} ($\times 10^7$)	μ_1	1.735	5.958	18.27	61.76	187.2	630.3	1889.	6271.
	σ_1	0.0635	0.193	0.633	1.90	4.89	11.5	32.5	97.1
λ (g/cm^2)	μ_2	83.27	78.93	75.08	71.56	69.07	66.40	65.34	64.66
	σ_2	5.152	6.079	5.041	4.581	3.307	2.939	2.074	1.493
r		-0.744	-0.756	-0.691	-0.732	-0.722	-0.687	-0.715	-0.661
X_0 (g/cm^2)	λ_0	10.42	11.74	11.51	9.526	10.45	9.344	10.87	9.728
	p	0.888	0.876	1.005	0.859	0.962	0.832	0.934	0.960
	q	-27.83	-41.32	-54.86	-68.54	-85.53	-97.89	-107.9	-114.5
X_{max} (g/cm^2)	n	10.58	10.32	15.28	19.14	7.427	13.98	14.07	9.605
	l	5.384	4.649	4.182	2.709	3.341	2.871	2.753	3.075
	X_c	466.1	510.1	525.8	569.5	624.0	640.4	668.3	704.2

Table 4.8: Coefficients of the parameterization with the Gaisser-Hillas function for iron showers without correcting for the threshold effect.

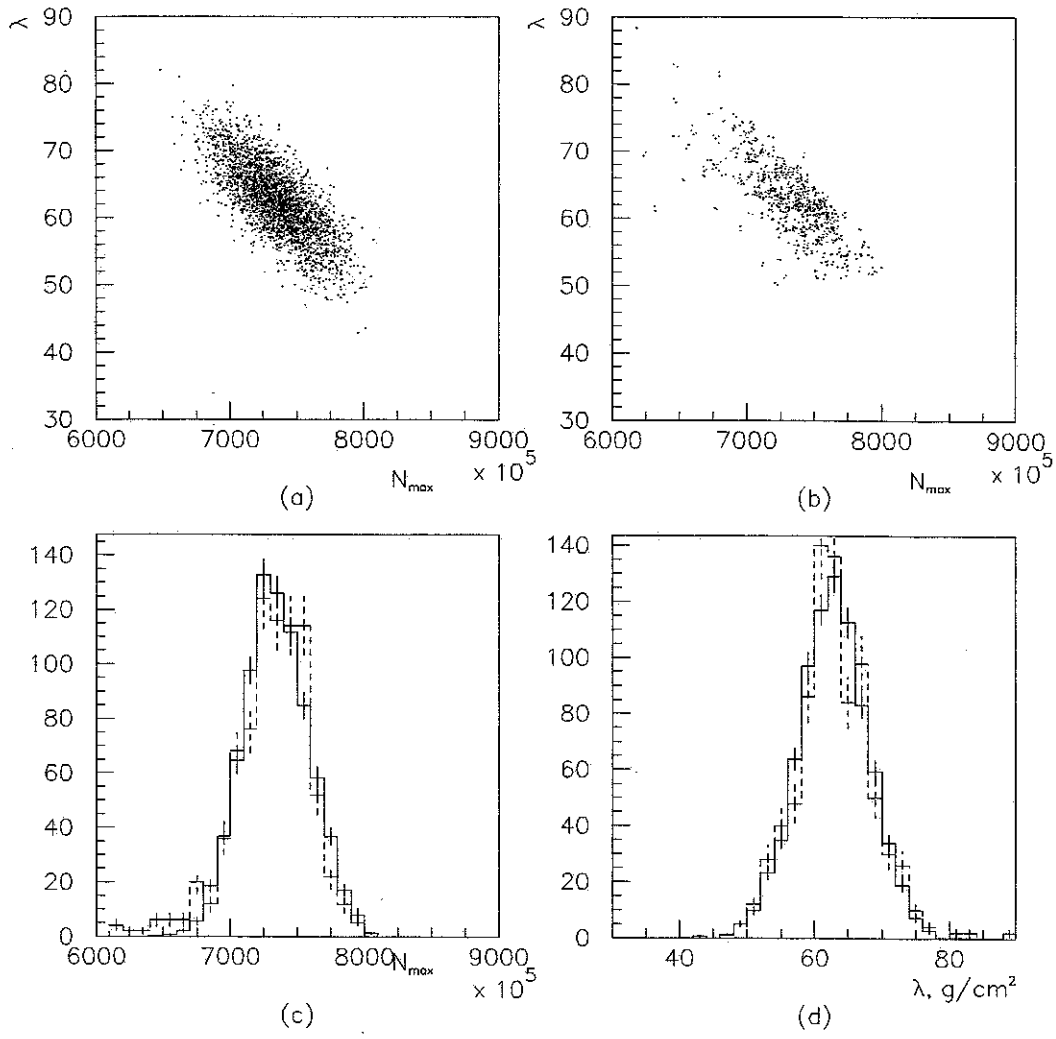

Figure 4.15: The distributions of the parameterized (solid line) N_{max} and λ are compared with those of CORSIKA output (dashed line) for proton induced shower at 10^{18} eV. The correlation between the two parameters are also compared.

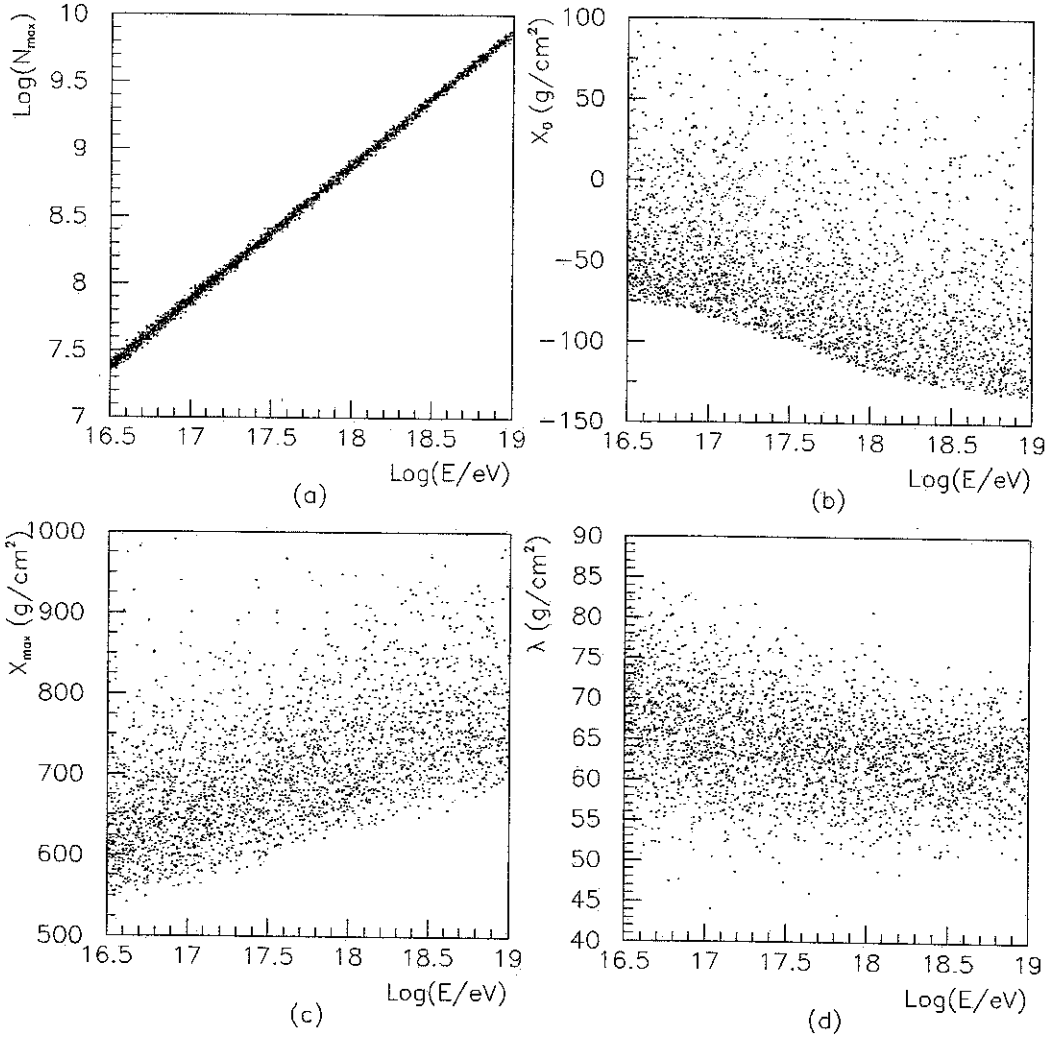

Figure 4.16: The four parameters of the Gaisser-Hillas function as a function of the primary energy for proton induced showers.

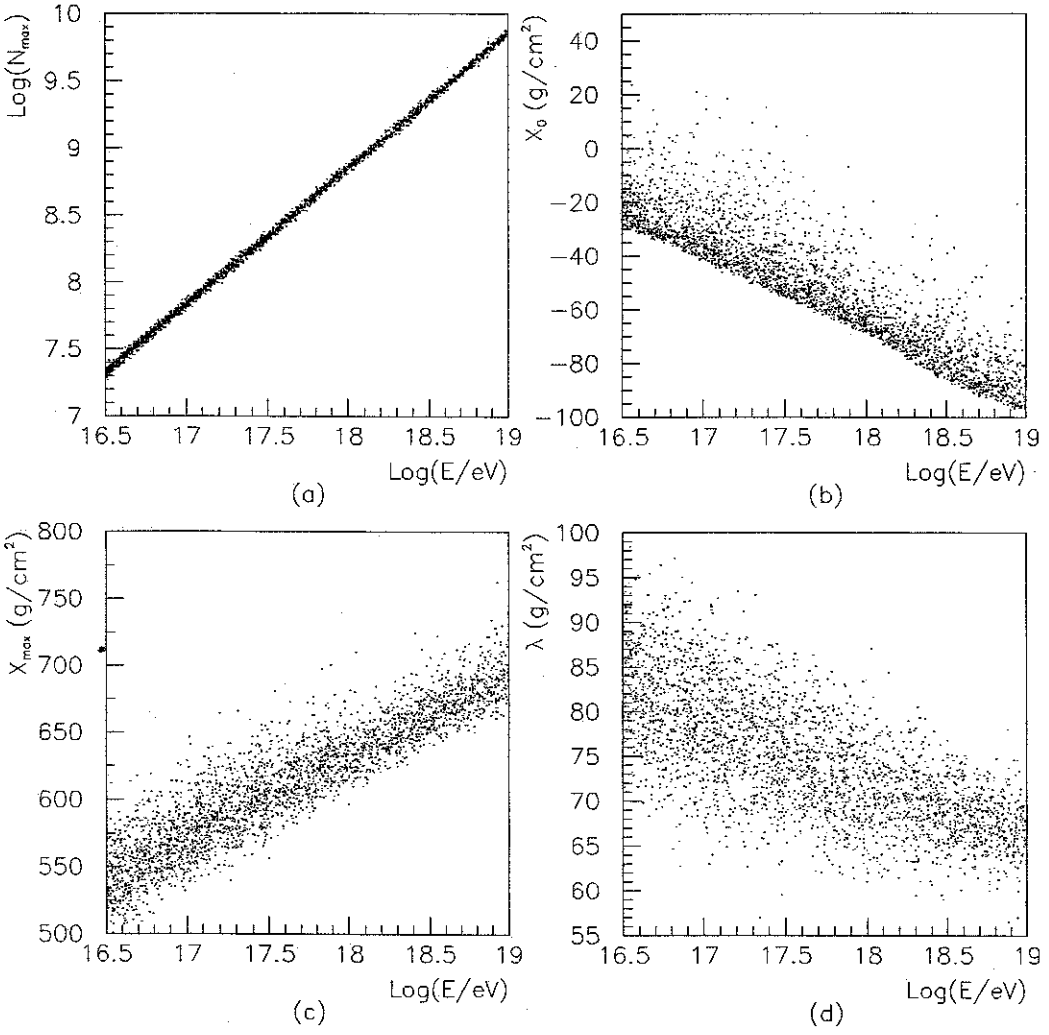

Figure 4.17: The four parameters of the Gaisser-Hillas function as a function of the primary energy for iron induced showers.

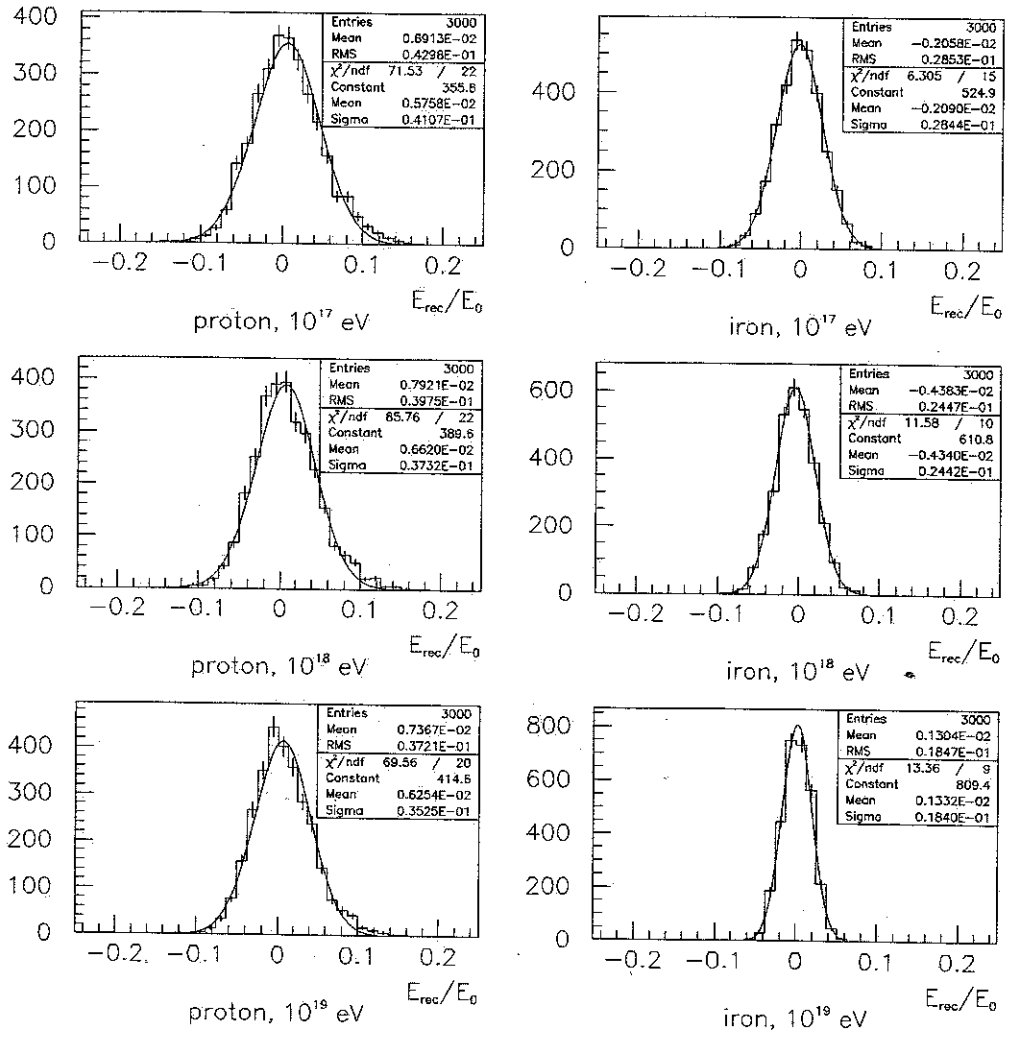

Figure 4.18: The ratio of reconstructed energy to input energy for proton and iron induced showers. 3,000 events are generated based on the parameterization at fixed energies and the energy is analytically calculated (Eq. (4.28)).

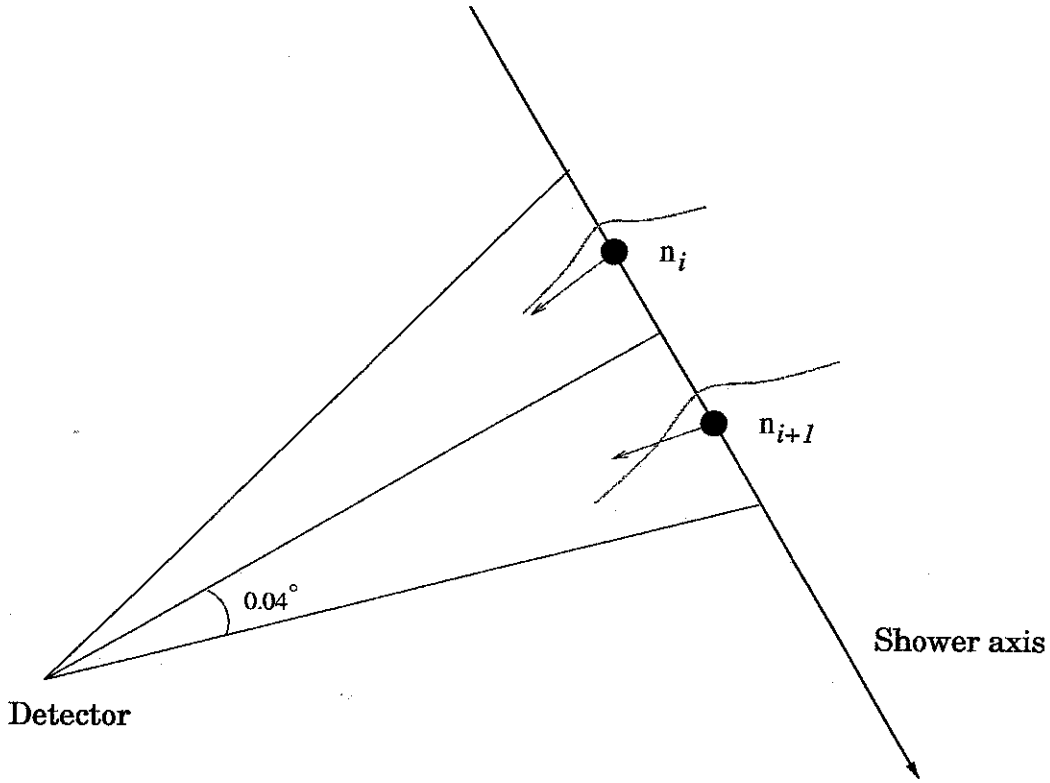

Figure 4.19: Light production and propagation.

4.19. Air density and temperature are calculated at the center of each segment, based on the U.S. standard atmosphere. We regard all charged particles as electrons. Thus, we can determine how many photons are generated via scintillation and Cherenkov radiation and how many reach the detector, taking into account the attenuation and scattering of light in the atmosphere.

Light Production

The fluorescence yield is measured by Kakimoto et al. for different temperatures and pressures at several fixed energies [144]. The fluorescence yield is defined as the number of photons per meter per electron and is given by

$$Y = \frac{(\frac{dE}{dx})}{(\frac{dE}{dx})_{1.4\text{MeV}}} \cdot \rho \Big\{ \frac{A_1}{1+\rho B_1 \sqrt{t}} + \frac{A_2}{1+\rho B_2 \sqrt{t}} \Big\}, \tag{4.29}$$

where $\mathrm{d}E/\mathrm{d}x$ is the energy loss rate of electrons in MeV/cm, ρ is the air density in kg/m^2 and t is the temperature in K. The constants A_1 and A_2 are 89.0 and 55.0 m^2 kg^{-1}, B_1 and B_2 are 1.85 and 6.50 m^2 kg^{-1} K$^{-1/2}$, respectively. The fluorescent light is emitted isotropically. Thus, the angular distribution is given by

$$\frac{\mathrm{d}^2 N_\gamma}{\mathrm{d}l\mathrm{d}\Omega} = Y\frac{N_e}{4\pi}. \tag{4.30}$$

The fluorescence yield is a function of $\mathrm{d}E/\mathrm{d}x$ of the electrons. However, we use the mean $\mathrm{d}E/\mathrm{d}x$ as a function of age as shown in Figure 4.2, instead of considering the energies of individual particles.

Charged particles moving through the atmosphere with a velocity larger than the local speed of light emit Cherenkov light. This light is emitted in a narrow cone around the direction of the particle. For a relativistic charged particle in air, the number of Cherenkov photons per unit length is given by [147]:

$$\frac{\mathrm{d}N_\gamma}{\mathrm{d}l} = \frac{2\pi\alpha}{c}\int\left(1-\frac{1}{\beta^2 n^2}\right)\mathrm{d}\nu, \tag{4.31}$$

where ν is the frequency of the radiation and n is the index of refraction of air. For $n \cong 1$, the integrand is approximated as

$$\begin{aligned} 1-(\beta n)^{-2} &= 1-\left(1-\frac{m^2c^4}{E^2}\right)(1+\delta)^{-2} \\ &\approx 2\delta - \frac{m^2c^4}{E^2}, \end{aligned} \tag{4.32}$$

where $\delta = n-1$. For air showers, the rate is

$$\frac{\mathrm{d}N_\gamma}{\mathrm{d}l} = \frac{2\pi\alpha}{c}N_e\int\mathrm{d}\nu\int_{E_{th}}^{\infty} f(E)\left(2\delta-\frac{m^2c^4}{E^2}\right)\mathrm{d}E, \tag{4.33}$$

where $f(E)$ is the energy spectrum of electrons and E_{th} is the threshold energy of Cherenkov radiation, which is given by

$$E_{th} = mc^2/\sqrt{2\delta}. \tag{4.34}$$

The angular distribution of Cherenkov light is

$$\frac{\mathrm{d}^2 N_\gamma}{\mathrm{d}l\mathrm{d}\Omega} = \frac{\mathrm{d}N_\gamma}{\mathrm{d}l}\frac{e^{-\theta/\theta_0}}{2\pi\sin\theta}, \tag{4.35}$$

where $\theta_0 = 0.83 E_{th}^{-0.67}$.

Light Propagation

The light produced by shower particles is attenuated by scattering and absorption in the atmosphere. We consider Rayleigh and Mie scattering of light. The amount of Rayleigh scattered light from N_γ is [147]:

$$\frac{\mathrm{d}N_\gamma}{\mathrm{d}l} = -\rho\frac{N_\gamma}{X_R}\left(\frac{400\mathrm{nm}}{\lambda}\right)^4, \tag{4.36}$$

where $X_R = 2{,}970$ g/cm^2 is the mean free path for scattering at 400 nm. For an isothermal atmosphere,

$$\rho = \rho_0 \exp(-h/H_0), \tag{4.37}$$

where H_0 is the atmospheric scale height and $\rho_0 = 0.00107$ g/cm^2 at 0°C at the Dugway site. The angular distribution is given by

$$\frac{\mathrm{d}^2 N_\gamma}{\mathrm{d}l\mathrm{d}\Omega} = \frac{\mathrm{d}N_\gamma}{\mathrm{d}l}\frac{3}{16\pi}(1+\cos^2\theta). \tag{4.38}$$

For Mie scattering, the rate of light production per unit distance [147] is

$$\frac{\mathrm{d}N_\gamma}{\mathrm{d}l} = -\frac{N_\gamma}{L_M}\exp(-h/H_M), \tag{4.39}$$

where $H_M = 1.2\,\mathrm{km}$ is the scale height and $L_M = 14\,\mathrm{km}$ is the attenuation length at $\lambda = 360\,\mathrm{nm}$. The angular distribution is strongly peaked in the forward direction and can be approximated by an exponential function,

$$\frac{\mathrm{d}^2 N_\gamma}{\mathrm{d}l\mathrm{d}\Omega} = a\frac{\mathrm{d}N_\gamma}{\mathrm{d}l}e^{-\theta/\theta_M}, \tag{4.40}$$

where $a = 0.80$ and $\theta_M = 26.7°$.

The attenuation of light is described by the transmission factor. The Rayleigh transmission factor is given by

$$T_R = \exp\Big\{ -\Big(\frac{\Delta x}{X_R}\Big)\Big(\frac{400\text{nm}}{\lambda}\Big)^4 \Big\}, \tag{4.41}$$

where Δx is the distance in depth between source and detector. For Mie scattering, we have

$$T_M = \exp\Big\{ \frac{H_M \sec\theta}{L_M} \Big(\exp(-h_1/H_M) - \exp(-h_2/H_M) \Big) \Big\}, \tag{4.42}$$

where h_1 and h_2 are heights of source and detector respectively.

The transmission of the ozone layer is given by

$$T_o = \exp(-\Delta x_o L_o), \tag{4.43}$$

where Δx_o is the integrated ozone density along the line between source and detector and L_o is the attenuation coefficient. Therefore, the overall transmission factor is

$$T_{atm} = T_R \cdot T_M \cdot T_o. \tag{4.44}$$

4.4.3 Detector Response

The fluorescent light and Cherenkov light are emitted at the shower track. For simplicity, we do not take into account multiple scattered light in the simulation. However, unlike the fluorescent light, the Cherenkov light is emitted more intensely along the shower track, so we need to consider the Cherenkov light scattered by air molecules and aerosols. In consequence, there are four components of light produced by shower particles in the simulation, as illustrated in Figure 4.20:

- *Fluorescent light*
- *Direct Cherenkov light*
- *Rayleigh scattered Cherenkov light*
- *Mie scattered Cherenkov light*

We ignore the scattered fluorescent light in our calculation. In the simulation, the number of photons collected with an ideal circular mirror is estimated for each segment along the shower track. During this process, the formulae for light production and propagation are used, and γ in $\mathrm{d}^2N_\gamma/\mathrm{d}l\mathrm{d}\Omega$ is replaced with *fluo*, *chk*, *rayl* and *mie* for fluorescent light, direct Cherenkov light, Rayleigh and Mie scattered Cherenkov light, respectively. The number of photons can be determined analytically:

$$N_\gamma = \sum_{\lambda=300}^{420} T_{atm}(\lambda)\left(\frac{\mathrm{d}^2N_{fluo}}{\mathrm{d}\Omega}(\lambda,\theta)+\frac{\mathrm{d}^2N_{chk}}{\mathrm{d}\Omega}(\lambda,\theta)v+\frac{\mathrm{d}^2N_{rayl}}{\mathrm{d}\Omega}(\lambda,\theta)+\frac{\mathrm{d}^2N_{mie}}{\mathrm{d}\Omega}(\lambda,\theta)\right)\delta l\delta\Omega, \tag{4.45}$$

where δl is the length of the segment in meter and $\delta\Omega$ is given by

$$\delta\Omega = \frac{A_o\cos(\phi)}{r^2}, \tag{4.46}$$

where r is the distance between the detector and the source, A_o is the mirror area and ϕ is the angle between mirror pointing direction and the direction of the incoming light.

Once the number of photons hitting the ideal mirror is estimated, the individual photons are traced assuming an actual mirror obscured by a cluster box. The number of photons hitting the mirror surface is determined by considering the actual mirror shape, spherical aberration, mirror reflectivity and the obscuration by the cluster box. Figure 4.21 shows the simulated spot due to the imperfection of the mirror surface. This effect broadens the impact position on the cluster box. The number of photoelectrons is determined by the number of photons weighted by the tube response profile, considering quantum efficiency and the UV filter transmission factor.

In practice, we use a table of the simulated average tube responses for various shower tracks, instead of tracing all photons every time. This is a so-called 'ray-tracing' table. To build the table, a large number of photons are generated uniformly along shower tracks horizontally placed every 0.1° up to 11° from the center of the mirror. In turn, the tracks are rotated by 0° to 360°. The relative tube responses

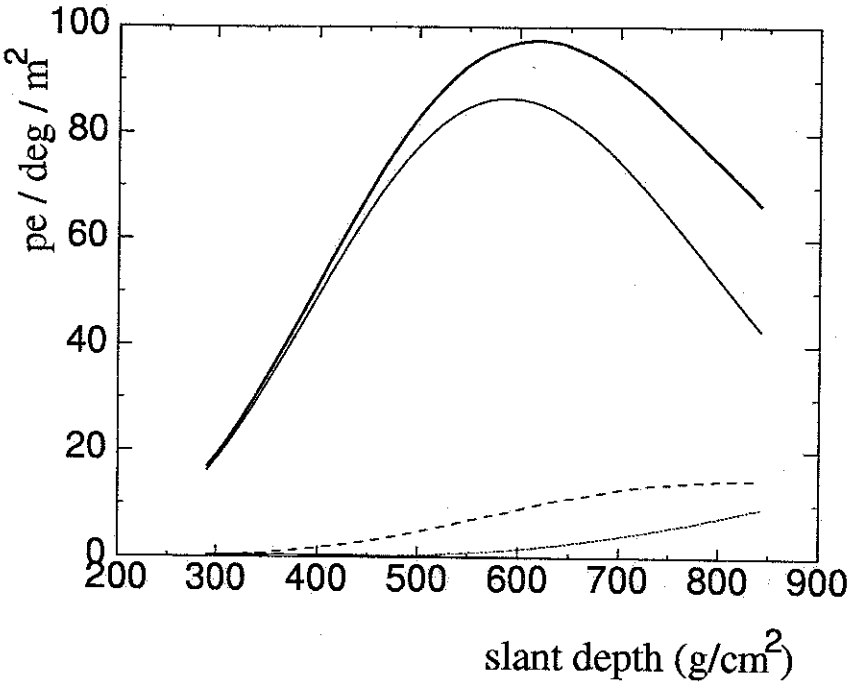

Figure 4.20: For a proton induced shower at 10^{18} eV, the number of photoelectrons per degree per area is estimated by summing up four components (thick solid line) of light sources, which are fluorescent light (thin solid line), Rayleigh scattered light (dashed line), Mie scattered light (dotted line) and direct Cherenkov light. In this case, the contribution of direct Cherenkov light is negligible.

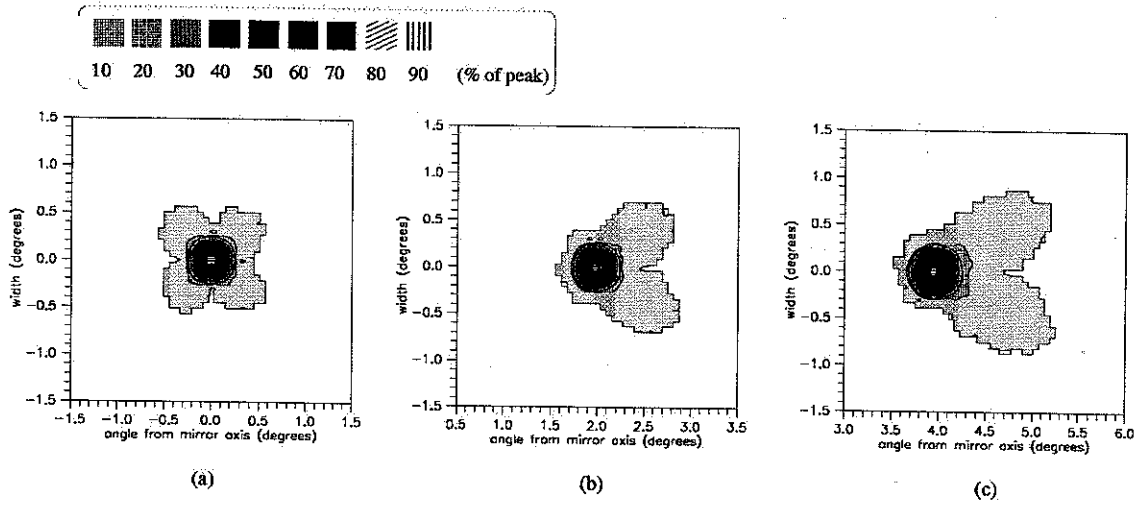

Figure 4.21: Mirror spot patterns for points off by 0°, 2° and 4° from the center of the cluster [148].

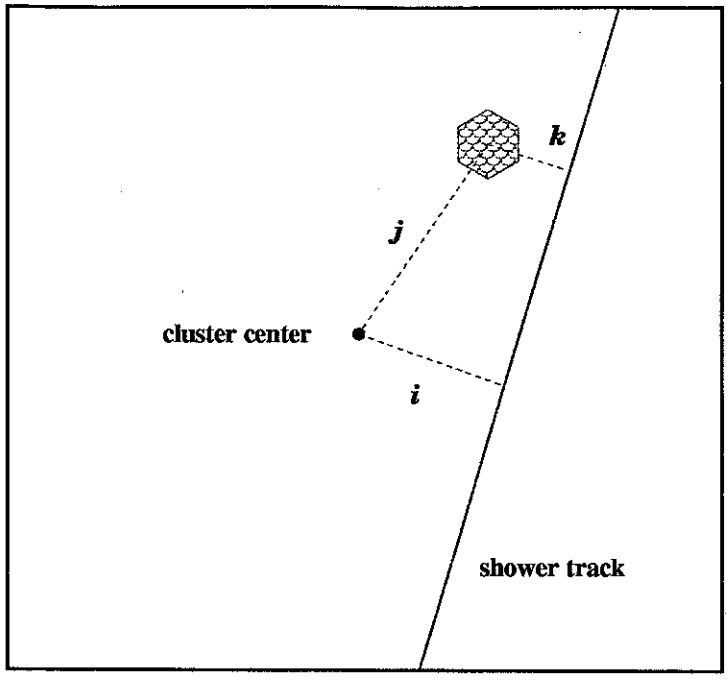

Figure 4.22: The three parameters to determine tube response for a given shower track.

for triggered tubes are recorded together with tube location parameters (i, j, k) as shown in Figure 4.22.

To consider the shower lateral spread, the initial position of the photon is displaced, based on the lateral shower distribution (the NKG function described in Chapter 2) which is extended to 7.5 Molière units. The size of the lateral bin is 0.05 Molière units.

Sky noise is added to the tube signal from a Poisson distribution with a mean of 40 pe/μs. In case of the trigger, the tube signal is integrated in the 1.2 μs time window and the trigger time is calculated and converted into an equivalent Time to Digital Converter (TDC) value. Finally, TDC and Charge to Digital Converter (QDC) values are saved for all triggered tubes.

Chapter 5

EVENT RECONSTRUCTION

To reconstruct air showers induced by cosmic rays from tube signals, triggers caused by various background and noise sources must be filtered out. Then, the shower-detector plane for triggered tubes is determined. Using tube trigger times, the shower axis within the plane is in turn determined. The knowledge of light production and propagation in the atmosphere enables us to reconstruct the longitudinal profile of the shower as the number of charged particles in atmospheric depth.

5.1 Data Processing

The tube signals are stored for the tubes that satisfy the trigger condition as described in Chapter 3. However, most of the triggered events are noise events and must be eliminated. Then, the number of photoelectrons is converted into the number of photons at the surface of the PMT using calibration data taken every night.

5.1.1 Raw Data

The HiRes prototype detector took data from August 1993 to October 1996. In total, thirty-nine months of data were recorded on magnetic tapes. Each night has several parts which contain about two hours of data. The detector 'start and stop' times were recorded in a file (*.on) and the weather code was logged in a file (*.note) every hour. The information was extracted and saved in a separate file on a monthly basis for future use. The total operating time was 2,351 hours. The raw data was

converted into Data Storage Template (DST) formatted data by 'rawtodst'. A DST bank is similar to a 'common block' in FORTRAN or a 'structure' in C. A RAW1 bank, which contains QDC and TDC values for triggered tubes, is produced for each truncated Julian day[1].

5.1.2 Calibration

Using the electronics (*.cal2.data) and YAG laser (*.mir.lp.sum) calibration, 'dstcal' produces a PHO1 bank, which contains the calibrated numbers of photons and trigger times for the triggered tubes. The electronics calibration using a Programmable Pulse Generator (PPG) provides a pedestal of QDC and TDC as well as α, β and the asymptotic gain for the pre-amplifier in Eq. (3.3). The number of photons is calculated by taking into account the tube gain and the quantum efficiency after subtracting pedestal, and is then multiplied by a correction factor that is the relative response of each PMT to the average response of the cluster as determined by YAG laser calibration. The trigger times of the tubes are corrected by adding the mirror trigger time determined by the GPS clock. Photons in the PHO1 bank are those at the face of the tube after reflecting off the mirror and passing through the UV filter.

5.1.3 Rayleigh Filter

In the data, most events are triggered by sky noise or artificial sources like flashers and airplanes. These background events can be distinguished from real events which look like a straight line. To do so, we can adopt an idea from random walk in two dimensions. After n steps, the resultant vector is the sum of random unit vectors. The magnitude distribution of the resultant vector is described by the Rayleigh distribution. The Rayleigh probability density function is given by

$$f(r) = \frac{r}{s^2} \exp\left\{ -\frac{r^2}{2s^2} \right\}, \tag{5.1}$$

[1]Truncated Julian day: the number of days since midnight on May 24, 1968 at which time the Apollo missions to the Moon were underway.

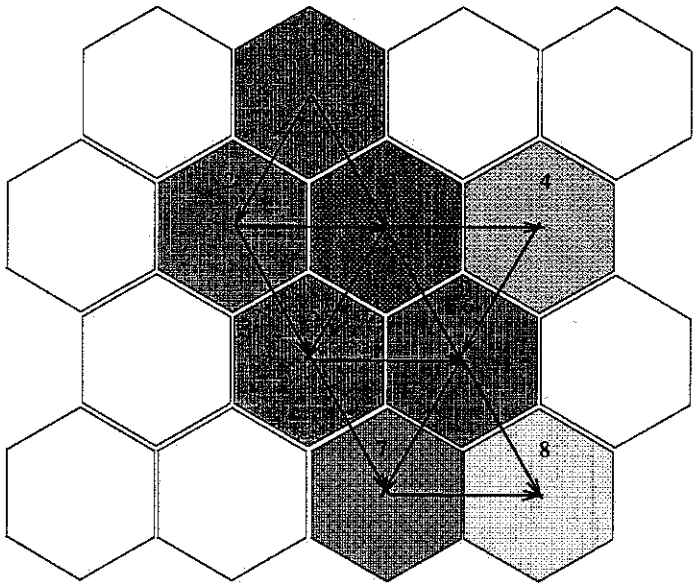

Figure 5.1: The tubes are numbered by trigger time. The unit vectors are added in time order to determine the resultant Rayleigh vector.

where r is the magnitude of the resultant vector after n steps and $s^2 = n/2$. The probability to observe a net displacement of $r > R$ after n steps is

$$P(r > R) = \int_R^\infty f(r)\, \mathrm{d}r = \exp\Big\{ -\frac{R^2}{n} \Big\}. \tag{5.2}$$

In our analysis, we require that $P \leq 0.01$ and a minimum of three neighboring triggered tubes.

To apply the Rayleigh filter to cosmic ray events, we add up unit vectors connecting neighboring triggered tubes in time order. In Figure 5.1, the tubes are numbered by trigger time. The first triggered tube (1) makes two unit vectors ($\vec{r}_{12}$, $\vec{r}_{13}$) and the second triggered tube (2) makes another two unit vectors ($\vec{r}_{23}$, $\vec{r}_{25}$), and so on. We can summarize the procedure as follows:

$$\vec{r} = \sum_{i=1}^{N} \sum_{j=i}^{N} \delta_{ij}\, \vec{r}_{ij}, \qquad \delta_{ij} = \begin{cases} 1 & : \ |\vec{r}_{ij}| = 1 \\ 0 & : \ |\vec{r}_{ij}| \neq 1 \end{cases}, \tag{5.3}$$

where N is the number of triggered tubes.

This process is done by 'hpass2' which has been used for filtering the HiRes-

I monocular data [117], and this code was modified for the HiRes prototype data. After the events are passed through the Rayleigh filter, the events are classified into three categories - upward, downward and horizontal events - and are recorded in separate files. The showers whose direction is within 20° of the horizon are regarded as horizontal events. Most of the downward and horizontal events are flasher or laser tracks. Only downward events are used in this study, and about 16 % of the events pass through the Rayleigh filter.

5.2 Shower Geometry Reconstruction

For stereo eyes, two planes made by each eye meet a line if they are not in parallel. However, a monocular eye determines only one plane. To determine the shower axis within the plane, we have to use the tube trigger times.

5.2.1 Plane Fit

An amplitude weighted plane fit is performed to determine the shower-detector plane. The amplitude is defined as the number of photoelectrons in the tube. The χ^2 is defined as

$$\chi^2 = \sum_i^N \frac{[(\hat{\mathrm{n}} \cdot \hat{\mathrm{n}}_i)]^2 \cdot S_i}{\sigma_i^2}, \tag{5.4}$$

where $\hat{\mathrm{n}}$ is the plane normal vector, $\hat{\mathrm{n}}_i$ is the tube pointing direction vector, S_i is the number of photoelectrons and N is the total number of triggered tubes. σ_i^2 is defined as $(S_i + S_{noise})/S_i$, where S_{noise} is a background signal which is 40 pe/μs. The noise comes from night sky and electronics. Even cosmic ray events often contain several noise tubes. Thus, during the plane fitting, the noise tubes are rejected based on the fact that the tubes triggered by cosmic ray events are strongly correlated spatially and temporally. Grouping the triggered tubes into clusters, the largest cluster is assumed to be formed by a cosmic ray event, and the other small clusters are rejected if they are not on the track determined by the largest cluster.

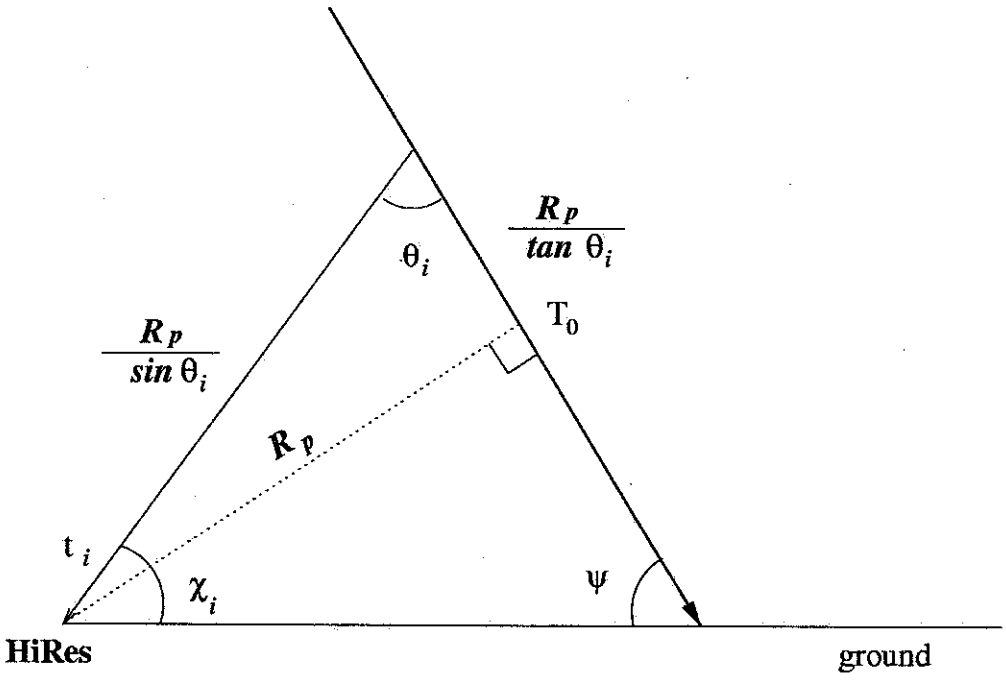

Figure 5.2: The determination of the expected trigger time of the ith tube.

5.2.2 Time Fit

Once we determine the shower-detector plane, the shower axis within the plane can be obtained by using tube trigger times in monocular reconstruction. First, we define a reference time T_0 at which the shower passes at the closest point to the detector. Figure 5.2 shows the track geometry within the shower-detector plane. The trigger time of ith tube can be written as

$$\begin{aligned} T_i &= T_0 - \frac{R_p}{c\tan\theta_i} + \frac{R_p}{c\sin\theta_i} \\ &= T_0 + \frac{R_p}{c}\tan\left(\frac{\theta_i}{2}\right), \end{aligned} \tag{5.5}$$

where R_p is the impact parameter of the shower and θ_i is the light emission angle, which can be replaced using $\theta_i = \pi - \psi - \chi_i$. R_p and ψ are obtained by minimizing χ^2:

$$\chi^2 = \sum_i^N \frac{1}{\sigma_i^2}\left\{t_i - \left(T_0 + \frac{R_p}{c}\tan\left(\frac{\pi - \psi - \chi_i}{2}\right)\right)\right\}^2, \tag{5.6}$$

where N is the total number of triggered tubes and t_i is the trigger time of the ith tube. σ_i is $300/\sqrt{S_i}$, where S_i is the tube signal in photoelectrons. Since it is difficult to estimate the error of the trigger time, the error was scaled so that χ^2 is close to 1 at the minimal point. The error is defined to be inversely proportional to the square root of tube signal.

5.2.3 Additional Filters

Based on the study of HiRes-MIA hybrid data and experience with HiRes-I [117], several additional filters are applied with the aid of 'hpln' code which, like the Rayleigh filtering code, is also modified for the HiRes prototype data. The track length, inverse angular speed of the track and the correlation between trigger time and tube viewing angle are used to filter out remaining noise events. Figure 5.3 shows the distribution of these parameters for the HiRes prototype data. A total of 22,730 events survived the filtering.

Track length cut: If the shower track is too short, it is difficult to get the correct shower geometry in monocular reconstruction. Thus, tracks shorter than 15° are rejected. However, we found that some events with long tracks have a small number of triggered tubes. Thus, we require a minimum of 0.85 good tubes per degree and a maximum number of 4 good tubes per degree along the track.

Angular speed cut: To eliminate events close to the detector, we use an angular speed cut. Events with angular speed faster than 58.22 ns/degree are rejected. Roughly speaking, this means that tracks with R_p less than 1 km are rejected.

Correlation cut: The correlation between trigger time and viewing angle χ_i in the plane is used to reject noise events. Figure 5.5 shows the strong correlation between trigger time and χ_i. The correlation coefficient is required to be greater than 0.985.

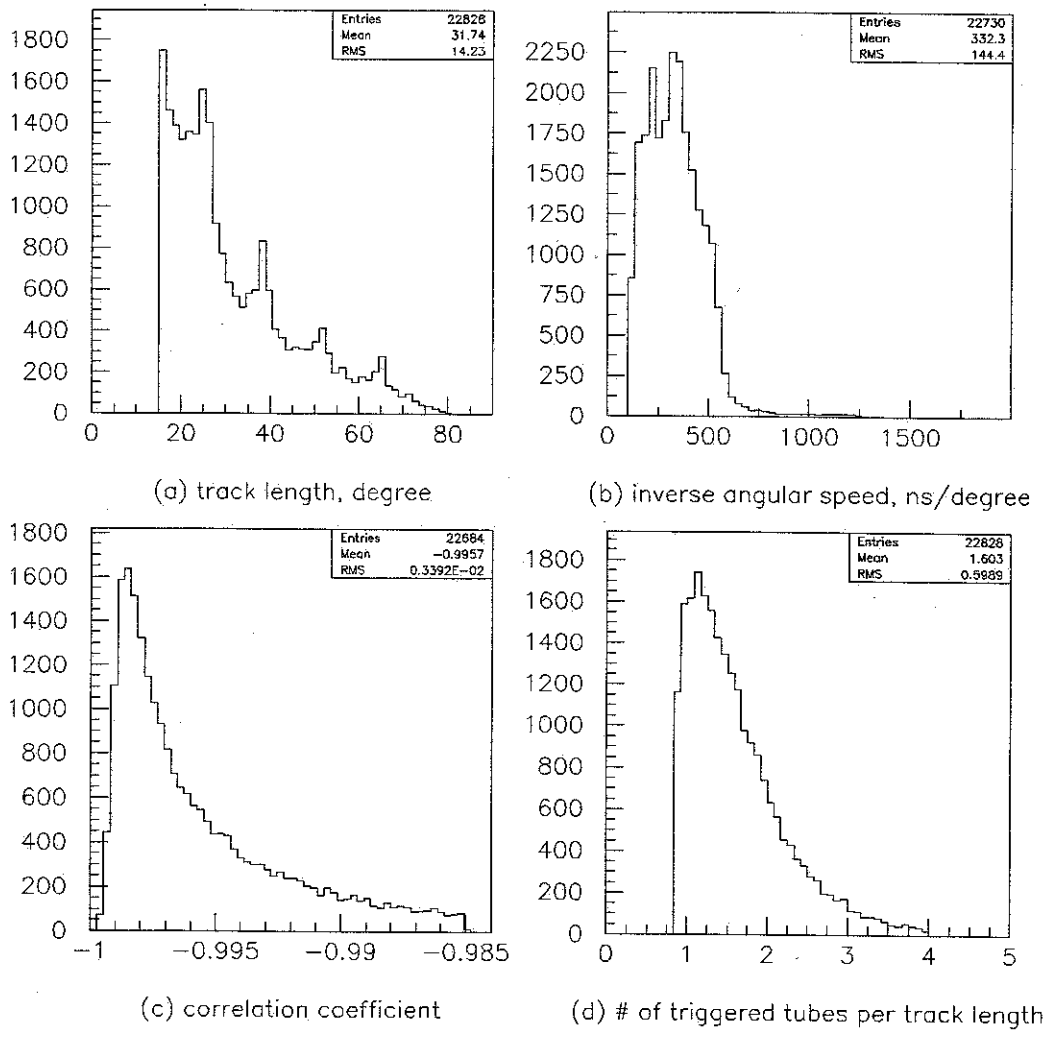

Figure 5.3: The distributions of the filtering parameters for HiRes prototype data.

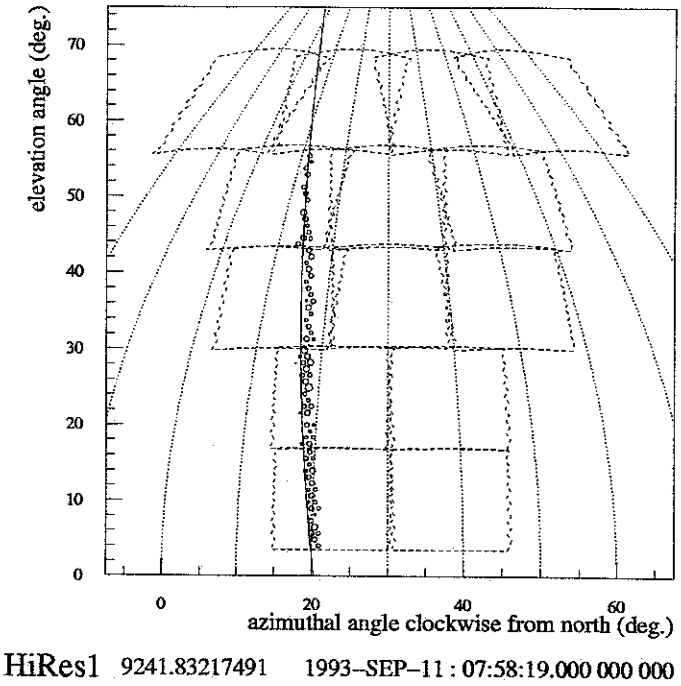

Figure 5.4: A typical event as seen by the HiRes prototype detector.

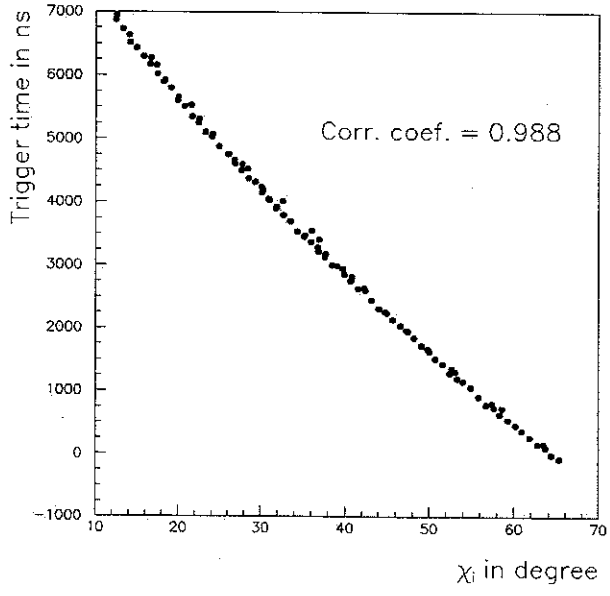

Figure 5.5: Trigger time versus viewing angle for the event shown in Figure 5.4.

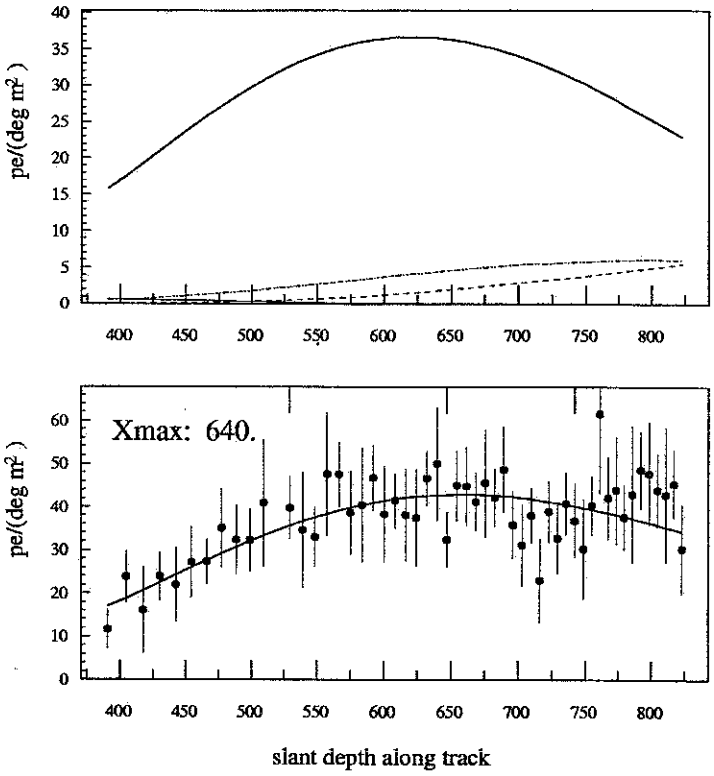

Figure 5.6: Example of a profile fit. In the upper plot, the fluorescent light (solid line), as well as the contributions of Rayleigh (dotted line) and Mie (dashed line) scattered Cherenkov light are shown. The light contributes to the predicted signals which are compared to experimental bin signals in the lower plot.

5.3 Shower Profile Fit

We divide the shower track into 1° bins. If the center of a tube lies within the bin, the tube signal is added to the bin signal. The number of photoelectrons per m^2 per degree is recorded with the bin direction in the BIN1 bank.

Once we have the binned signals, we calculate the amount of light emitted at the shower axis, taking into account the attenuation and scattering of the light in the atmosphere. Then, the contamination of the Cherenkov light has to be subtracted since the amount of fluorescent light is proportional to the number of charged particles. However, we have to know the longitudinal shower profile prior to subtraction. Thus, the contamination of the Cherenkov light is determined by an iteration process.

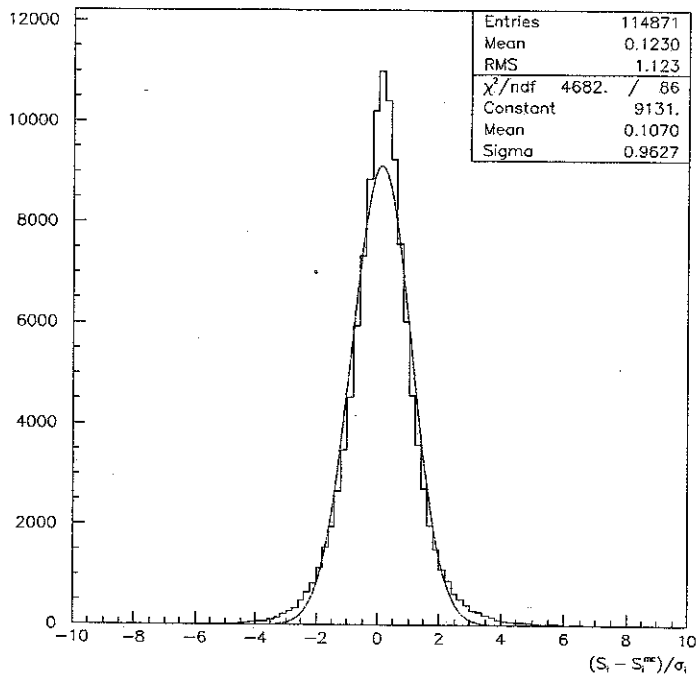

Figure 5.7: Distribution of the residuals of the bin signals for all of the HiRes prototype events.

The Gaisser-Hillas function, normalized by N_{max} at X_{max}, is used as a shower profile, and λ is set to 70 g/cm^2 and X_0 is set to -20 g/cm^2. Thus, the shower profile is a function of X_{max} only. X_{max} is determined by minimizing

$$\chi^2 = \sum_i \frac{(S_i - N_{max} S_i^{mc})^2}{\sigma_i^2}, \tag{5.7}$$

where S_i is the bin signal and S_i^{mc} is the simulated bin signal, and N_{max} is given by differentiating the above equation:

$$N_{max} = \frac{\sum_i (S_i S_i^{mc})/\sigma_i^2}{\sum_i (S_i^{mc} S_i^{mc})/\sigma_i^2}, \tag{5.8}$$

where $\sigma^2 = \sigma_{poisson}^2 + \sigma_{noise}^2 + \sigma_{mc}^2$. $\sigma_{poisson}$ is the square root of the tube signal and σ_{noise} is the square root of 40 pe/μs. σ_{mc} is the error due to the uncertainty in the tube pointing direction. Figure 5.6 shows an example of a profile fit. This figure

shows the four contributions of light emitted from the shower track determined by the iteration process. The error of the profile fit is checked by plotting the residual distribution from the shower profile fits, as shown in Figure 5.7. The residual is defined as $(S_i - S_i^{mc})/\sigma_i$, where S_i is the bin signal, S_i^{mc} is the simulated signal and σ_i is the error of the bin. The distribution is fitted with a Gaussian function with a sigma of 0.96. The main contribution to the error is the Poisson fluctuation of the number of photons.

Chapter 6

RESULTS FOR COMPOSITION AND FLUX

The HiRes prototype detector took data for about three years. It covered a wide energy range from 10^{17} to 10^{19} eV. The depth of the shower maximum is used as an indicator of mass for this study. The fact that light nuclei penetrate more deeply than heavy ones enables us to deduce the mass of the primary particles. However, because of the large fluctuation in the shower maximum depth, it is not possible to measure the mass of the primary particle on an event-by-event basis. Only the average mass can be deduced from the average shower maximum, but this interpretation depends on the hadronic interaction model. We will show the results for the composition of cosmic ray particles in this chapter. In addition, the flux of cosmic rays is determined by estimating the detector aperture by means of the detector simulation.

6.1 Event Selection

As mentioned in Chapter 4, one of the roles of detector simulation is to determine criteria for the selection of good events. This can be done by eliminating poorly reconstructed events which would otherwise cause a bias in the interpretation of the data. To do so, we have chosen several elimination criteria to enhance the resolution. These cuts are applied to the data as well as to the simulated events.

The minimum viewing angle (θ_{min}) between the triggered tube and the shower

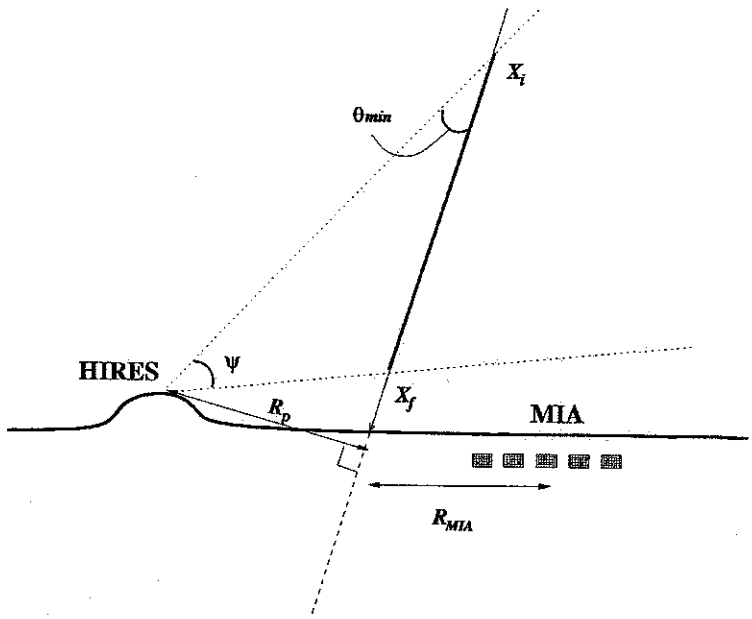

Figure 6.1: Shower geometry.

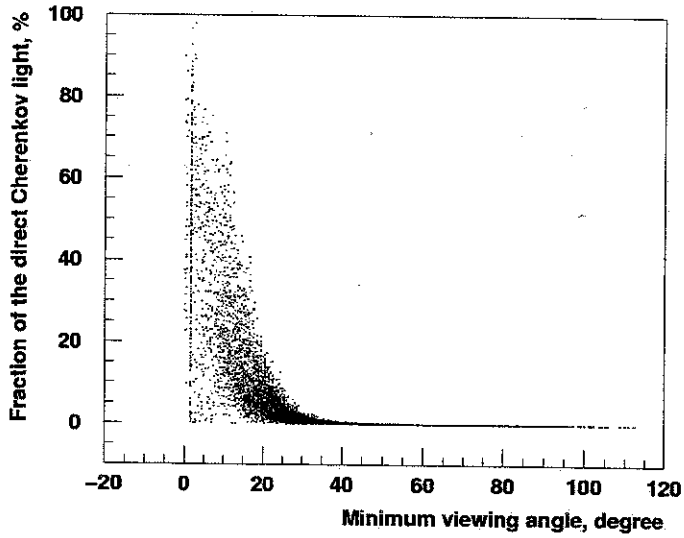

Figure 6.2: The fraction of the direct Cherenkov light versus the minimum viewing angle for all data.

Variables	Cut conditions	
	Hybrid data	Monocular data
Angular track length	$> 20°$	$> 44°$
X_{max} observation	$X_i < X_{max} < X_f$	$X_i < X_{max} < X_f$
Track length $(X_f - X_i)$	> 250 g/cm^2	> 300 g/cm^2
δX_{max}	< 50 g/cm^2	< 50 g/cm^2
Minimum viewing angle	$> 10°$	$> 14°$
χ^2/dof	< 10	< 10
R_{MIA}	< 2 km	–
Zenith angle	–	$< 60°$

Table 6.1: Cut conditions for hybrid and monocular data. X_i and X_f are the depths of the highest and lowest points of the shower track, respectively. δX_{max} is the error of the shower maximum and R_{MIA} is the core distance from the center of MIA.

track (Figure 6.1) is employed to eliminate events dominated by Cherenkov light. The Cherenkov light is emitted intensely along the shower axis. Consequently, the estimation of the Cherenkov light is strongly dependent on the shower geometry. As shown in Figure 6.2, the contamination of the direct Cherenkov light in the signal increases suddenly below $\theta_{min} \approx 20°$. For better quality of the profile fit, the χ^2 per degree of freedom and the error of X_{max} should be less than 10 and 50 g/cm^2, respectively. The shower maximum depth is required to be observed within the field of view of the detector. To enhance the quality of the reconstruction of shower geometry, the length of the shower track is required to be greater than 300 g/cm^2 $(X_f - X_i)$ and $44°$ (ψ) seen by the detector. The cut conditions for the HiRes prototype monocular data are similar to those for the MIA-HiRes hybrid data, but employ an additional zenith angle cut because the monocular reconstruction of the shower axis works poorly for inclined showers whose zenith angle is larger than $60°$. For hybrid data, the core distance from the center of MIA is used to obtain sufficient information on the arrival times of shower particles (MIA covers 370 m $\times$ 370 m and is located 3.3 km away from HiRes). The cut conditions are summarized in Table 6.1. Figures 6.3 and 6.4 show the X_{max} resolution versus the cut parameters before and after applying the cuts for 20,000 proton induced showers. After the cuts, the resolution is significantly

improved.

Figures 6.5 and 6.6 show the resolutions of the energy, X_{max}, R_p and ψ for proton and iron induced showers, respectively. 20,000 triggered events are generated from 10^{17} to 10^{19} eV with a spectrum of $dN/dE \propto E^{-3}$ as described in Chapter 4. 989 proton and 1,056 iron events remained after applying the cuts. The energy resolution is 14.4 % and 8.5 % for proton and iron showers, respectively. The mean of the resolution is shifted by 5.9 % and -10.8 % for proton and iron, because of the use of the average energy conversion (Eq. (4.12)) for hadronic showers due to the lack of knowledge of the type of primary particles. The energy resolution of the HiRes prototype detector is better than that of the Fly's Eye monocular (33 %) and stereo (24 %) detectors, and is comparable to that of the MIA-HiRes prototype hybrid detector (16 % for p and 10 % for Fe). The resolution of the shower maximum is 56.8 g/cm^2 and 58.1 g/cm^2 for proton and iron showers, respectively. For geometry reconstruction, the resolution of the impact parameter (R_p) is 3.1 and 3.3 % and that of ψ is 2.9° and 3.3°, with a shift of $-0.7°$ and $-0.6°$ for proton and iron induced showers. The distributions of the energy, N_{max}, R_P and zenith angle are compared for simulation and experimental data as shown in Figure 6.7. The comparison shows that experimental data and simulated events agree to a satisfying degree. We see a slight difference in the zenith angle distribution, which indicates that the detector simulation is not perfect. As shown in Figure 6.8, the reconstruction procedure does not have a bias on the zenith angle determination since the mean of the resolution of the zenith angle is very small ($< 1°$). Thus, the detector simulation may have intrinsic problem involving light production and propagation, etc.

For 2,881 events triggered by both MIA and HiRes prototype detectors, the shower tracks are reconstructed by the hybrid and monocular reconstruction methods, respectively. In the hybrid geometry reconstruction, the shower-detector plane is determined by a linear fit weighted by tube signals from the HiRes detector. Then, the muon arrival times are used to determine the shower axis within the plane, instead of the time fit as in the monocular reconstruction. Figure 6.9 shows the comparison between

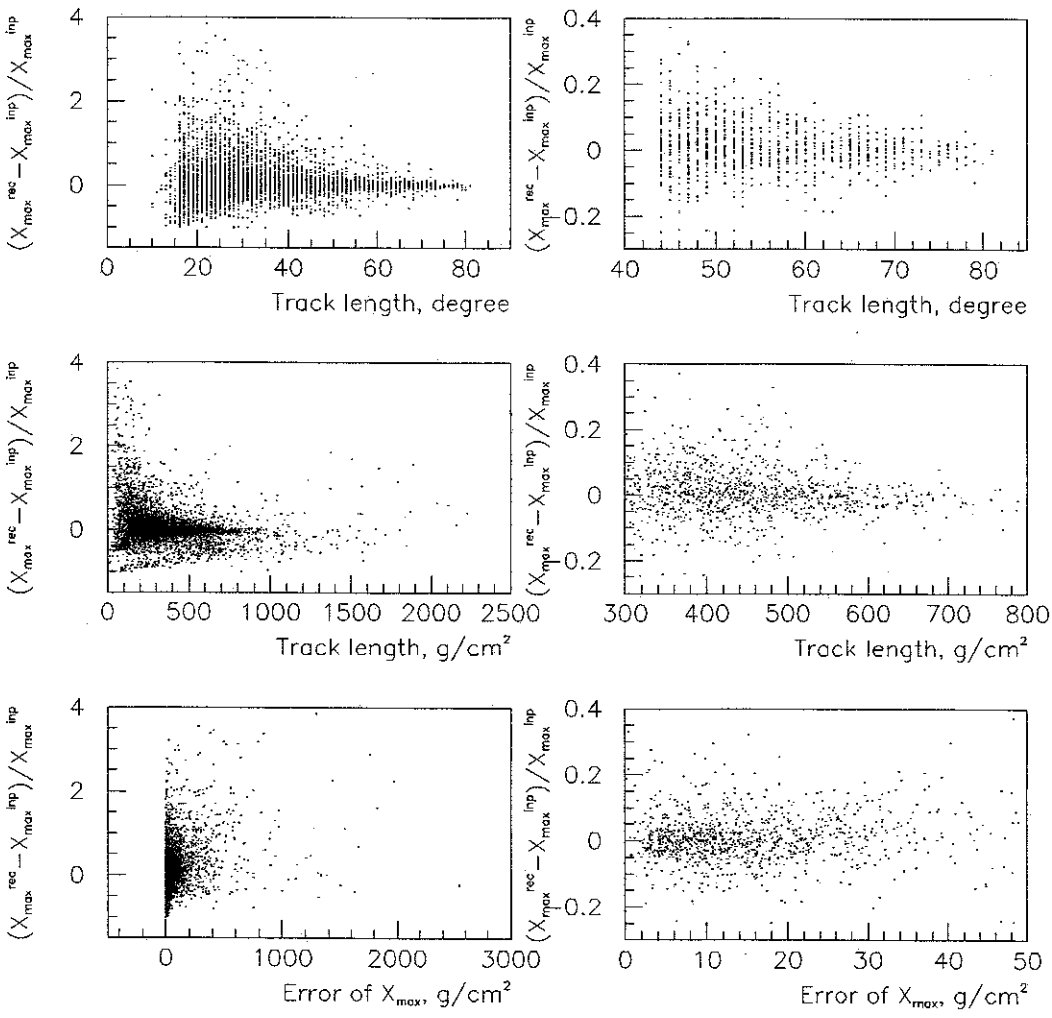

Figure 6.3: The X_{max} resolution versus angular track length, track length and the error of X_{max} before and after applying the cuts for 20,000 proton induced showers. X_{max}^{inp} and X_{max}^{rec} represent the input and reconstructed shower maximum depths.

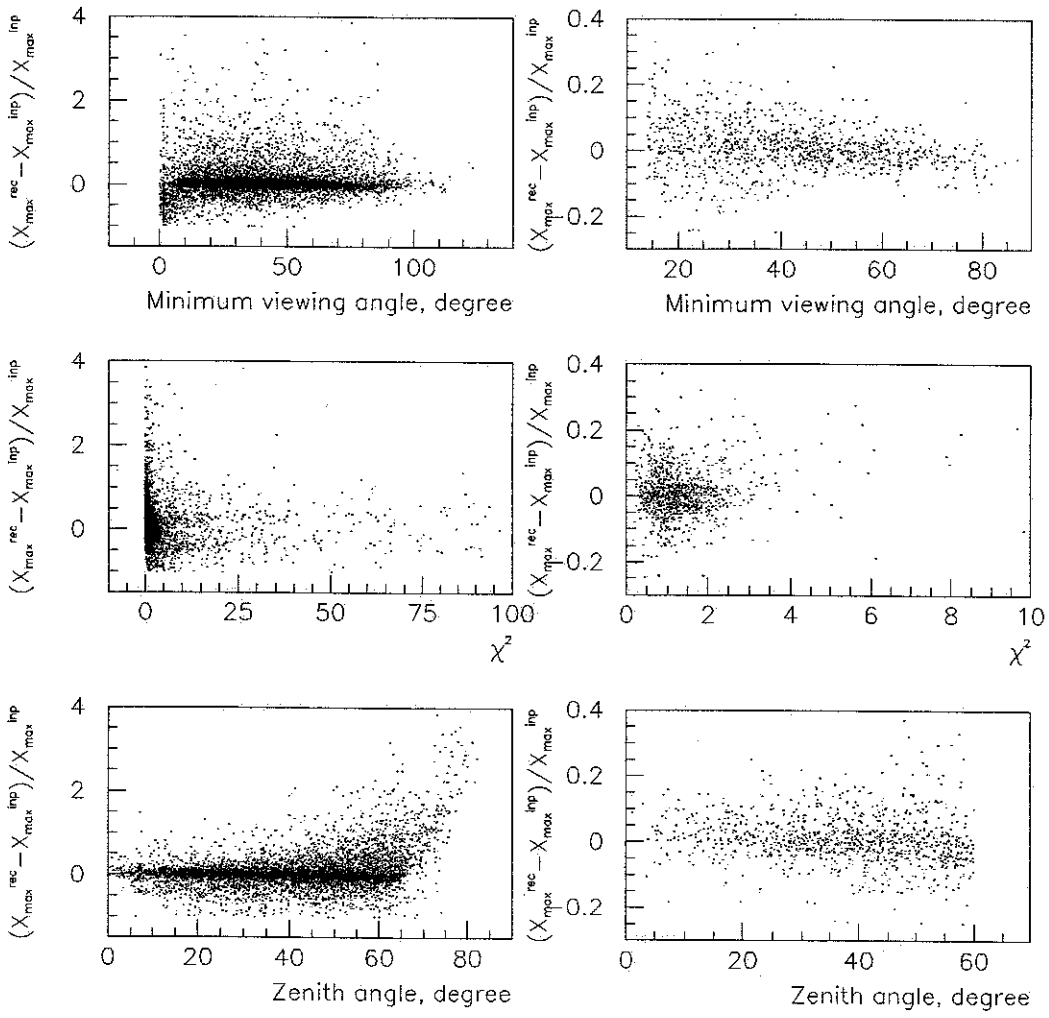

Figure 6.4: The X_{max} resolution versus the minimum viewing angle, χ^2 and the zenith angle before and after applying the cuts for 20,000 proton induced showers. X_{max}^{inp} and X_{max}^{rec} represent the input and reconstructed shower maximum depths.

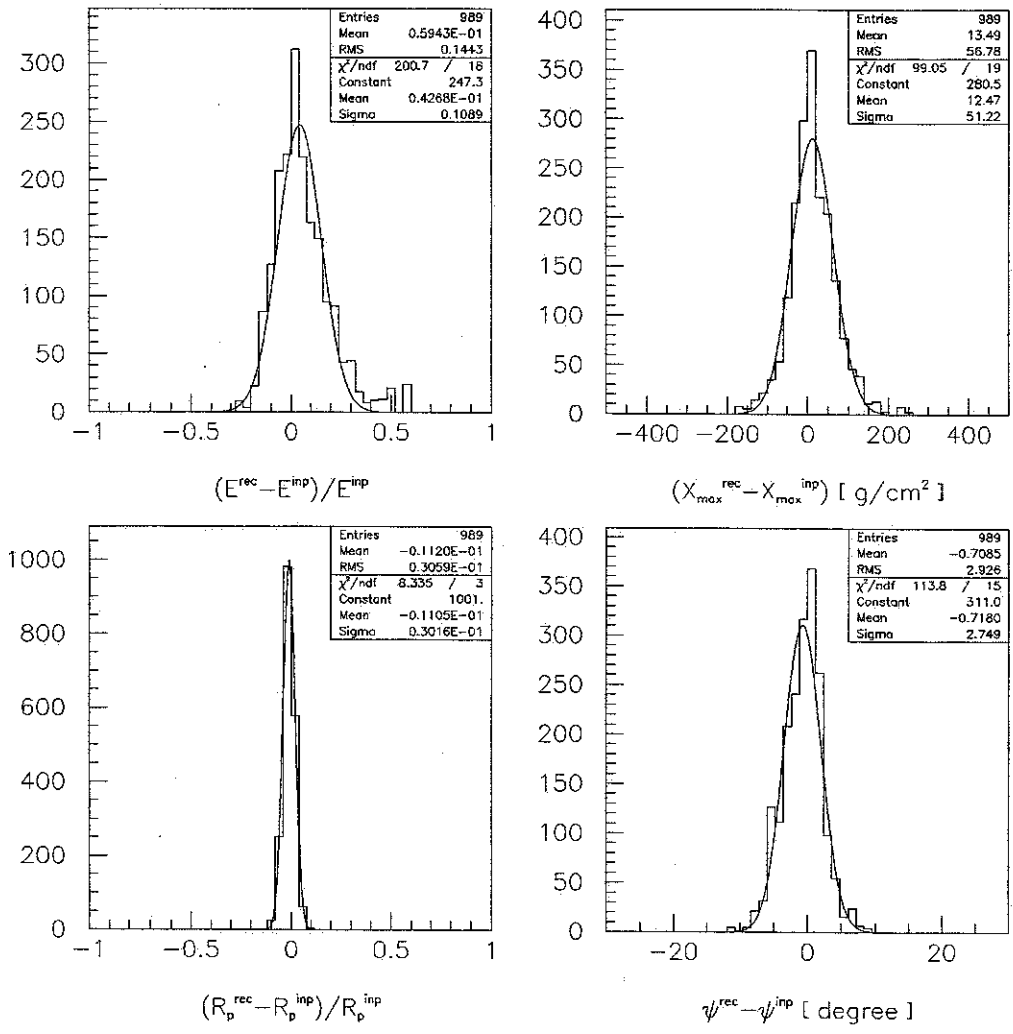

Figure 6.5: The resolution of energy, X_{max}, R_p and ψ for proton induced showers. 20,000 triggered events are generated from 10^{17} eV to 10^{19} eV.

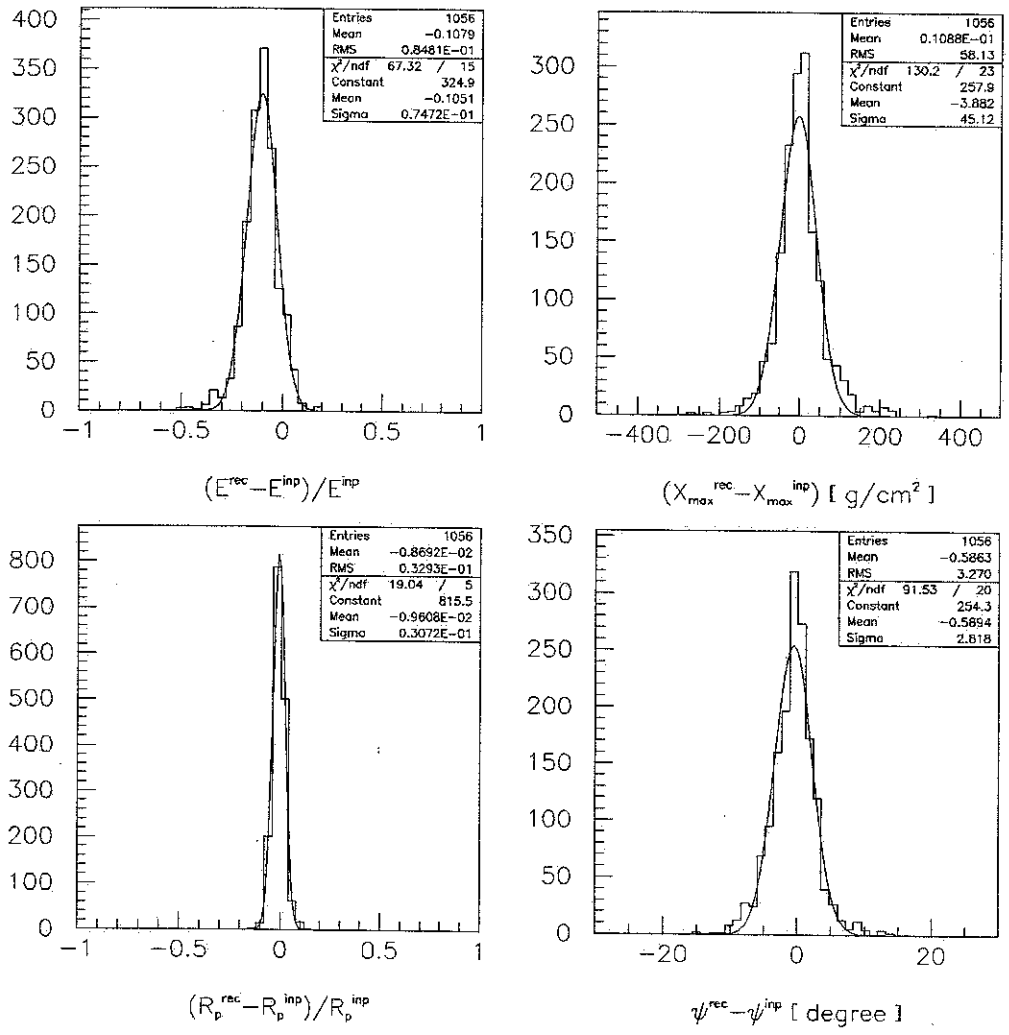

Figure 6.6: The resolution of energy, X_{max}, R_p and ψ for iron induced showers. 20,000 triggered events are generated from 10^{17} eV to 10^{19} eV.

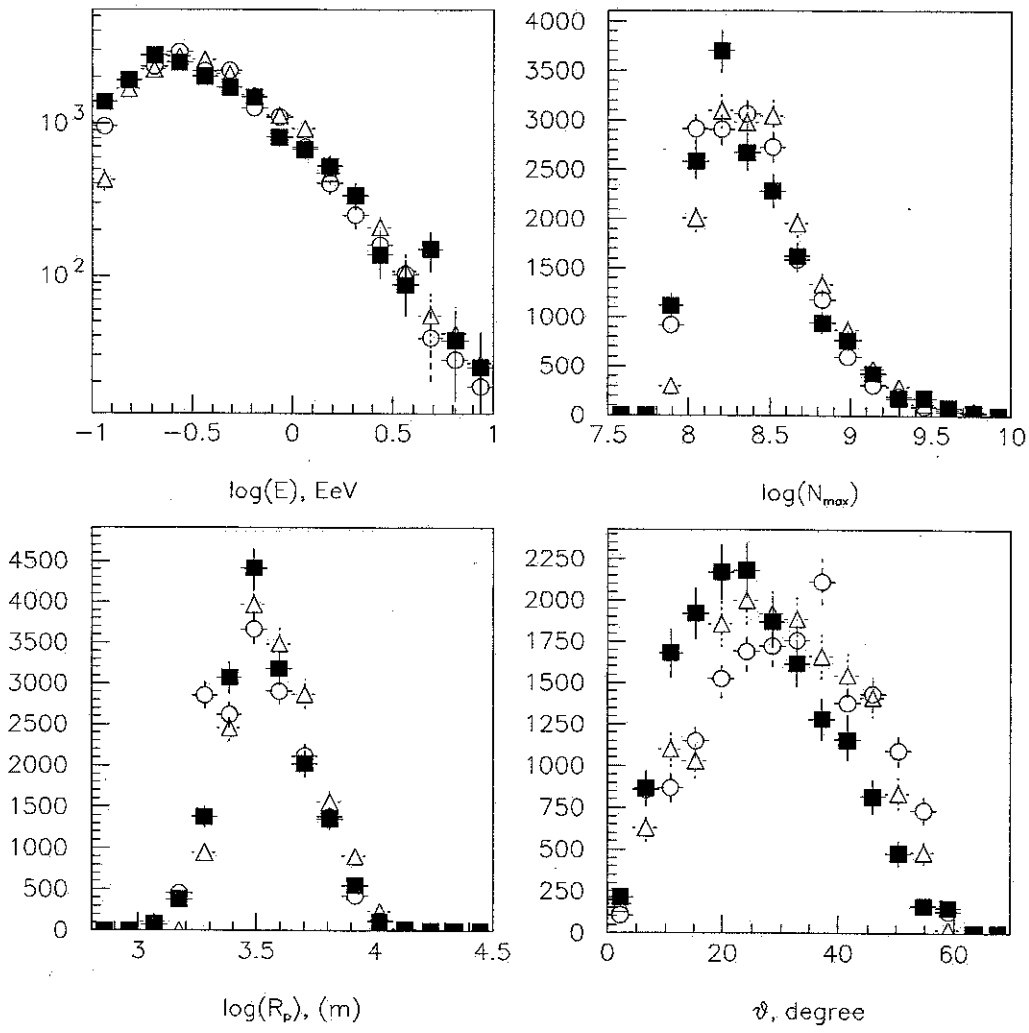

Figure 6.7: The distributions of energy, N_{max}, R_p and zenith angle are compared between experimental data (filled squares) and simulated events for proton (open triangles) and iron (open circles) induced showers.

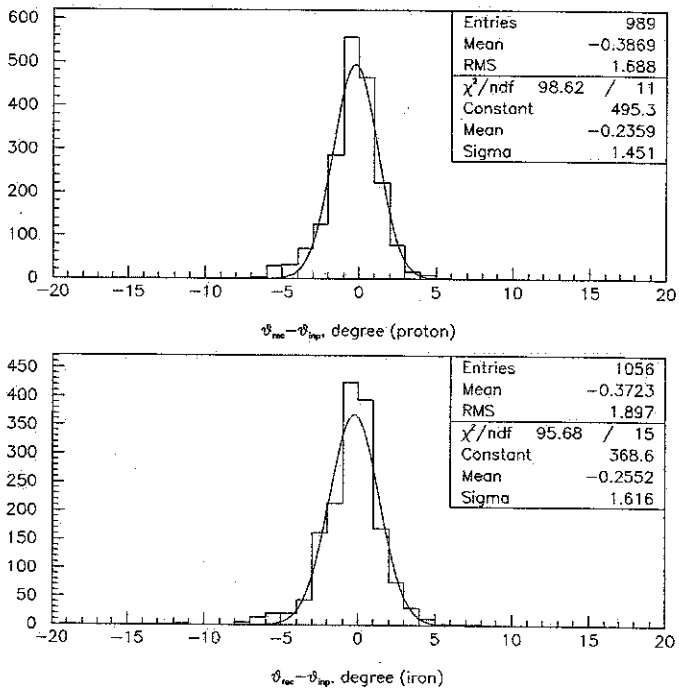

Figure 6.8: The resolution of zenith angle for proton and iron induced showers. $\theta_{\rm inp}$ and $\theta_{\rm rec}$ are the input and reconstructed zenith angle, respectively.

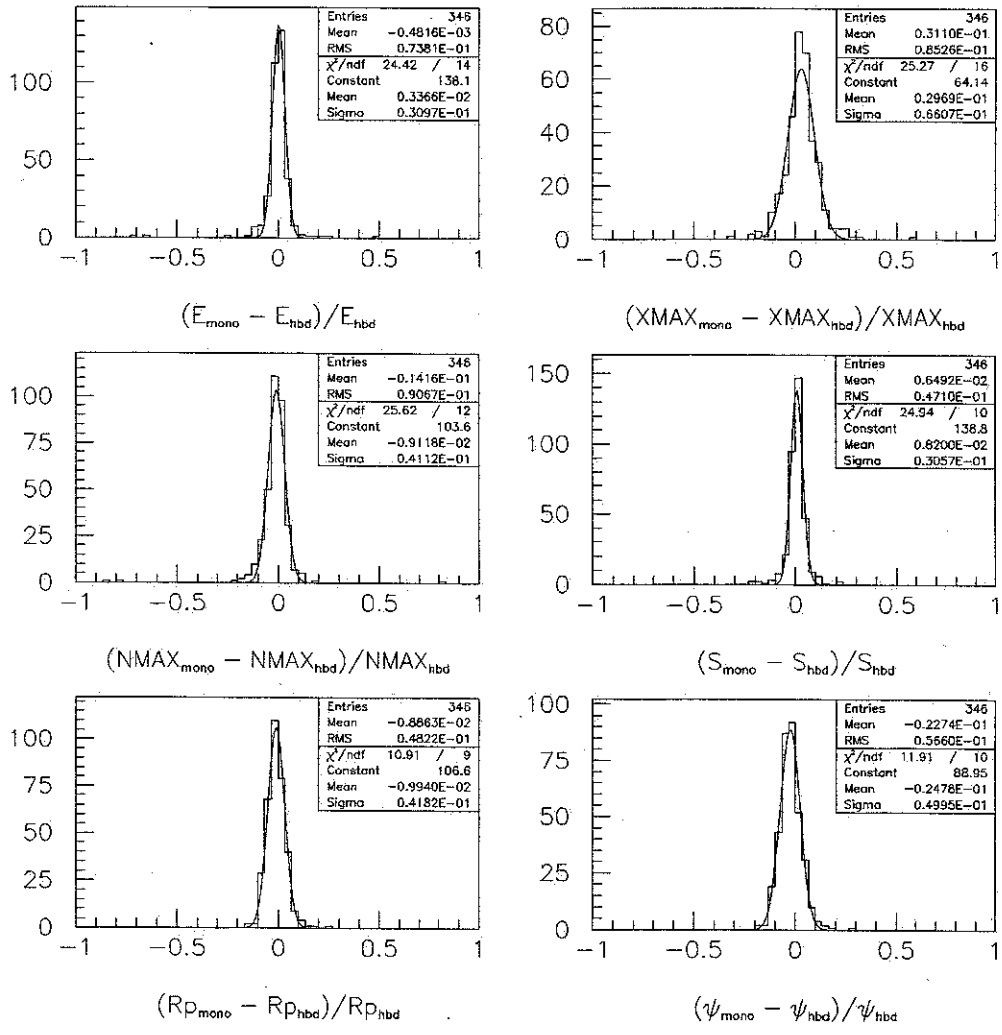

Figure 6.9: The comparison of the reconstructed energy, X_{max}, N_{max}, total tube signal (S), R_p and ψ between hybrid (hbd.) and monocular (mono.) reconstruction methods for 2,881 events triggered by both MIA and HiRes prototype detectors.

the two reconstruction methods for 346 events after applying the cuts to the monocular reconstructed events. The shift in determination of the energy, X_{max} and shower geometry is very small. Both reconstruction methods provide consistent results, but the cuts eliminate many of the monocular reconstructed events.

6.2 Chemical Composition

HiRes observes the longitudinal development of air showers. The mass of the primary particle can be deduced from the longitudinal shower profile by using the fact that showers induced by light nuclei penetrate more deeply into the atmosphere. The distributions of the shower maximum depth for various nuclei are shown in Figure 6.10, based on air shower simulation with CORSIKA. As seen in the figure, it is not possible to determine the primary mass on an event-by-event basis. Thus, the average mass can only be determined from the average shower maximum. Unfortunately, the average shower maximum for a given nucleus depends on the hadronic interaction model. The rate of change of the average shower maximum per logarithmic energy, the so-called 'elongation rate', however, is not sensitive to the model. The elongation rates of proton and iron induced showers between $10^{16.5}$ and 10^{19} eV are 55.4 ± 1.7 and 60.7 ± 0.6 g/cm^2 for QGSJET, and 57.1 ± 1.5 and 60.1 ± 0.6 g/cm^2 for SIBYLL. Figure 6.11 shows the average maximum depths of proton and iron induced showers generated by the parameterization of the QGSJET model in CORSIKA, and they are compared to those of the showers which go through the detector simulation and are reconstructed.

Figure 6.12 shows the average shower maximum as a function of the primary particle's energy. In this figure, the average depths of the shower maximum for proton and iron induced showers generated by full air shower simulation with QGSJET and SIBYLL in CORSIKA are compared. According to this figure, the average mass composition changes from iron-dominated to proton-dominated between $10^{17.0}$ and $10^{17.6}$ eV, after which it is consistently proton-dominated according to the QGSJET model. The ratio of the difference in the average shower maximum between experimental

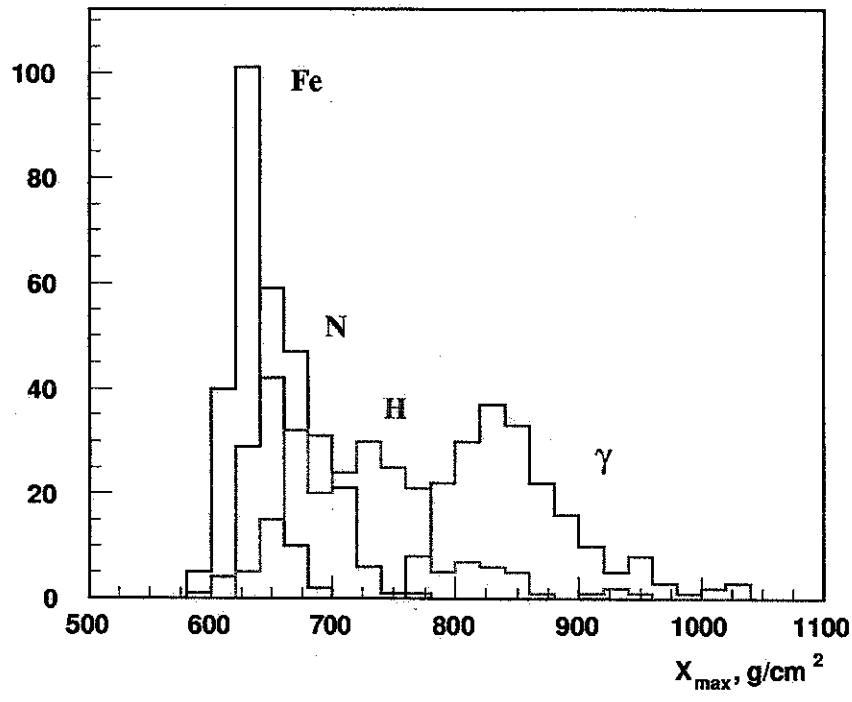

Figure 6.10: The X_{max} distributions of air showers induced by gamma (γ), proton (H), nitrogen (N) and iron (Fe) nuclei. Two hundred events are generated at 10^{18} eV by using CORSIKA with the QGSJET model.

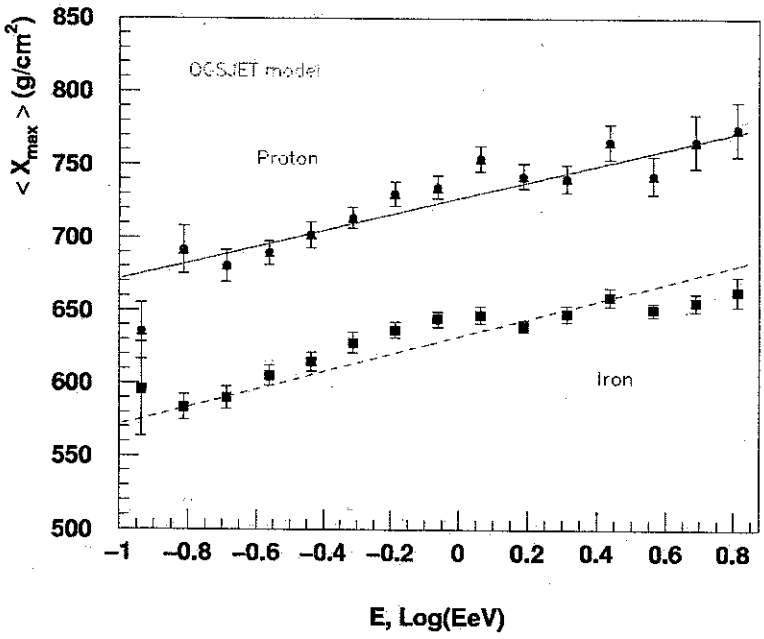

Figure 6.11: The average maximum depths of proton (solid line) and iron (dashed line) induced showers generated by the parameterization of the QGSJET model in CORSIKA are compared to those of the showers which go through the detector simulation and are reconstructed (red triangles for proton and blue squares for iron).

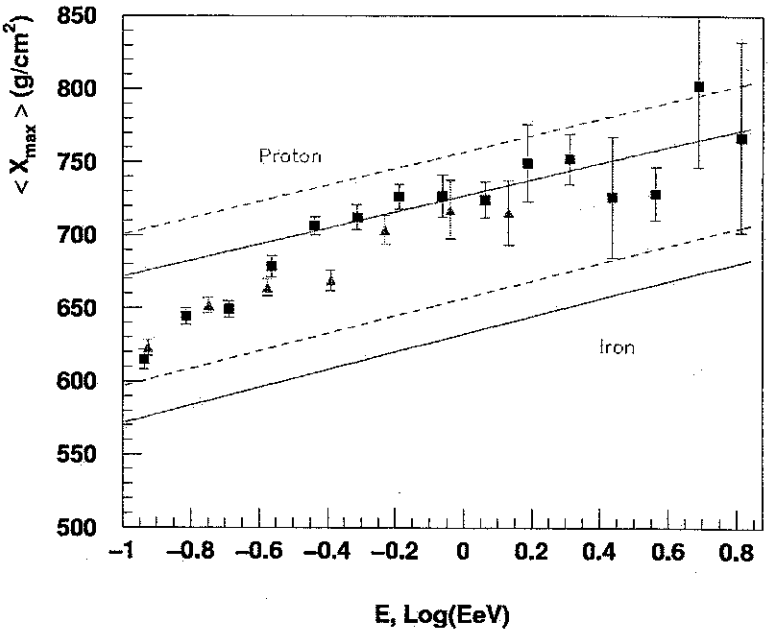

Figure 6.12: The measured average shower maximum (filled squares for the monocular data and filled triangles for the hybrid data) is compared to simulation predictions for proton and iron induced showers. The solid (QGSJET) and dashed (SIBYLL) lines indicate the best fit lines for the simulation. HiRes monocular data clearly indicates that the composition changes from heavy to light nuclei at energies from $10^{17.0}$ to $10^{17.6}$ eV, but does not change above $10^{17.6}$ eV.

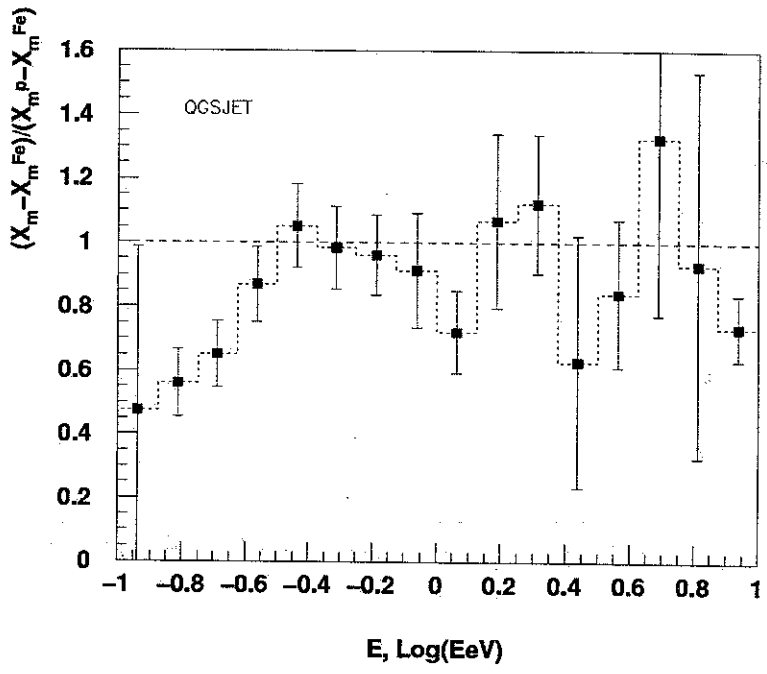

Figure 6.13: The ratio of the difference in the average shower maximum depths (X_m) between data and simulated events to that between simulated proton and iron events. The proton and iron events are generated using the parameterization based on the QGSJET model option in CORSIKA.

data and simulated iron events to that between simulated proton and iron events is shown in Figure 6.13. This figure clearly shows the change in the composition.

When we do a profile fit, all cosmic rays are assumed to be hadronic. If the cosmic rays are electromagnetic, we will overestimate the primary energy and the quality of the profile fit will be poor, because we fixed the X_0 and λ of the Gaisser-Hillas function for hadronic showers.

The Gaisser-Hillas function works well to fit simulated showers. However, in reality, only a small portion of the longitudinal shower profile is usually seen, and experimental data is not as smooth as simulated showers due to night sky noise and the binning procedure. Consequently, the Gaisser-Hillas function may fail to fit shower profiles, which means that parameters of the Gaisser-Hillas function are out of reasonable ranges. For example, λ and $-X_0$ are very large for poorly fitted events. To avoid this problem, we fixed both parameters at $\lambda = 70$ g/cm^2 and $X_0 = -20$ g/cm^2 during profile fits. However, these values represent only the average behavior of the longitudinal shower development. Alternatively, as mentioned in Chapter 4, using a Gaussian function in shower age reduces the number of fitting parameters. In addition, σ of the Gaussian function in age fluctuates less than λ of the Gaisser-Hillas function, as indicated in Table 4.5 and 4.6. Therefore, the Gaussian function in age is preferred to fit experimental data, while the Gaisser-Hillas function describes the longitudinal shower development well based on air shower simulation studies. In fact, a Gaussian function in depth (not in age) was used to fit the shower profiles of the Fly's Eye stereo data. It was claimed that the χ^2 distributions for the Gaisser-Hillas and Gaussian functions in depth are very similar, but the fitting success rate is higher for the Gaussian [149].

6.3 Energy Spectrum

For a detector with a certain efficiency (η), the total number of events in an energy bin ΔE for a given flux ($\vec{J}$) is given by

$$\Delta N_i = \eta T \int_{E_i-\Delta E/2}^{E_i+\Delta E/2} \mathrm{d}E \int \vec{J}(E) \cdot \mathrm{d}\vec{s}\, \mathrm{d}\Omega \tag{6.1}$$

$$\cong \eta T |\vec{J}(E_i)| A\Omega\Delta E, \tag{6.2}$$

where A is the effective core area, T is the exposure time and Ω is given by

$$\Omega = 2\pi \int_0^{\theta_{max}} \cos(\theta)\sin(\theta)\mathrm{d}\theta = \pi \sin^2(\theta_{max}), \tag{6.3}$$

and η is determined by using simulations. For a given aperture ($A\Omega$), η is defined as the ratio of the number of triggered and reconstructible events to the total number of generated events in the detector simulation. The flux is given by

$$J(E) = \frac{\mathrm{d}N/\mathrm{d}E}{\eta A\Omega T}. \tag{6.4}$$

$\mathrm{d}N/\mathrm{d}E$ is replaced with $\mathrm{d}N/\mathrm{dlog}(E)$, because the cosmic ray flux decreases steeply with energy:

$$\mathrm{d}N/\mathrm{d}E = \frac{\log(e)}{E}\, \mathrm{d}N/\mathrm{d}\log(E). \tag{6.5}$$

Therefore, the flux is obtained from the energy distribution:

$$J(E) = \frac{\log(e)}{\eta A\Omega T E}\mathrm{d}N/\mathrm{d}\log(E). \tag{6.6}$$

The flux is determined by dividing the energy distribution by the exposure time (T) and the detector aperture ($\eta A\Omega$).

The total detector run time is 2,370 hours. To determine the detector aperture, the detector simulation is used. As mentioned previously, the scattering of light by aerosols is not certain, so we monitor the atmospheric conditions [123]. However, in the simulation, the average atmospheric condition is assumed for light production and propagation. Based on the atmospheric monitoring, we found the average behavior of the aerosol scattering - 14 km and 1.2 km for the attenuation length (L_M) and scale height (H_M) in Eq. (4.39) and Eq. (4.42). The aperture is shown in Figure 6.14 (b).

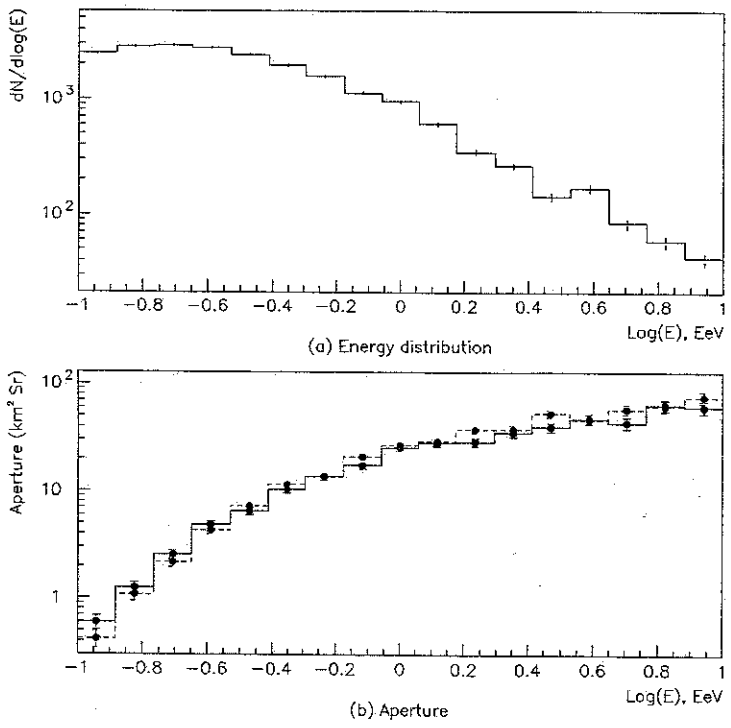

Figure 6.14: (a) Energy distribution after the cuts. (b) Detector aperture as determined by the simulation for proton (solid line) and iron (dashed line) induced showers.

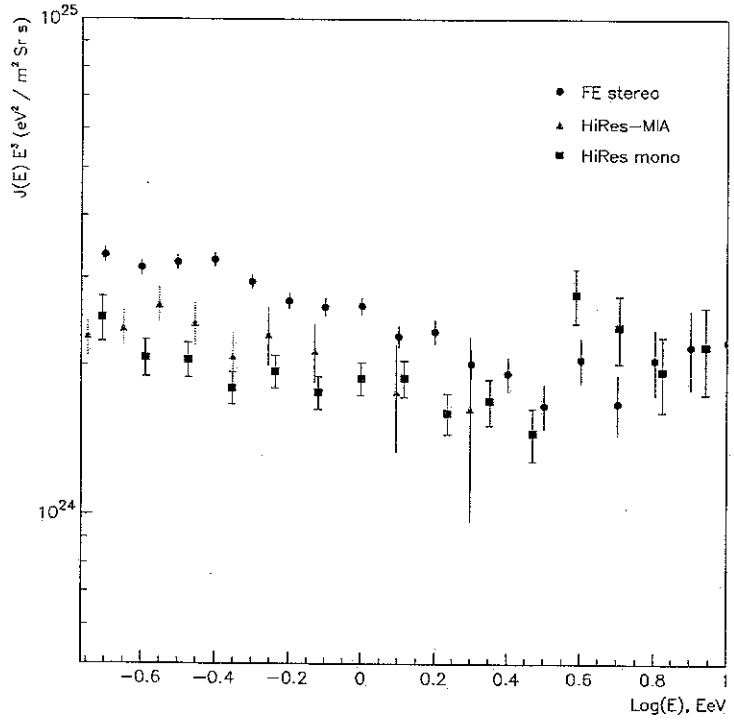

Figure 6.15: The cosmic ray flux is shown at energies between 10^{17} and 10^{19} eV. The average aperture was used to determine the flux. The flux of the HiRes prototype agrees with those of the HiRes-MIA hybrid and the Fly's Eye within the uncertainties. The ankle, a dip in the flux, is also seen.

However, we do not take into account clouds in the simulation. Consequently, we may have slightly overestimated the aperture. According to the trigger rate distribution in Figure 3.11, the average trigger rate for cloudless data is shifted by about 5 % from that for all data. This causes a systematic error in determining the aperture, but the criteria for good weather based on the weather code is subjective. Thus, the cloud coverage needs to be quantitatively estimated, and this can be accomplished with the aid of the cloud detector as described in Chapter 3. Furthermore, we need to study how to apply the information from the cloud detector to the aperture calculation.

By using the average aperture for proton and iron showers, the flux of cosmic rays is determined and shown in Figure 6.15. The flux derived from the HiRes monocular

data agrees with the flux measured by the HiRes-MIA hybrid detector, but is lower than the flux estimated from the Fly's Eye stereo detector at low energies (27 % at 10^{18} eV). However, considering that the energy resolution for the Fly's Eye stereo detector is 24 %, the results agree within the uncertainties.

It is important to note that a very important feature of the cosmic ray spectrum, the dip in the energy spectrum at $10^{18.5}$, is confirmed by this analysis. This so-called 'ankle' was observed by the Fly's Eye experiment at roughly the same energy, and, in addition, has been observed in recent analyses of HiRes monocular data taken with the HiRes-I and HiRes-II detector. The AGASA group has also observed this feature of the spectrum, but the ankle in the AGASA spectrum is at a considerably higher energy, at about $10^{19.01}$ eV [150]. Even assuming that the systematic errors of the HiRes analysis add up to a shift of the energy by 30 %, there is still a factor of 2 discrepancy between the results. This may indicate a severe problem in the energy estimation of either ground arrays or air fluorescence experiments. This discrepancy will likely be resolved by the Pierre Auger Observatory which comprises fluorescent light detectors and a Cherenkov water tank array. Note that this uncertainty in the energy estimation has severe consequences for the number of events measured above the GZK cutoff and may account for the striking difference in the number of GZK events as seen by HiRes and AGASA [151].

Chapter 7

COMPOSITION ABOVE THE ANKLE

It is difficult to explain ultra high energy cosmic rays within conventional models since it is difficult for protons and heavy nuclei to be accelerated up to 100 EeV even in the most powerful astrophysical objects. In addition, nucleons above 50 EeV lose energy drastically due to photo-pion production ($p\gamma_b \rightarrow p\pi^o$) on the cosmic microwave background.

In this chapter, I will study in more detail the possibility that cosmic rays with energies above the ankle are gamma rays. Most of the so-called top-down models for cosmic ray production predict such high energy gamma rays, so a more detailed study of the composition above the ankle may indeed help to discriminate between top-down and the more conventional bottom-up scenarios.

As mentioned earlier, additional effects like the LPM effect and interactions of gamma rays with the geomagnetic field have to be taken into account. I will briefly describe the changes to the simulation made necessary by these effects, and then present first results for the HiRes-I monocular data.

7.1 Gamma Ray Flux

According to Sangjin Lee [152], it was incorrectly claimed that the ultra high energy photons lose energy very fast based on the fact that the mean free path of the ultra

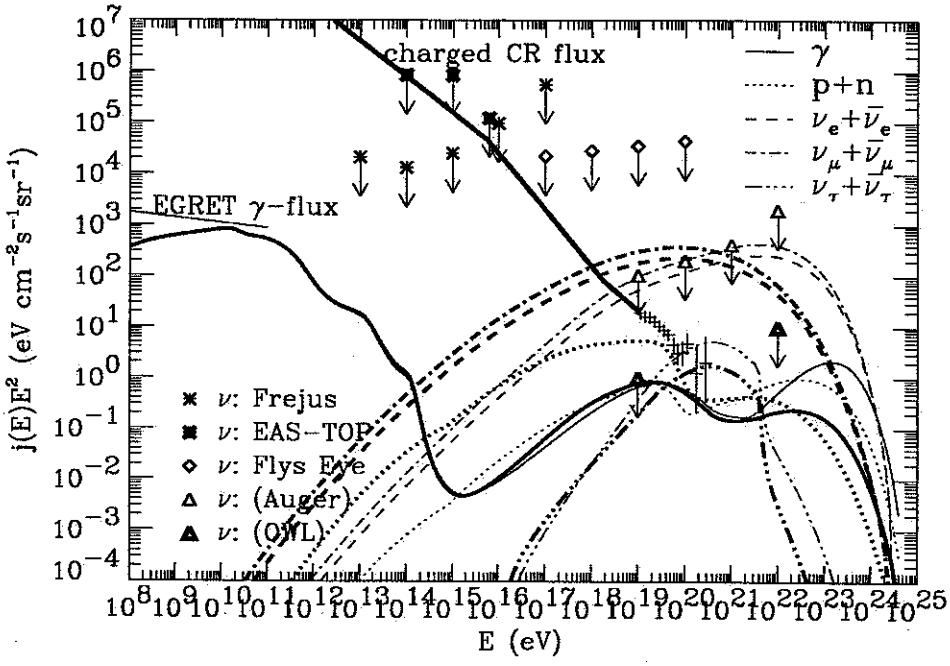

Figure 7.1: Energy spectra of nucleons, neutrinos and gamma rays for the 'top-down' model with $m_X = 10^{16}$ GeV, $\mathrm{d}n_X/\mathrm{d}t \propto t^{-3}$ and the decay mode $X \to q + q$, assuming the high universal radio background version [153, 154] and an extra-galactic magnetic field of 10^{-10} G [155]. Thick and thin lines represent SUSY and no-SUSY fragmentation functions, respectively [156].

high energy photon is fairly short. In fact, the sequence of pair production and inverse Compton scattering makes the actual energy attenuation much slower. In the extreme Klein-Nishima limit ($s \gg m_e^2$), one of the particles produced in an electron-positron pair production carries almost all of the initial energy and the produced electron undergoes inverse Compton scattering. In this high energy limit, the inelasticity for inverse Compton scattering is more than 90 %, so the electron loses most of its energy to the background photon. As a consequence, the up-scattered photon carries almost all of the energy of the initial photon. As a result, the predicted flux of ultra high energy photons can be much larger than the one calculated by considering only the absorption length of ultra high energy photons due to pair production. However, this process can be suppressed by synchrotron radiation with the extragalactic magnetic field.

Figure 7.1 shows the energy spectra of nucleons, gamma rays and neutrinos for 'top-down' models with likely parameters [156]. The injection rate of X particles of mass m_X is assumed to be spatially uniform and can be parameterized as $\mathrm{d}n_X/\mathrm{d}t \propto t^{-4+p}$, where p is a dimensionless constant. Two major uncertainties come from the intensity and spectrum of the universal radio background and the average value of the extragalactic magnetic field. For most combinations of likely values for these astrophysical parameters and the energy scale of new physics, there are possible decay modes and fragmentation functions that lead to scenarios that explain the UHECRs above the GZK cut-off.

7.2 Geomagnetic Field

Both primary and secondary charged particles in air showers are deflected by the geomagnetic field. Furthermore, if the energies are high enough for magnetic pair production and magnetic bremsstrahlung, the electromagnetic cascade can be initiated before reaching the top of the atmosphere. We will study this phenomenon.

The earth's magnetic field is - to some accuracy - that of a spherical magnet. The axis of the magnetic dipole is off by 10° from that of the earth's rotation. The current location of the surveyed magnetic north pole is 78.5 N and 103.4 W. The opening angle between magnetic and geological north is about 14° at Dugway, Utah. The intensity of the earth's magnetic field is roughly between 25 and 65 μT. However, the geomagnetic field is constantly changing. By using the International Geomagnetic Reference Field (IGRF) model [129], the intensity of the magnetic field can be calculated for a given location and time.

7.3 Electromagnetic Cascades in Magnetic Field

If ultra high energy gamma rays exist, it is possible that they convert into electron-positron pairs in the geomagnetic field before reaching the top of the atmosphere. The produced electrons emit photons. As a result, there are many secondary photons

and electrons instead of the primary photon and the longitudinal development of air shower will be shrunk. The electromagnetic conversion processes are well described by Erber [157]. We consider magnetic bremsstrahlung (synchrotron radiation) and magnetic pair production in the simulation, but we do not consider trident cascades, photon splitting or magnetic Cherenkov radiation as described in [157].

7.3.1 Magnetic Bremsstrahlung

Electrons orbiting in strong magnetic fields radiate photons. Similarly, high energy electrons radiate photons in weak magnetic fields. This magnetic bremsstrahlung is characterized in terms of Υ, defined as

$$\Upsilon \equiv \frac{E}{mc^2}\frac{H}{H_{cr}}, \tag{7.1}$$

where E is the initial energy of electron, H is the ambient magnetic field strength, m is the rest mass of the electron and H_{cr} is defined as

$$H_{cr} = m^2c^3/e\hbar = 4.414 \cdot 10^{13}\ \text{G}. \tag{7.2}$$

The spectral distribution of the radiation emitted per unit length is given by

$$I(E,\omega,H) = \frac{\sqrt{3}\alpha}{2\pi}\frac{mc^2}{\lambda_e}\frac{\Upsilon}{E}\Big(1-\frac{\omega}{E}\Big)\xi\int_{\xi}^{\infty} \mathrm{d}x K_{5/3}(x), \tag{7.3}$$

where λ_e is the Compton wavelength of the electron, ω is the energy of the emitted photon, $K_{5/3}$ is the modified Bessel function and ξ is

$$\xi = \frac{2}{3\Upsilon}\frac{\omega}{E}\left(1-\frac{\omega}{E}\right)^{-1}. \tag{7.4}$$

Unlike the Bethe-Heitler formula, there is no infrared divergence. The radiation length is given by

$$L_e = \frac{1}{\int_0^E I(E,\omega,H)\ \mathrm{d}\omega}. \tag{7.5}$$

The radiation length of electrons at three different energies is shown in Figure 7.2.

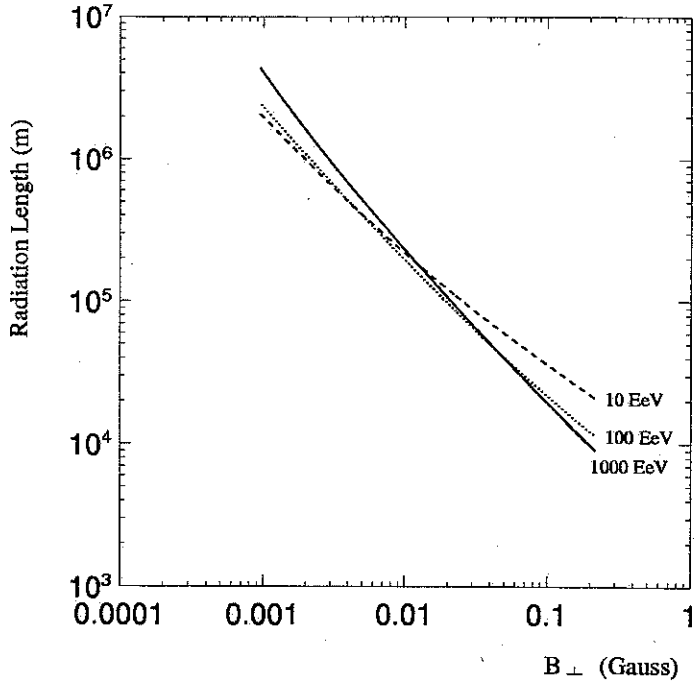

Figure 7.2: Radiation length of electrons as a function of the perpendicular component of the magnetic field at three different energies.

The differential probability per unit length for magnetic bremsstrahlung is given independently by Bayer [158]:

$$\pi(E,\omega,H) = \frac{\alpha}{\pi\sqrt{3}}\frac{m^2c^4}{E^2}\left[\left(\frac{E-\omega}{E}+\frac{E}{E-\omega}\right)K_{2/3}\left(\frac{2u}{3\Upsilon}\right) - \int_{\frac{2u}{3\Upsilon}}^{\infty} K_{1/3}(y)\,\mathrm{d}y\right], \quad (7.6)$$

where $u = \omega/(E-\omega)$. The free path of electrons is the inverse value of the total probability:

$$L_e' = \frac{1}{\int_0^E \pi(E,\omega,H)\,\mathrm{d}\omega}. \quad (7.7)$$

Both equations (7.5) and (7.7) give identical results [159].

7.3.2 Magnetic Pair Production

We define χ, which plays a role analogous to the parameter Υ in bremsstrahlung, as:

$$\chi \equiv \frac{\omega}{mc^2}\frac{H}{H_{cr}}, \tag{7.8}$$

where ω is the initial energy of the photon. The attenuation coefficient (1/attenuation length) is expressed in the form

$$\alpha(\chi) = \frac{1}{2}\frac{\alpha}{\lambda_e}\frac{H}{H_{cr}}T(\chi), \tag{7.9}$$

where the dimensionless $T(\chi)$ is given by

$$\begin{aligned} T(\chi) = \frac{16}{3\pi^2\chi^2}\int_0^\infty \int_0^\infty du dw \\ \Big[(2\cosh^2 w \cosh^5 u - \sinh^2 u \cosh^3 u) K_{1/3}^2\left(\frac{4}{3\chi}\cosh^2 w \cosh^3 u\right) \\ +(2\cosh^2 w - 1)\cosh^5 u \; K_{2/3}^2\left(\frac{4}{3\chi}\cosh^2 w \cosh^3 u\right)\Big], \end{aligned} \tag{7.10}$$

where $K_{1/3}$ and $K_{2/3}$ are modified Bessel functions. However, as pointed out by Vankov [160], Table VI in [157] provides wrong $T(\chi)$ values. Thus, we recalculate $T(\chi)$ numerically without any approximation. Figure 7.3 shows the attenuation coefficient of gammas as a function of the perpendicular component of the magnetic field.

The differential probability per unit length for magnetic pair production is given by Bayer [158]:

$$\gamma(\omega, E, H) = \frac{\alpha}{\pi\sqrt{3}}\frac{m^2c^4}{E}\left[\left(\frac{\omega - E}{E} + \frac{E}{\omega - E}\right) K_{2/3}\left(\frac{2v}{3\chi}\right) - \int_{\frac{2v}{3\chi}}^\infty K_{1/3}(y)\, dy\right], \tag{7.11}$$

where $v = \omega^2/E(\omega - E)$. The free path of photons is the inverse value of the total probability:

$$L_\gamma = \frac{1}{\int_0^\omega \gamma(\omega, E, H)\, dE}. \tag{7.12}$$

Both methods give the same results as those for bremsstrahlung. The ratio of electron energy to gamma energy in magnetic pair production for various χs is shown in Figure 7.4.

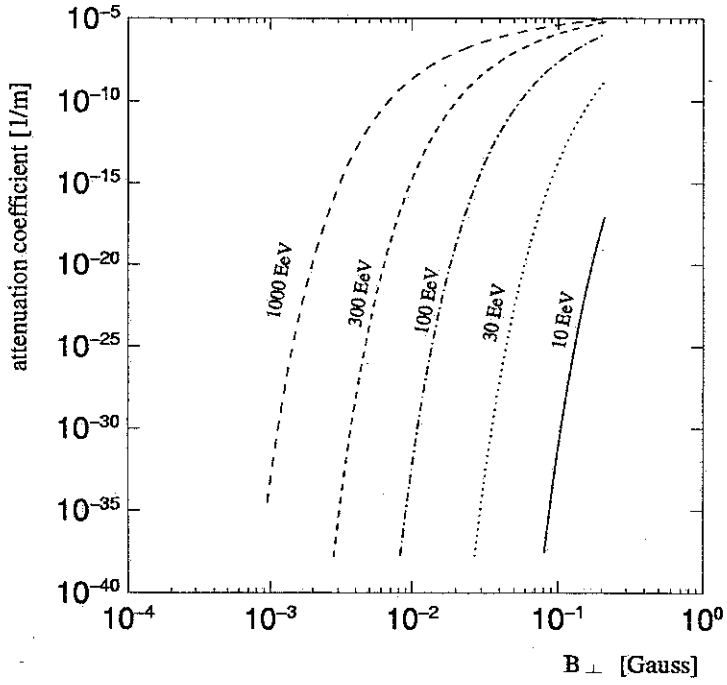

Figure 7.3: Attenuation coefficient of gammas as a function of the perpendicular component of the magnetic field for several energies of gamma rays.

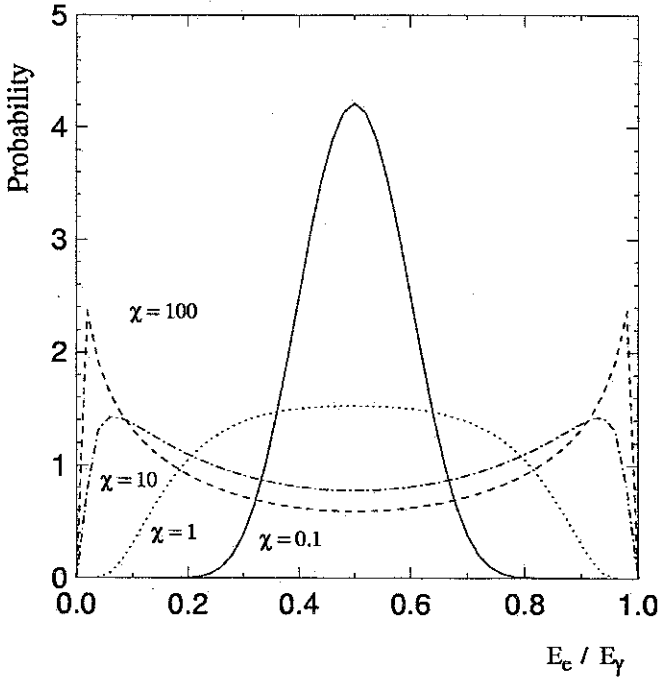

Figure 7.4: Ratios of electron energy to gamma energy in magnetic pair production for various χs.

7.4 Simulation

In the ultra-relativistic limit, the scattering angle is approximately 0°. Thus, we consider the electromagnetic cascade in one dimension. The detector is located at 248° W, 40° N and 1,957 m above sea level. The geometry used in our simulation is shown in Figure 7.5. We adopted the IGRF model [129] to describe the magnetic field of the earth. Figure 7.6 shows the perpendicular component of the geomagnetic field as a function of the distance from the center of the earth for different zenith angles. The ultra high energy gamma ray reaches the detector from $10 \times R_{\oplus}$ away. The mean free path is calculated in every step, which is 10 km for gammas and 1 km for electrons. Within the step, the magnetic field is assumed to be constant and calculated using the IGRF model.

These processes stop at the top of the atmosphere (50 km above sea level) and compete with atmospheric interactions down to 20 km using the air shower simulation code AIRES. Within the competition region, the free paths of electrons or photons for atmospheric and magnetic interactions are calculated and the interaction with the shorter path is selected for further development. Figure 7.7 shows the scatter plot of the free paths of electrons for atmospheric and magnetic interactions in a 10^{20} eV gamma ray induced shower. Figure 7.8 shows that the atmospheric interaction is dominant in the competition region except at very high altitudes. As the energy of the gamma ray increases, we can expect more magnetic interactions. The atmospheric interaction is dominant below 20 km.

The additional gamma ray interactions are incorporated into AIRES instead of CORSIKA, as CORSIKA does not enable us to simulate air showers above 10^{20} eV and does not consider the curvature of the earth's surface. Moreover, AIRES adapts a more realistic geomagnetic field model, IGRF. Within AIRES, the QGSJET model is chosen for high energy hadronic interactions. The threshold kinetic energies of electrons, photons and muons are 0.2, 0.2, 1 MeV, respectively. The LPM effect is enabled.

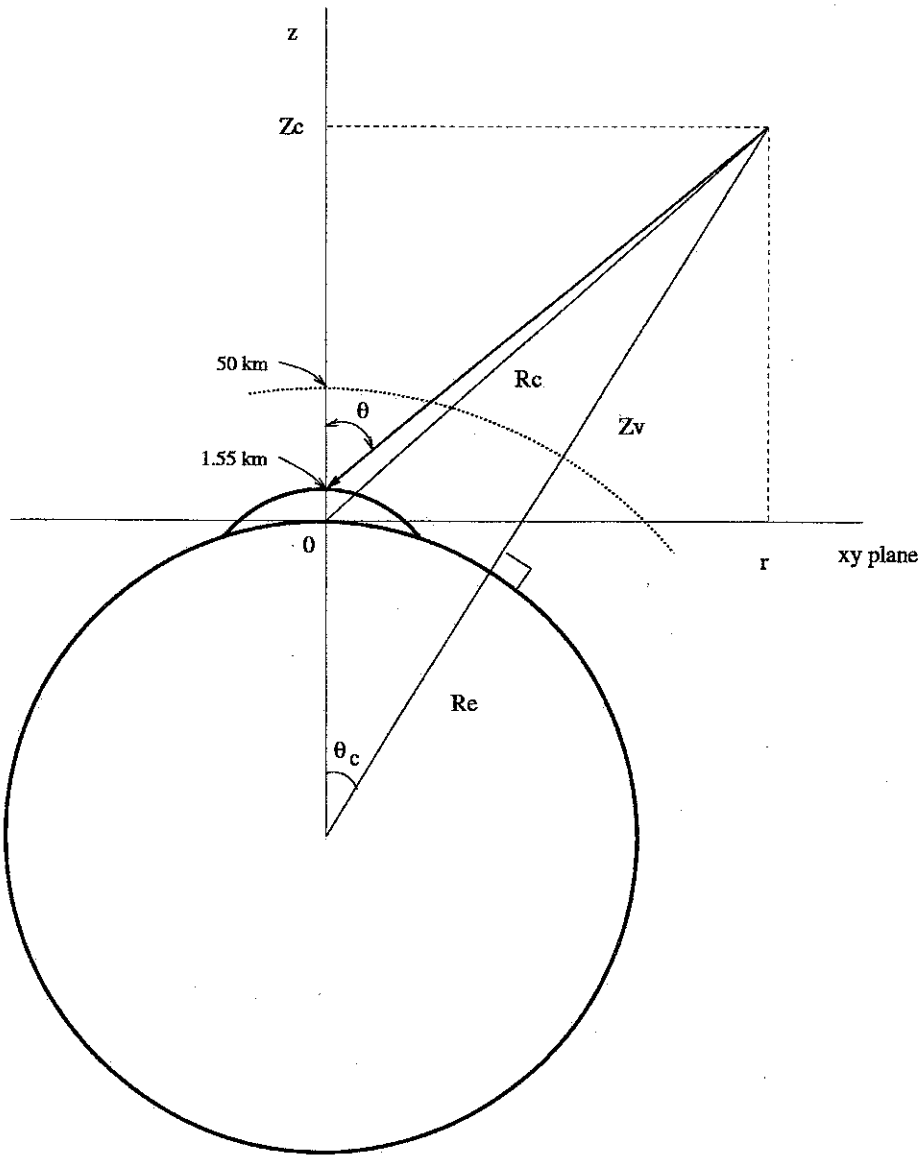

Figure 7.5: Coordinate system used in the simulation of ultra high energy gamma rays.

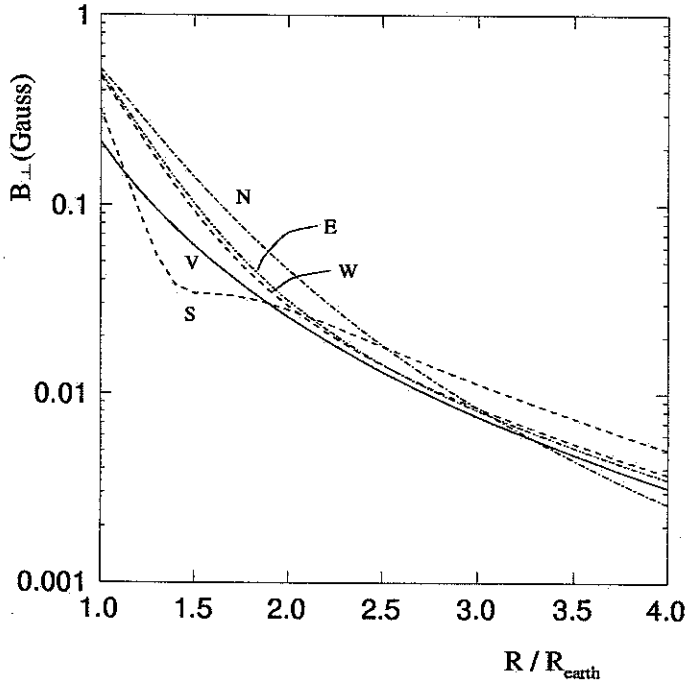

Figure 7.6: Perpendicular component of the geomagnetic field as a function of distance from the center of the earth for various incident directions: vertical direction (V), north (N), south (S), east (E) and west (W) with a zenith angle of 45°.

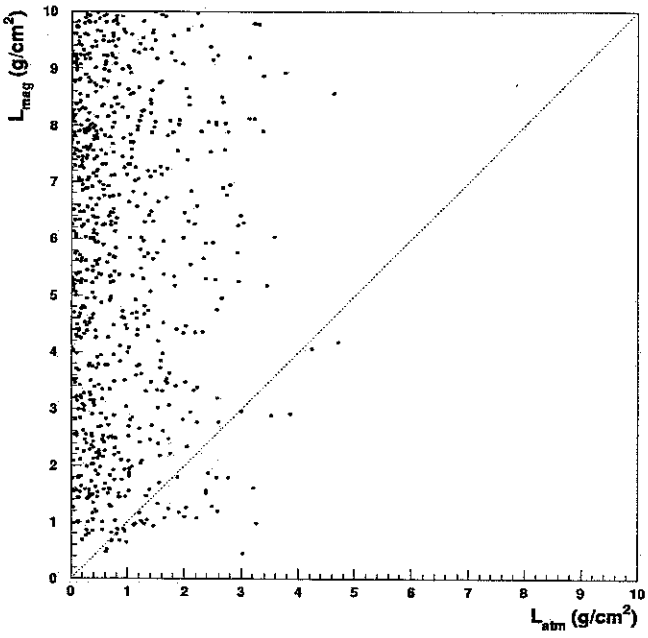

Figure 7.7: Free paths of electrons for atmospheric and magnetic interactions within the competition region (20 - 50 km) for a 10^{20} eV gamma ray at a fixed incident angle $\theta = 55°$, $\phi = 76°$.

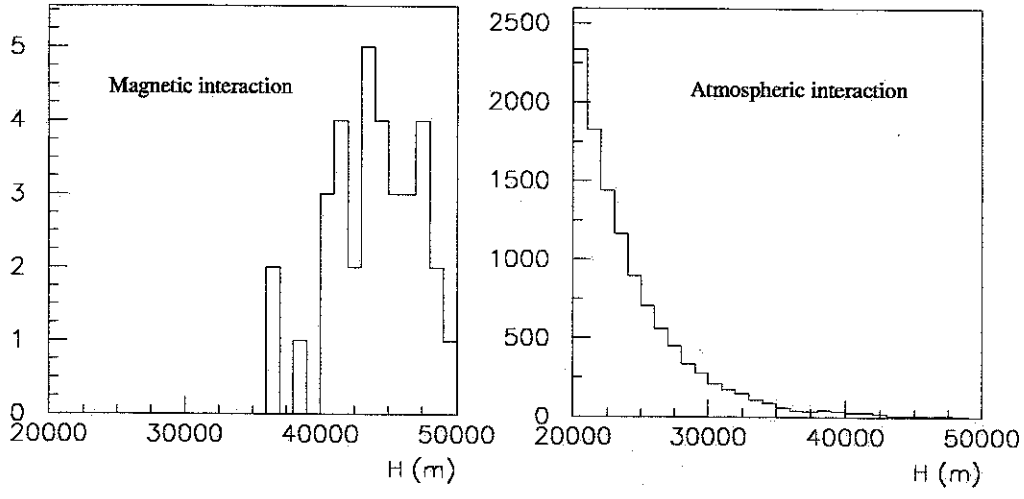

Figure 7.8: Interaction height distribution for electrons: the atmospheric interaction is dominant in the competition region except at very high altitude. As the energy of the gamma ray increases, we can expect more magnetic interactions.

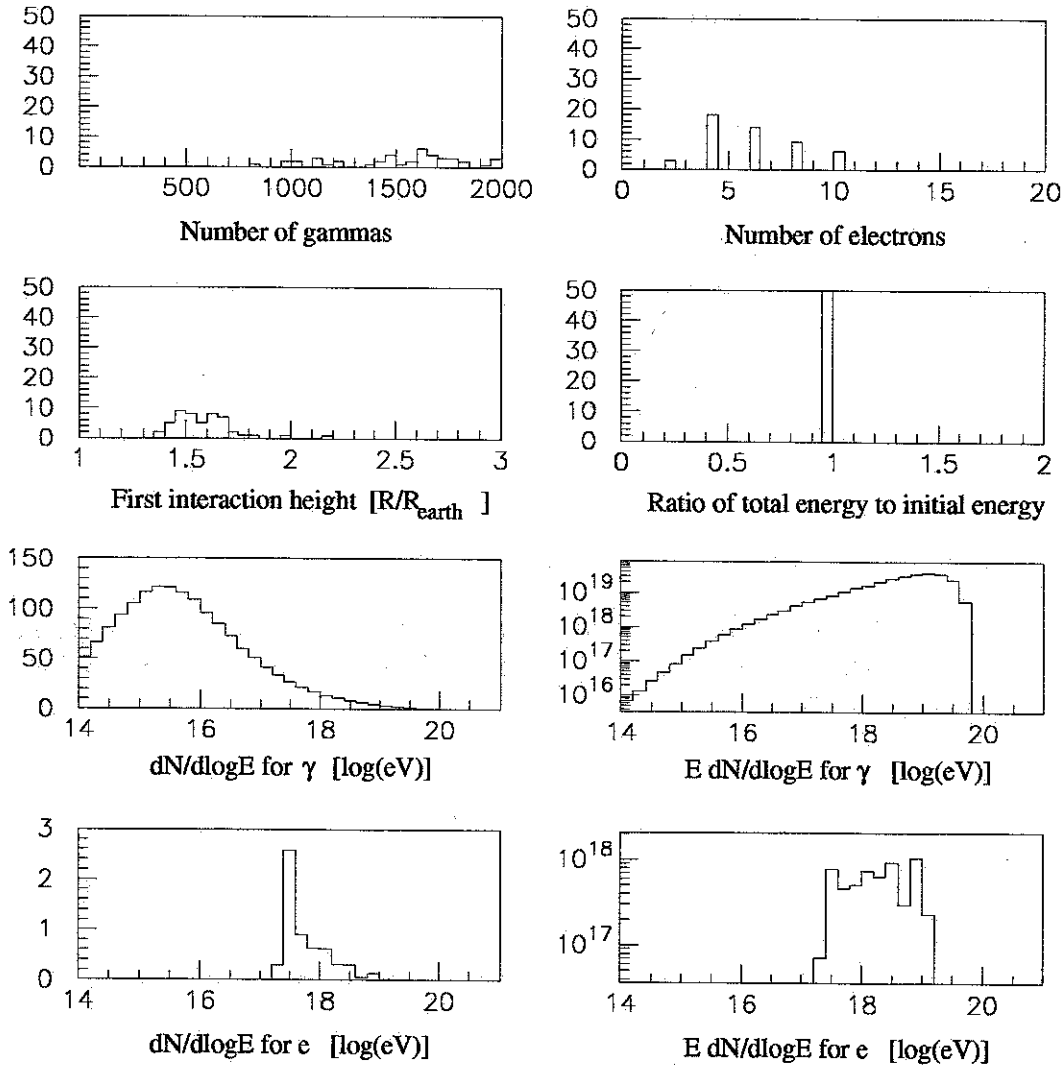

Figure 7.9: For $10^{20.5}$ eV gamma rays coming from the north with a zenith angle of 45°, the number and energy distributions of electrons and photons are shown. The distribution of the first interaction height from the center of the earth is shown in units of the earth's radius.

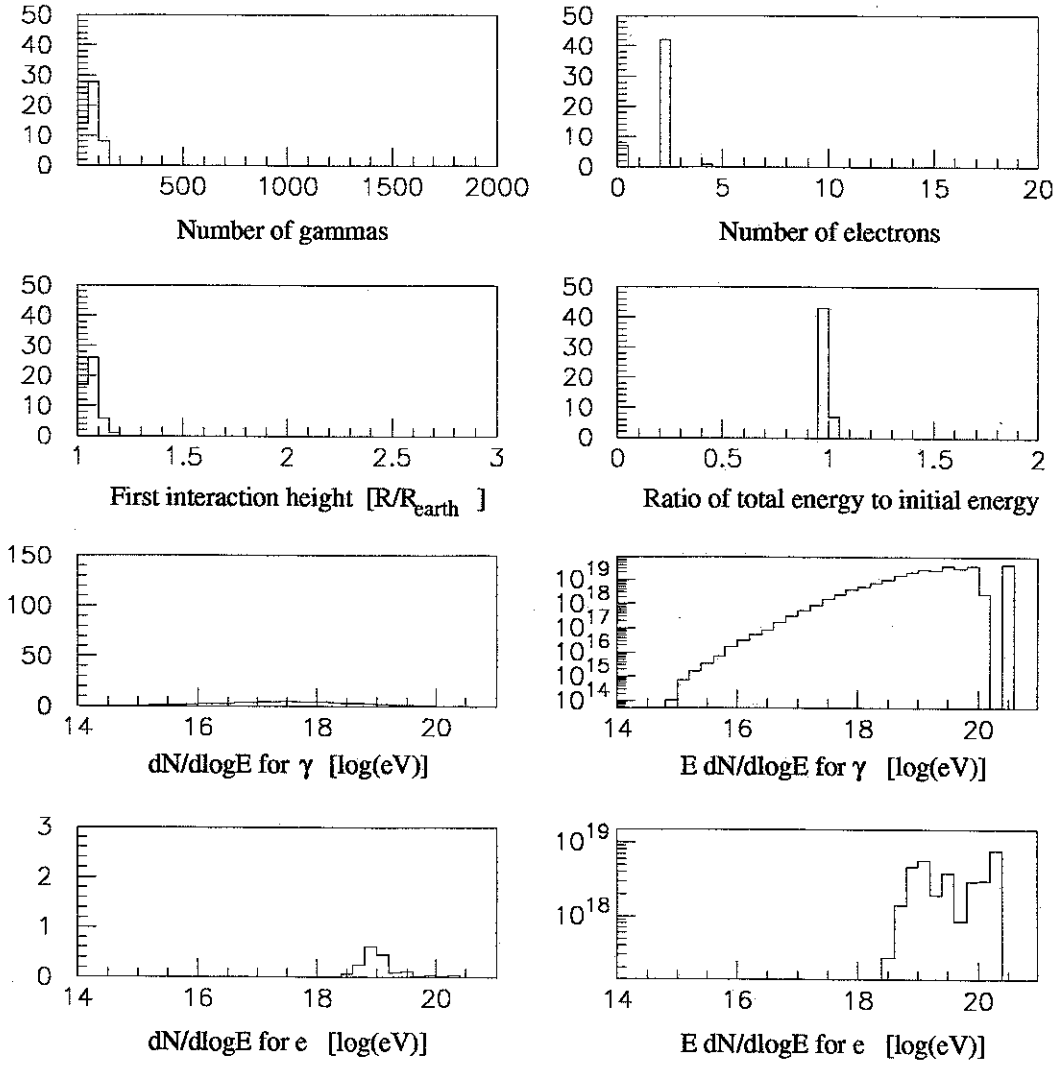

Figure 7.10: For $10^{20.5}$ eV gamma rays coming from the south with a zenith angle of 45°, the number and energy distributions of electrons and photons are shown. The distribution of the first interaction height from the center of the earth is shown in units of the earth's radius.

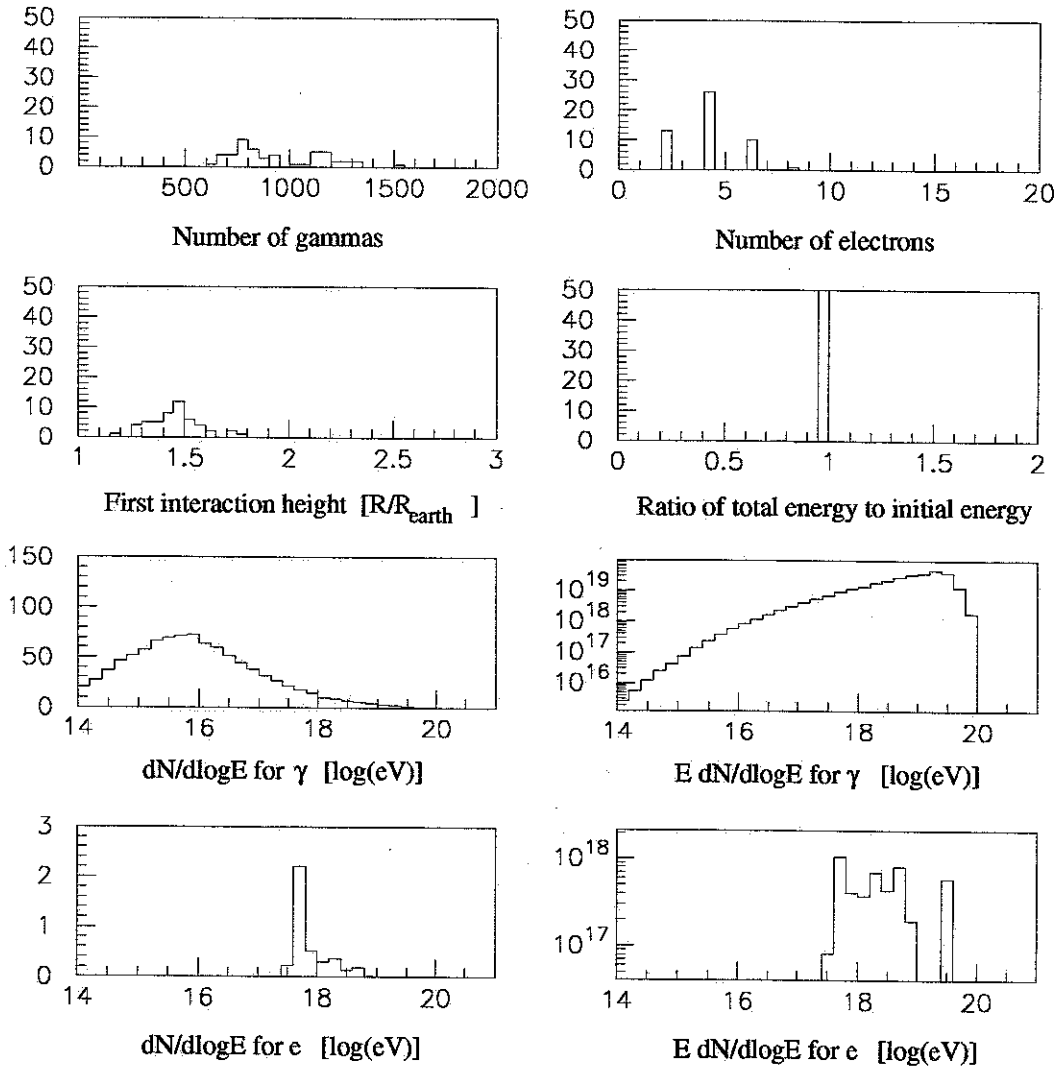

Figure 7.11: For $10^{20.5}$ eV gamma rays coming from the east with a zenith angle of 45°, the number and energy distributions of electrons and photons are shown. The distribution of the first interaction height from the center of the earth is shown in units of the earth's radius.

Figure 7.9, 7.10 and 7.11 show the results of the simulation. At 50 km, a $10^{20.5}$ eV gamma ray comes from the north, east and south with a zenith angle of 45°. The gamma ray from the north experiences a much stronger magnetic field than the gamma ray from the south. More gammas are produced than electrons because the mean free path of magnetic pair production is much longer than the radiation length of magnetic bremsstrahlung. The energy is conserved throughout the simulation.

Figure 7.12 shows the first interaction distributions of ultra high energy gammas. We see a window in the southern sky. Figures 7.13 and 7.14 show the distribution of the number of electrons and photons at 50 km. Figure 7.15 shows the average X_{max} as a function of primary energy for protons, iron nuclei and gamma rays at various zenith angles. Between $10^{19.5}$ to 10^{20} eV, we see the largest difference in the average X_{max} of gamma showers between north and south. Figure 7.16 shows the X_{max} distribution induced by ultra high energy gamma rays at four different energies. In this figure, the X_{max} distribution is different for showers from north and south. By using this so-called north-south effect, we may see the signature of ultra high energy gamma rays.

7.5 Search for Ultra High Energy Gamma Rays

The north-south effect is maximized for energies between $10^{19.5}$ and 10^{20} eV as indicated in Figure 7.15. To search for ultra high energy gamma rays in HiRes data, we focus on this energy range. For better statistics within the energy range, we collect events from a wide azimuthal angle. Events coming between $-60°$ and $60°$ of geomagnetic north in azimuthal angle are defined as coming from the north, and these events experience a strong magnetic field. For events from the south, we choose $-15°$ to $15°$ of geomagnetic south. The simulation results are shown in Figure 7.17 and 7.18, which show zenith angle and X_{max} distributions for gamma rays coming from north and south. In the simulation, 3,000 events are generated for two different energy regions, assuming that the flux of cosmic rays is proportional to E^{-3}. The gamma induced showers coming from south penetrate deeply so that the shower maximum

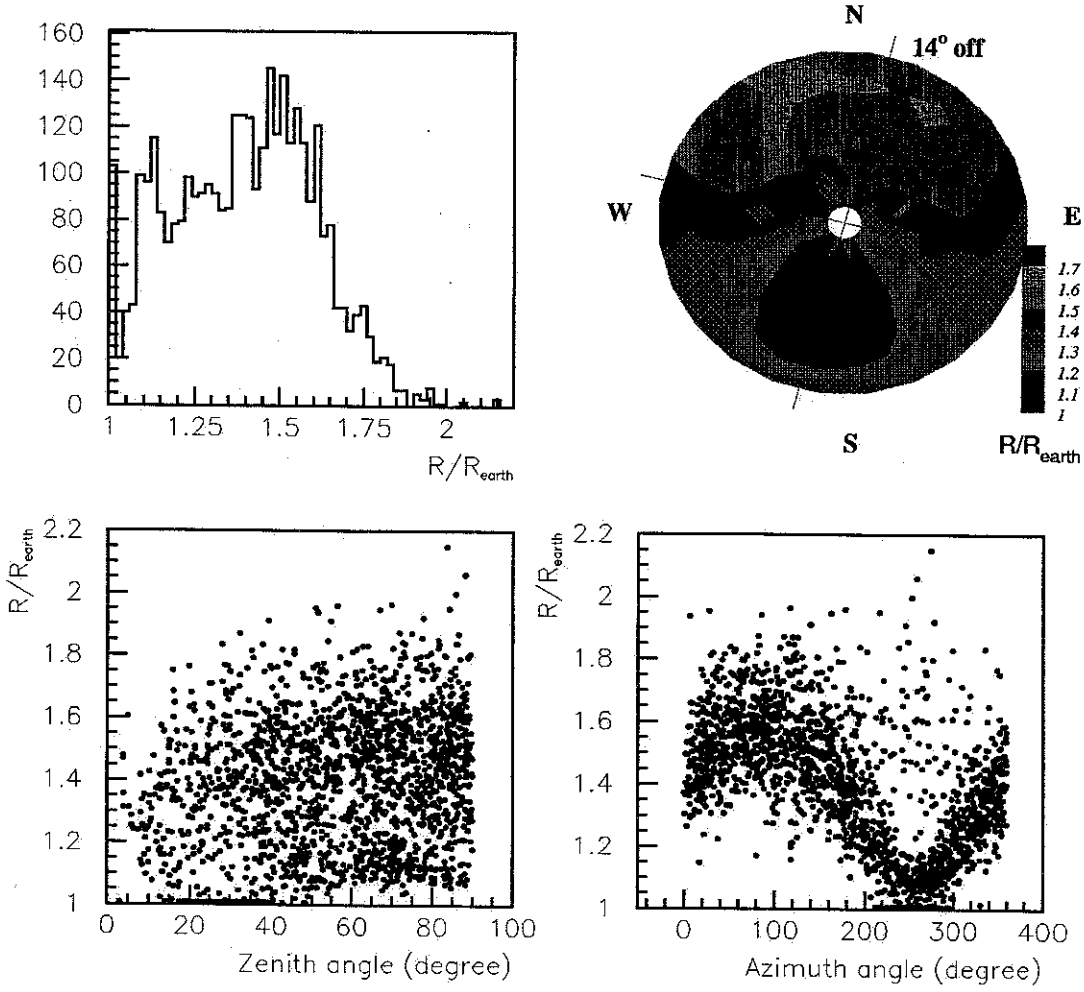

Figure 7.12: First interaction height R of ultra high energy gamma rays in units of the earth's radius R_{earth} for 1,500 events with random incident angles. The primary energy is $10^{20.5}$ eV. The first interaction height is shown with zenith and azimuth angles.

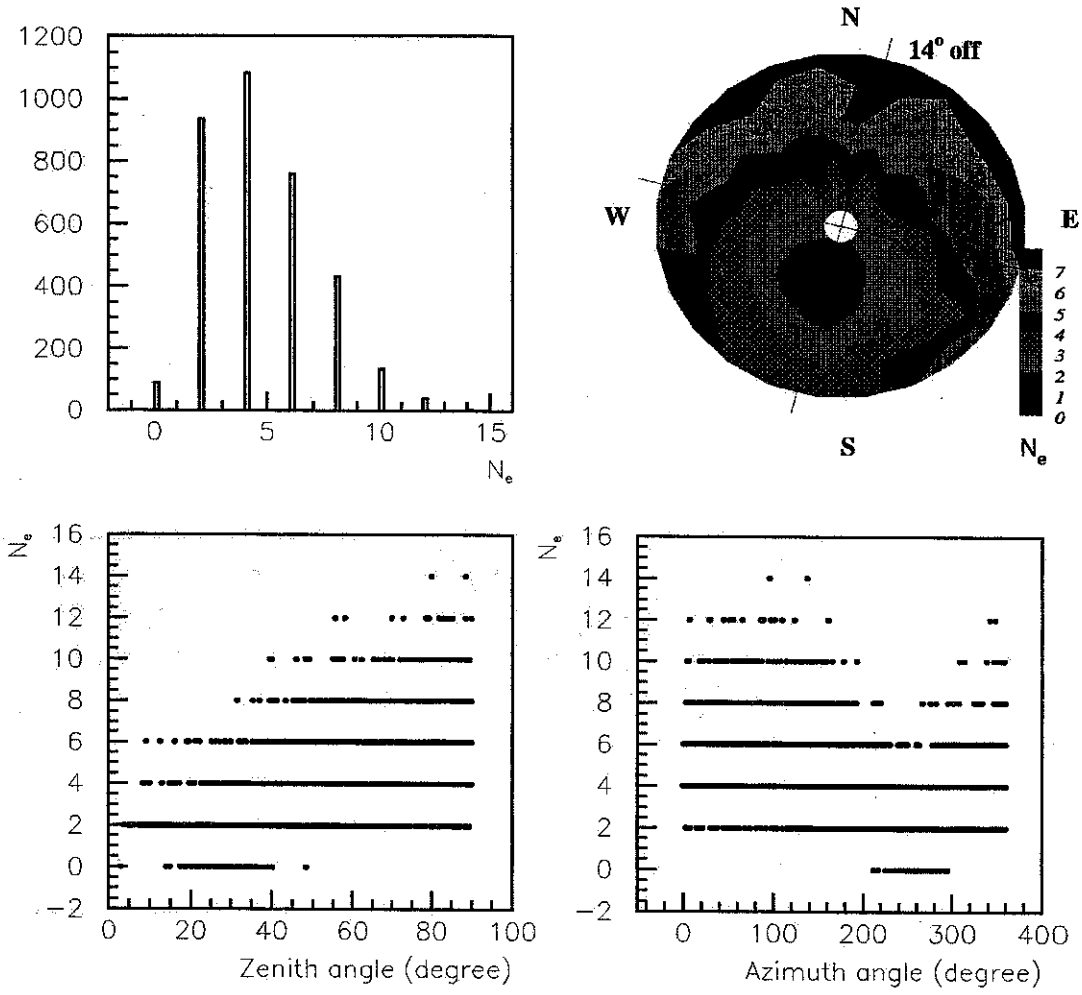

Figure 7.13: The number of secondary electrons induced by ultra high energy gamma rays at 50 km. The primary energy is $10^{20.5}$ eV. The number of secondary electrons is shown with zenith and azimuth angles.

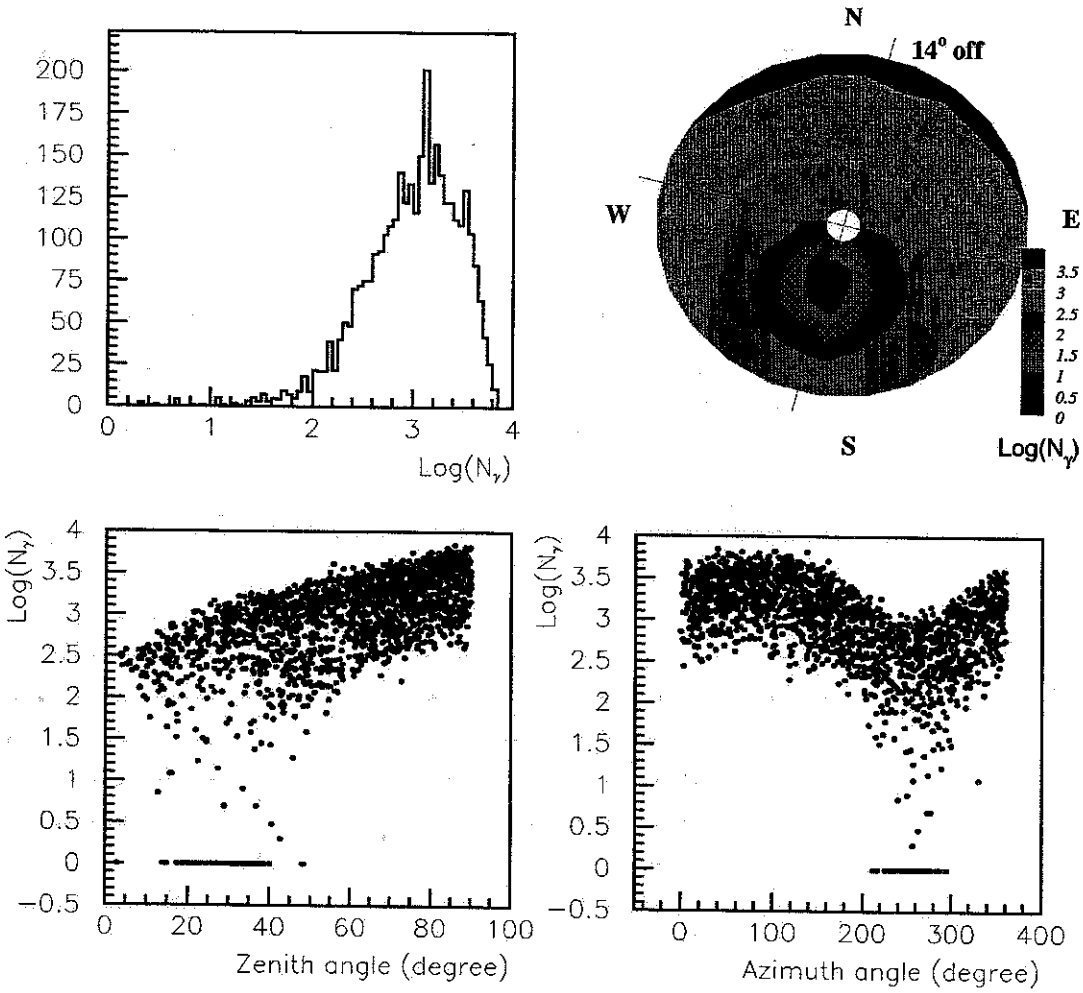

Figure 7.14: The number of secondary photons induced by ultra high energy gamma rays at 50 km. The primary energy is $10^{20.5}$ eV. The number of secondary photons is shown with zenith and azimuth angles.

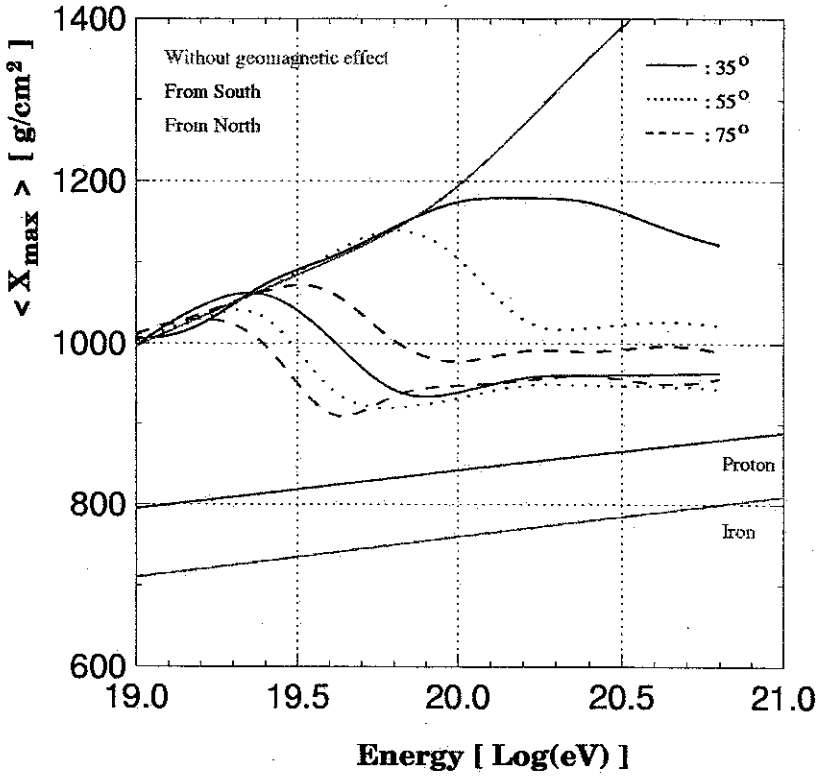

Figure 7.15: Average shower maximum as a function of the primary energy for gamma induced showers coming from north and south at three different zenith angles. The average shower maxima for protons, iron nuclei and gamma rays without geomagnetic effect are also shown.

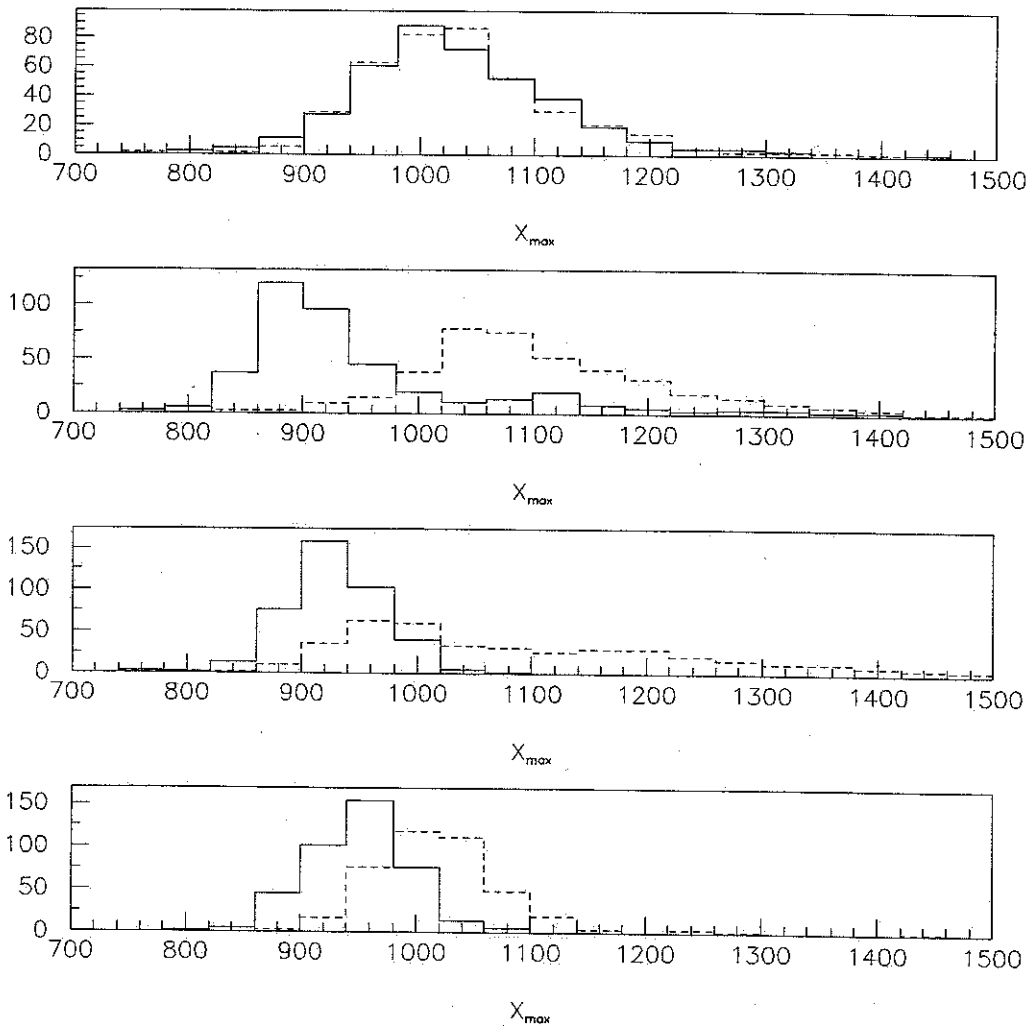

Figure 7.16: Comparison of X_{max} distributions for gamma rays coming from north (solid lines) and south (dashed lines) at $10^{19.2}$, $10^{19.6}$, $10^{20.0}$ and $10^{20.4}$ eV. The zenith angle is 55°.

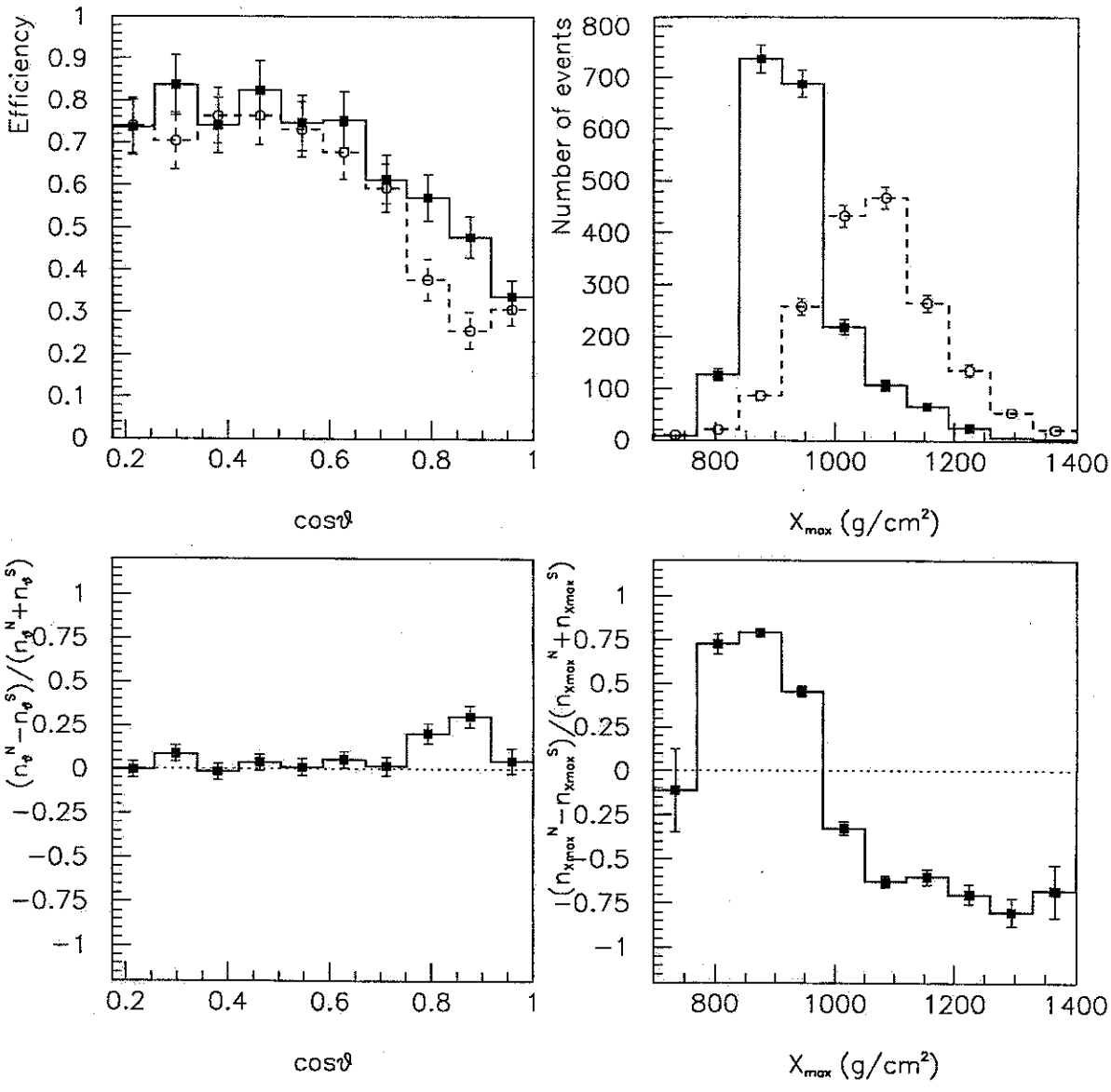

Figure 7.17: The upper plots show zenith angle and X_{max} distributions for gamma rays coming from north (closed squares) and south (open circles) regions defined in the text. In the simulation, 3,000 events are generated at energies between $10^{19.5}$ and 10^{20} eV assuming that the flux of cosmic rays is proportional to E^{-3}. The distributions of the ratio of the difference in the number of events from north and south over the sum of all events for zenith angle and X_{max} are shown in the lower plots.

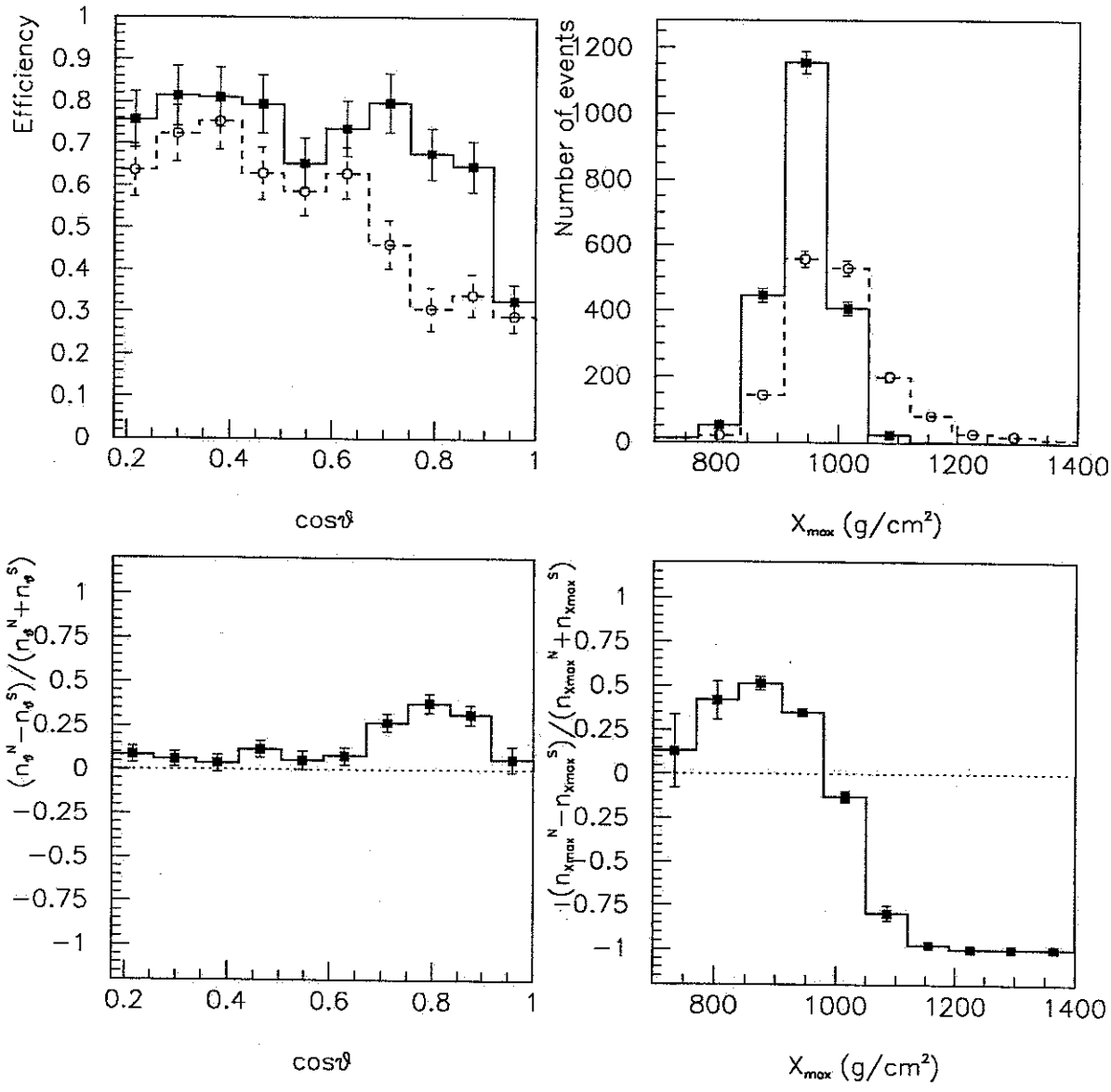

Figure 7.18: The upper plots show zenith angle and X_{max} distributions for gamma rays coming from north (closed squares) and south (open circles) regions defined in the text. In the simulation, 3,000 events are generated at energies between 10^{20} and $10^{20.5}$ eV assuming that the flux of cosmic rays is proportional to E^{-3}. The distributions of the ratio of the difference in the number of events from north and south over the sum of all events for zenith angle and X_{max} are shown in the lower plots.

can be deeper than the depth of the observation site. As shown in the figures, the number of reconstructible events is different for the two regions. More events coming from south are not reconstructible. The largest difference in the zenith angle distributions appears between 20° and 40°. Comparing the X_{max} distributions for north and south, we also see the signature of ultra high energy gamma rays.

Unfortunately, the HiRes prototype detector does not cover this energy region. Thus, we turn to the HiRes-I monocular data reconstructed by Abu-Zayyad [117]. However, the study of the detector simulation for HiRes-I shows that the reconstruction of the shower axis works poorly because of the short track length of the air showers (the track lengths of the HiRes-I monocular data are mostly less than 15°). Thus, Abu-Zayyad invented the 'profile constrained geometry fit'. In this profile fit, χ^2 is minimized with several fixed shower maximum depths chosen from a reasonable range based on air shower simulations.

To search for ultra high energy gamma rays, the zenith angle distribution is used instead of X_{max}, because a small shift in the determination of the shower axis can give quite different X_{max} and because good angular resolution is not required for this study. Figure 7.19 shows the zenith angle distributions for different energy bins. We see a difference in the zenith angle distribution. Figure 7.20 shows a scatter plot of the zenith and azimuth angles for events at the same energy region. However, the effect is statistically insignificant. This technique will help to identify the nature of the particle type. In addition to studies of the isotropy or anisotropy of the arrival direction, this method will make the HiRes stereo detector a powerful tool for discriminating between various models of cosmic ray production.

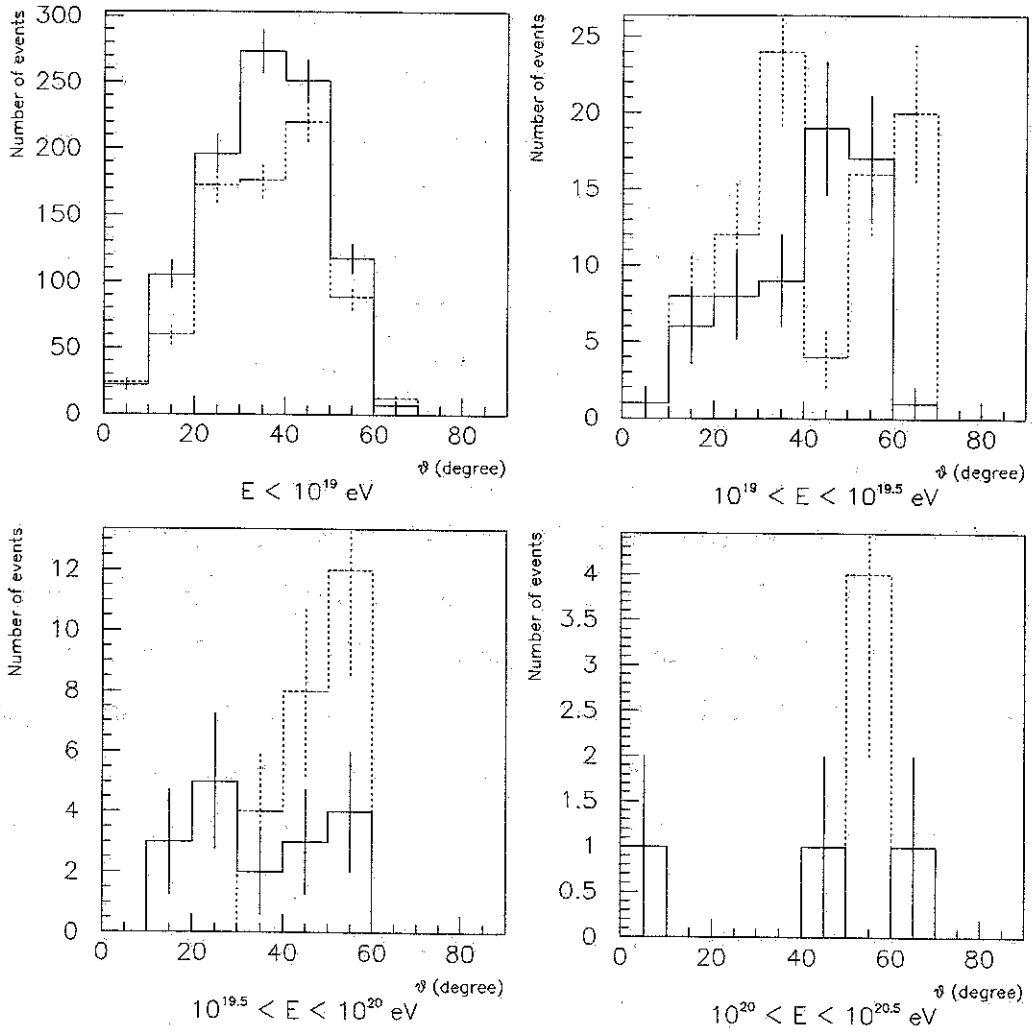

Figure 7.19: Zenith angle distributions for events coming from north (solid line) and south (dashed line) at different energy bins.

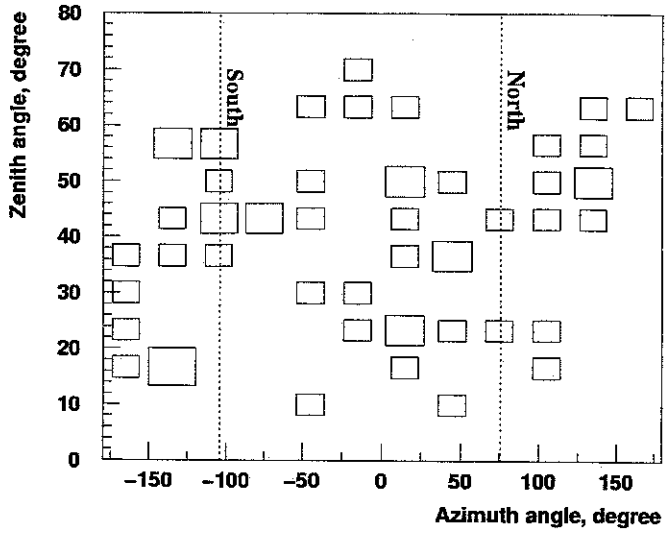

Figure 7.20: Zenith angle versus azimuth angle for events of energies between $10^{19.5}$ and 10^{20} eV. The dotted lines represent the directions of magnetic north and south.

Chapter 8

CONCLUSION

8.1 Air Shower Simulations

Above 10^{16} eV, the energy of primary cosmic ray particles cannot be measured directly. In HiRes, the atmosphere is a calorimeter, and the calorimetric energy is determined by integrating the longitudinal shower profile. In this thesis, the energy determination of cosmic rays is investigated with the air shower simulation code CORSIKA. The technique provides a good estimate of the primary energy for electromagnetic showers. For hadronic showers, I have derived a correction function which accounts for unseen energy such as high energy muons, neutrinos and nuclear excitation.

To generate more realistic air showers in our detector simulation, I parameterized longitudinal shower profiles between $10^{16.5}$ and 10^{20} eV with CORSIKA. When we implant shower parameterizations into our detector simulation, the threshold effect should be taken into account very carefully. In the simulation, particles below the threshold energies are not considered. Thus, we should account for the particles below the thresholds by raising the shower size by 11.1 %. The reconstructed energy was shown to be consistent with the input energy without going through the detector. Various distributions between experimental data and simulated events are compared. The comparison shows that our treatments for detector and atmosphere are appropriate.

The shower profile has to be fitted for energy reconstruction. Using a Gaussian

function in age rather than a Gaisser-Hillas function reduces the number of fitting parameters. The parameter σ of the Gaussian function in age fluctuates less than the parameter λ of the Gaisser-Hillas function. Both functions give comparable χ^2 where the shower sizes are greater than 10^{-2} times the maximum shower size (N_{max}), although the Gaussian function does not fit the profile at the early stage of the shower. Moreover, both functions give consistent values for X_{max}, N_{max} and the energy for simulated showers. Therefore, a Gaussian function in age is used for the reconstruction of experimental data.

8.2 Composition and Flux at $10^{17} - 10^{19}$ eV

Events triggered by both the MIA and HiRes prototype detectors are reconstructed using the information from the HiRes detector only and from both HiRes and MIA. In comparison with the hybrid reconstruction, the monocular reconstruction works equally well. One advantage of HiRes monocular data is that it provides about ten times more events than the hybrid data. However, the number of events is drastically reduced after applying the cuts, and this enables us to obtain resolution comparable to that of the hybrid data.

To determine the flux of cosmic rays, the aperture was determined with the detector simulation. By using the average aperture for proton and iron induced showers, the flux of cosmic rays is determined. The flux of the HiRes prototype monocular data agrees with that of the HiRes-MIA hybrid but is lower than that of the Fly's Eye stereo at low energies (27 % at 10^{18} eV). Considering that the energy resolution for the Fly's Eye stereo detector is 24 %, the results agree within the uncertainties. Cloud coverage in the sky may cause a systematic error in determining the aperture. The quantitative estimate of the cloud coverage can be accomplished with the aid of the cloud detector. Furthermore, we need to study how to apply the information from the cloud detector to the aperture calculation.

By determining the shower maximum, the change of the average mass composition was determined. The interpretation of the absolute composition depends on the

hadronic interaction model used in the analysis. However, we clearly see that the composition changes from heavy to light at energies between 10^{17} and $10^{17.6}$ eV and that the average composition is constant above $10^{17.6}$ eV. Above the ankle, it is more difficult to deduce the composition from the shower maximum depth because as energy increases, air showers penetrate more deeply and the chance to observe the shower maximum depths decreases. Thus, a new method of composition study above the ankle was proposed.

8.3 Composition above 10^{19} eV

Cosmic rays at these energies are hardly accelerated in conventional bottom-up models. Nucleons above 50 EeV lose energy drastically due to photo-pion production ($p\gamma_b \rightarrow p\pi^o$) on the cosmic microwave background. This limits the distance of possible astrophysical sources to around 50 Mpc. The galaxy M87 in the Virgo cluster is a possible source for cosmic rays above 50 EeV. At these energies, the deflection in extragalactic magnetic field is small ($< 1°$), so these particles should point back to their sources. But experimental data at these energies is too limited to allow for conclusions. Alternatively, top-down models predicted a flux of gammas or neutrinos. The break in the energy spectrum known as the ankle can be interpreted as evidence of a new source of cosmic rays. The present study investigated the possibility that cosmic rays with energies above the ankle are gamma rays.

A method for identifying such high energy gamma rays is proposed based on the simulation study. We simulated gamma ray showers, factoring in the earth's magnetic field. Both geomagnetic and LPM effects are effective at energies above 10^{19} eV. The longitudinal shower development is influenced differently depending on the arrival direction of the incident particle due to the inhomogeneous magnetic field. If the primary particles are gamma rays, the simulation study suggests that the difference in shower maximum will be maximized between incident directions of north and south at the energy range of $10^{19.5}$ to 10^{20} eV.

Comparison with the experimental data did show a slight difference at this energy

range. Nonetheless, present evidence that cosmic rays are gamma rays is limited by the insufficient experimental data from the HiRes-I monocular detector. In future studies, however, we can predict that the signature of ultra high energy gamma rays will be seen in data from the HiRes stereo detector, from which shower geometry can be more accurately reconstructed.

Appendix A

$G(s)$, $\Phi(s)$ and $\xi(s)$ in Migdal Theory

The functions $G(s)$ and $\Phi(s)$ are given by [82]:

$$G(s) = 48s^2\left(\frac{\pi}{4} - \frac{1}{2}\int_0^\infty e^{-st}\frac{\sin(st)}{\sinh(t/2)}\mathrm{d}t\right), \tag{8.1}$$

and

$$\phi(s) = 12s^2\int_0^\infty e^{-st}\cosh(t/2)\sin(st)\mathrm{d}t - 6\pi s^2. \tag{8.2}$$

These two functions are plotted in Figure 8.1.

$\xi(s)$ is given by

$$\xi(s) = \begin{cases} 2 & : \text{ if } s < s_1, \\ 1 + \ln(s)/\ln(s_1) & : \text{ if } s_1 \le s \le 1, \\ 1 & : \text{ if } s > 1, \end{cases} \tag{8.3}$$

where $s_1 = Z^{2/3}/184^2$ and r_e is the classical electron radius. For $s \geq 1$, there is no suppression and the Migdal theory yields a result identical to the Bethe-Heitler cross-section. However, the suppression becomes important when s approaches 0.

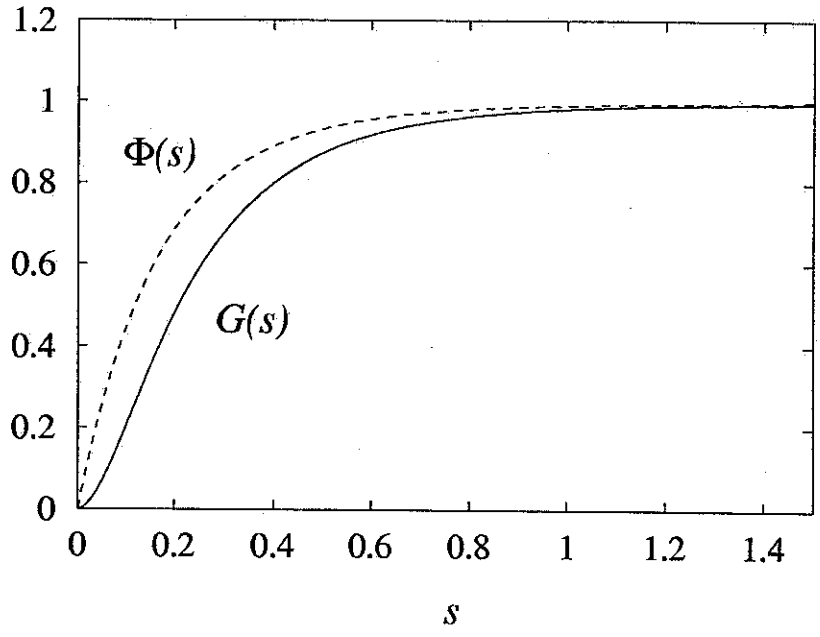

Figure 8.1: Functions $G(s)$ and $\Phi(s)$ in Migdal theory are shown.

Bibliography

[1] N. Hayashida, *et al.*, *Phys. Rev. Lett.* **73**, 3491 (1994).

[2] M. A. Lawrence, R. J. O. Reid and A. A. Watson, *J. Phys. G: Nucl. Part. Phys.* **17**, 733 (1991).

[3] T. A. Egorov, "Recent Results from Yakutsk Experiment", *Proc. Tokyo Workshop on Techniques for the Study of Extremely High Energy Cosmic rays*, Tokyo, Japan, 35 (1993).

[4] C. D. Anderson, *Science* **76**, 238 (1932).

[5] S. H. Neddermeyer and C. D. Anderson, *Phys. Rev.* **51**, 884 (1937).

[6] G. D. Rochester and C. C. Butler, *Nature* **160**, 855 (1947).

[7] R. Armenteros, *et al.*, *Phil. Mag.* **43**, 597 (1952).

[8] A. Bonetti, R. Levi-Setti, M. Panetti, G. Tomasini, *Nuovo Cim* **10**, 345 (1953).

[9] M. S. Longair, "High Energy Astrophysics", Vol. 1, (Cambridge University Press, 1994).

[10] C. T. R. Wilson, *Phyl. Trans. Royal Soc.* **189**, 265 (1897).

[11] V. Hess, *Phys. Z.* **13**, 1084 (1912).

[12] W. Kolhörster, *Ber. Deutsch. Phys. Ges.* **16**, 719 (1914).

[13] P. Auger, R. Maze, and Grivet-Meyer, *C. R. Acad. Sci.*, Paris, **206**, 1721 (1938).

[14] J. Linsley, *Phys. Rev. Lett.* **10**, 146 (1963).

[15] D. J. Bird *et al.*, *Ap. J.* **424**, 491 (1994).

[16] J. R. Hörandel, *et al.*, *Proc. 26th ICRC*, Salt Lake City, USA, **1**, 337 (1999).

[17] K. Greisen, *Phys. Rev. Lett.* **16**, 748 (1966).

[18] G. T. Zatsepin and V. A. Kuzmin, *Sov. Phys. JETP Lett.* **4**, 78 (1966).

[19] J. Elbert and P. Sommers, *Ap. J.* **441**, 151 (1995).

[20] J. A. Simpson, *Ann. Rev. Nucl. Part. Sci.* **33**, 326 (1983).

[21] M. S. Longair, "High Energy Astrophysics", Vol. 2, (Cambridge University Press, 1994).

[22] T. Shibata, *Nucl. Phys. B, Proc. Suppl.* **75A**, 22 (1999).

[23] A. Castellina, *Nucl. Phys. B, Proc. Suppl.* **97**, 35 (2001).

[24] T. Tominaga, *et al.*, *Proc. 23th ICRC*, Calgary, India, **2**, 21 (1995).

[25] A. V. Apanasenko, *et al.*, *Institute of Space and Astronautical Science Report*, **ISAS-37** (1998).

[26] N. L. Grigorov, *et al.*, *Proc. 12th ICRC*, Hobart, Australia, **5**, 1746 (1971).

[27] I. P. Ivanenko, *et al.*, *Proc. 23rd ICRC*, Calgary, India, **2**, 17 (1993).

[28] S. I. Nikolsky, *Nucl. Phys. B, Proc. Suppl.* **39A**, 228 (1995).

[29] A. M. Hillas, *Proc. 16th ICRC*, Kyoto, Japan, **8**, 7 (1979).

[30] P. L. Biermann, *Proc. 23th ICRC*, Calgary, Canada, *Rapporteur*, 45 (1993).

[31] E. S. Seo and V. S. Ptuskin, *Ap. J.* **431**, 705 (1994).

[32] P. L. Biermann, *et al.*, "The Central Parsecs of the Galaxy", *ASP Conf. Series*, **136**, (1999).

[33] R. J. Protheroe and A. P. Szabo, *Phys. Rev. Lett.* **69**, 2885 (1992).

[34] T. Abu-Zayyad, *et al.*, *Phys. Rev. Lett.* **84**, 4276 (2000).

[35] N. Hayashida, *et al.*, *J. Phys. G: Nucl. Part. Phys.* **21**, 1101 (1995).

[36] B. R. Dawson, R. Meyhandan and K. M. Simpson, *Astropart. phys.* **9**, 331 (1998).

[37] TA collaborators, TA proposal (2000).

[38] E. Fermi, *Phys. Rev.* **75**, 1169 (1949).

[39] A. R. Bell, *Mon. Not. R. Astr. Soc.* **182**, 147 (1978).

[40] R. D. Blandford and J. P. Ostriker, *Ap. J.* **221**, L29 (1978).

[41] F. C. Jones, *Proc. Workshop on Observing Giant Cosmic Ray Air Showers from $\geq 10^{20}$ eV Particles from Space*, edited by J. F. Krizmanik, J. F. Ormes and R. E. Steitmatter, *AIP Conference Proc.* **433**, 37 (1997).

[42] C. Cesarsky and V. Ptsukin, *Proc. 23rd ICRC*, Calgary, India, **2**, 341 (1993).

[43] X. Bertou, M. Boratav, A. Letessier-Selvon, *Int. J. Mod. Phys.* **A15**, 2181 (2000).

[44] T. Gaisser, "Cosmic Rays and Particle Physics", (Cambridge University Press, 1990).

[45] K. Koyama, *et al.*, *Nature* **378**, 255 (1995).

[46] J. W. Keohane, *et al.*, *Ap. J.* **454**, 350 (1997).

[47] G. E. Allen, *et al.*, *Ap. J.* **487**, L97 (1997).

[48] C. D. Dermer and M. Humi, *astro-ph/0012272*, submitted to *Ap. J.*.

[49] G. R. Burbidge, F. Hoyle, *Proc. Phys.* **84**, 141 (1964).

[50] pico btG. R. Burbidge, *Phil. Trans. R. Soc. Lond.* **A277**, 481 (1975).

[51] R. D. Blandford and R. L. Znajek, *Mon. Not. R. Astr. Soc.* **179**, 433 (1977).

[52] A. P. Szabo and R. J. Protheroe, *Astropart. Phys.* **2**, 375 (1994).

[53] C. A. Norman, D. B. Melrose and A. Achterberg, *Ap. J.* **454**, 60 (1995).

[54] E. Boldt and P. Ghosh, *astro-ph/9902342*, accepted to *Mod. Not. R. Astr. Soc.*

[55] K. S. Cheng, C. Ho and M. Ruderman, *Ap. J.* **300**, 500 (1986).

[56] A. V. Olinto, *Proc. 26th ICRC*, Salt Lake City, USA, **4**, 361 (1999).

[57] P. Blasi, R. I. Epstein and A. V. Olinto, *Ap. J.* **533**, L123 (2000).

[58] M. Vietri, *Ap. J.* **453**, 883 (1995).

[59] E. Waxman, *Phys. Rev. Lett.* **75**, 386 (1996).

[60] T. Totani, *Astropart. Phys.* **11**, 451 (1999).

[61] E. Waxman, *Phys. Scripta* **T85**, 117 (2000). *astro-ph/9911395.*

[62] F. W. Stecker, *Astropart. Phys.* **14**, 207 (2000).

[63] P. Bhattacharjee, T. W. B Kibble and N. Turok, *Phys. Lett. B* **119**, 95 (1982).

[64] R. Brandenberger, *Nucl. Phys. B* **293**, 812 (1987).

[65] A. J. Gill and T. W. B. Kibble, *Phys. Rev. D* **50**, 3660 (1994).

[66] E. Witten, *Nucl. Phys. B* **249**, 557 (1985).

[67] C. T. Hill, D. N. Schramm and T. P. Walker, *Phys. Rev. D* **36**, 1007 (1987).

[68] C. T. Hill, *Nucl. Phys. B* **224**, 469 (1983).

[69] P. Bhattacharjee and G. Sigl, *Phys. Rev. D* **51**, 4079 (1995).

[70] V. S Berezinsky and A. Vilenkin, *Phys. Rev. Lett.* **79**, 5202 (1997).

[71] P. Bhattacharjee, Q. Shafi and F. W. Stecker, *Phys. Rev. Lett.* **80**, 3698 (1998).

[72] U. F. Wichoski, J. H. MacGibbon and R. H. Brandenberger, *hep-ph/9805419*, submitted to *Phys. Rev. D.*

[73] V. S. Berezinsky, M. Kachelrieβ and A. Vilenkin, *Phys. Rev. Lett.* **79**, 4302 (1997).

[74] V. A. Kuzmin and V. A. Rubakov, *Phys. Atom. Nucl.* **61**, 1028 (1998).

[75] S. L. Dubovsky and P. G. Tinyakov, *JETP Lett.* **68**, 107 (1998).

[76] V. S. Berezinsky, P. Blasi and A. Vilenkin, *Phys. Rev. D* **58**, 103515 (1998).

[77] V. S. Berezinsky and A. Mikhailov, *Phys. Lett. B* **449**, 237 (1999).

[78] G. A. Medina-Tango and A. A. Watson, *Astropart. Phys.* **12**. 25 (1999).

[79] D. Heck, J. Knapp, J. N. Capdevielle, G. Schatz and T. Thouw "CORSIKA : A Monte Carlo Code to Simulate Extensive Air Showers", *Report* **FZKA-6019**, Forschungszentrum Karlsruhe (1998).

[80] Particle Data Group, Review of Particle Physics, *The European Physical Journal* **3**, 76 and 148 (1998).

[81] L. D. Landau and I. J. Pomeranchuk, *Dokl. Akad. Nauk SSSR* **92**, 535 and 735 (1953).

[82] A. B. Migdal, *Phys. Rev.* **103**, 1811 (1956).

[83] P. L. Anthony, *et al.*, *Phys. Rev. D* **56**, 1373 (1997).

[84] M. L. Ter-Mikaelian, "High Energy Electromagnetic Processes in Condensed Media", (Wiley, New York, 1972).

[85] P. L. Anthony, *et al.*, *Phys. Rev. Lett.* **76**, 3550 (1996).

[86] H. Bethe and W. Heitler, *Proc. Roy. Soc.* **A146**, 83 (1934).

[87] J. J. Gaimard, Thèse Université Paris 7 (1990); *Report* **GSI-90-27**, Gesellschaft für Schwerionenforschung, Darmstadt (1990).

[88] X. Campi and J. Hüfner, *Phys. Rev. C* **24**, 2199 (1981).

[89] T. H. Burnett, *et al.*, *Phys. Rev. D* **35**, 824 (1987).

[90] A. S. Goldhaber, *Phys. Lett. B* **53**, 306 (1974).

[91] H. J. Bhabha and W. Heitler, *Proc. Roy. Soc.* **159**, 432 (1937).

[92] J. F. Carlson and J. R. Oppenheimer, *Phys. Rev.* **51**, 220 (1937).

[93] R. Serber, *Phys. Rev.* **54**, 317 (1938).

[94] H. S. Snyder, *Phys. Rev.* **76**, 1563 (1949).

[95] B. Rossi, "High Energy Particles", (Prentice Hall, 1952).

[96] B. Rossi and K. Greisen, *Rev. Mod. Phys.* **13**, 240 (1941).

[97] K. Greisen, *Prog. Cosmic Ray Phys.* **3**, 1 (1956).

[98] T. Gaisser and A. M. Hillas, *Proc. 15th ICRC*, Plovdiv, Bulgaria, **8**, 353 (1977).

[99] E. Longo and I. Sestili, *Nucl. Instru. Meth.* **128**, 283 (1975).

[100] J. N. Capdevielle and J. Gawin, *J. Phys. G: Nucl. Phys.* **8**, 1317 (1982).

[101] A. A. Lagutin *et al.*, *Proc. 16th ICRC*, Kyoto, Japan, **7**, 18 (1979).

[102] K. Kamata and J. Nishimura, *Prog. Theor. Phys. Suppl.* **6**, 93 (1958).

[103] K. Greisen, *Ann. Rev. Nucl. Sci.* **10**, 63 (1960).

[104] A. V. Glushkov, *et al.*, *J. Nucl. Phys.* preprint (1994).

[105] M. Nagano, *et al.*, *J. Phys. G: Nucl. Phys.* **10**, 1295 (1984).

[106] A. M. Hillas, D. J. Marsden, J. D. Hollows and H. W. Hunter, *Proc. 12th ICRC*, Hobart, Australia, **3**, 1001 (1971).

[107] H. Y. Dai, K. Kasahara, Y. Matsubara, M. Nagano and M. Teshima, *J. Phys. G: Nucl. Phys.* **13**, 793 (1988).

[108] A. M. Hillas, *J. Phys. G: Nucl. Phys.* **8**, 1461 (1982).

[109] T. C. Weekes and K. E. Turver, *Proc. 12th ESLAB Symp.*, Frascati, **ESA SP-124**, 279 (1977).

[110] L. G. Poter, *et al.*, *Nucl. Instru. Meth.* **87**, 87 (1970).

[111] A. N. Bunner, "Cosmic Ray Detection by Atmospheric Fluorescence", Ph. D thesis, Cornell University (1967).

[112] E. C. Loh, "Fabrication of HiRes Mirrors", *Proc. Tokyo Workshop on Techniques for Study of Extremly High Energy Cosmic Rays*, Tokyo, Japan, 219 (1993).

[113] B. R. Dawson, "Florescence Detector Techniques", Auger Project Fluorescence Workshop, Salt Lake City, (1996).

[114] J. Smith, "Eletronics for the High Resolution EYE Detector", *Proc. Tokyo Workshop on Techniques for Study of Extremly High Energy Cosmic Rays*, Tokyo, Japan, 250 (1993).

[115] C. R. Wilkinson, "The Application of High Precision Timing in the High Resolution Fly's Eye Cosmic Ray Detector", Ph. D thesis, University of Adelaide, Adelaide (1998).

[116] J. M. Pasachoff, "Astronomy: From the Earth to the Universe", (Saunders College Publishing, 1998).

[117] T. Abu-Zayyad, "The Energy Spectrum of Ultra High Energy Cosmic Rays", Ph. D thesis, University of Utah (2000).

[118] D. J. Bird, *et al.*, "The Calibration of Photomultiplier Tubes in The HiRes Experiment" *Proc. Tokyo Workshop on Techniques for Study of Extremly High Energy Cosmic Rays*, Tokyo, Japan, 269 (1993).

[119] F. X. Kneizys, *et al.*, "The MODTRAN 2/3 Report and LOWTRAN 7 MODEL" *MODTRAN Report* (1996).

[120] NASA (National Aero Space Administration), NOAA (NAtional Oceanic and Atmospheric Administration) and US Air Force, "US standard atmosphere", *NASA technical report* **NASA-TM-X-74335** (1976).

[121] D. R. Longtin, *et al.*, "A Wind Dependent Aerosol Model: Radiative Properties", *AFGL-TR-88-0112*, (1988).

[122] L. R. Wiencke, *et al.*, *Nucl. Instru. Meth. A* **428**, 593 (1999)

[123] T. Abu-Zayyad, *el al.*, "Atmospheric Monitoring at the High Resolution Fle's Eye: Atmospheric Scattering", *Proc. 25th ICRC*, Durban, South Africa, **5**, 345 (1997).

[124] R. W. Clay, *et al.*, *Astro. Soc. Aust.* **15**, 332 (1998).

[125] S. J. Sciutto, "AIRES, a system for air shower simulations. User's manual and reference guide", *Pierre Auger Observatory technical note* **GAP-98-032** (1998).

[126] A. M. Hillas, *Proc. 19th ICRC*, La Jolla, USA, **1**, 155 (1985).

[127] R. S. Fletcher, T. K. Gaisser, P. Lipari and T. Stanev, *Phys. Rev. D* **50**, 5710 (1994).

[128] N. N. Kalmykov, S. S. Ostapchenko and A. I. Pavlov, *Nucl. Phys. B, Proc. Suppl.* **52**, 17 (1997).

[129] IAGA Dividion V, Working Group 8, "International Geomagnetic Field, 1995 Revision", *J. Geomag. Geoelectr.* **47**, 1257 (1995).

[130] A. M. Hillas, *Proc. 17th ICRC*, Paris, France, **8**, 193 (1981).

[131] A. M. Hillas, *Nucl. Phys. B, Proc. Suppl.* **52**, 29 (1997).

[132] A. F. Bielajew, "Photon Monte Carlo simulation", *Report* **PIRS-0393**, National Research Council of Canada (1993).

[133] A. F. Bielajew and D. W. O. Rogers, "Electron Monte Carlo simulation", *Report* **PIRS-0394**, National Research Council of Canada (1993).

[134] H. Fesefeldt, *Report* **PITHA-85/02**, RWTH, Aachen (1985).

[135] R. Brun, *et al.*, *Report* **CERN DD/EE/84-1**, CERN (1987).

[136] J. Ranft, *Phys. Rev. D* **51**, 64 (1995).

[137] K. Werner, *Phys. Rep.* **232**, 87 (1993).

[138] J. N. Capdevielle, *J. Phys. G: Nucl. Part. Phys.* **15**, 909 (1989).

[139] J. Linsley, private communication by M. Hillas (1988).

[140] M. J. Berger and S. M. Seltzer, "Table of Energy Losses and Ranges of Electrons and Positrons" *National Aeronautics and Space Administration Report* **NASA-SP-3012**, Washington DC (1964).

[141] M. J. Berger, "ESTAR : Computer Program for Calculating Stopping Power", *NIST Report* **NISTIR-4999**, Washington DC (1992).

[142] J. Linsley, *Proc. 18th ICRC*, Bangalore, India, **12**, 159 (1983).

[143] R. M. Baltrusaitis *et al.*, *Proc. 19th ICRC*, La Jolla, USA, **7**, 159 (1985).

[144] F. Kakimoto, *et al.*, *Nucl. Inst. Meth. A* **372**, 527 (1996).

[145] C. Song *et al.*, *Astropart. Phys.* **14**, 7 (2000).

[146] T. Abu-Zayyad *el al.*, accepted to *Astropart. Phys.* (2001).

[147] R. M. Baltrusaitis *et al.*, *Phys. Rev. D* **31**, 2192 (1985).

[148] M. J. Kidd, "Properties of Extensive Air Showers Around 10^{17}eV", Ph. D thesis, University of Illinois at Urbana-Champaign (1997).

[149] G. L. Cassiday, *et al.*, *Ap. J.* **356**, 669 (1990).

[150] M. Takeda, *et al*, *Phys. rev. Lett* **81**, 1163 (1998).

[151] see contributions of the AGASA and HiRes group to the International Cosmic Ray Conference 2001 in Hamburg, Germany.

[152] S. Lee, *Phys. Rev. D* **58**, 043004 (1998).

[153] T. A. Clark, L. W. Brown and J. K. Alexander, *Nature* **228**, 847 (1970).

[154] R. J. Protheroe and P. L. Biermann, *Astropart. Phys* **6**, 45 (1996).

[155] P. P. Kronberg, *Rep. Prog. Phys.* **57**, 325 (1994).

[156] G. Sigl, S. Lee, P. Bhattacharjee and S. Yoshida, *Phys. Rev. D* **59**, 043504 (1999).

[157] T. Erber, *Rev. Mod. Phys.* **38**, 4 (1966).

[158] V. H. Bayer, B. M. Katkov and V. S. Fadin, "Radiation of Relativestic Electrons", (Moscow, Atomizdat, 1973).

[159] private communication with N. Inoue (1999).

[160] Z. Cao, private communication with H. P. Vankov (2000).

- *Before 1989, Journal of Physics G: Nuclear and Particle Physics was entitled Nuclear Physics.*
- *Before 1978, Annual Review of Nuclear and Particle Science was entitled Annual Review of Nuclear Science.*
- *ICRC : International Cosmic Ray Conference held biannually.*